

July 2021

## Enhanced Oil Recovery in Tight Rocks Using the “Slot-Drill” Completion

Hassan Amer

*Louisiana State University and Agricultural and Mechanical College*

Follow this and additional works at: [https://digitalcommons.lsu.edu/gradschool\\_theses](https://digitalcommons.lsu.edu/gradschool_theses)



Part of the [Petroleum Engineering Commons](#)

---

### Recommended Citation

Amer, Hassan, "Enhanced Oil Recovery in Tight Rocks Using the “Slot-Drill” Completion" (2021). *LSU Master's Theses*. 5394.

[https://digitalcommons.lsu.edu/gradschool\\_theses/5394](https://digitalcommons.lsu.edu/gradschool_theses/5394)

This Thesis is brought to you for free and open access by the Graduate School at LSU Digital Commons. It has been accepted for inclusion in LSU Master's Theses by an authorized graduate school editor of LSU Digital Commons. For more information, please contact [gradetd@lsu.edu](mailto:gradetd@lsu.edu).

# ENHANCED OIL RECOVERY IN TIGHT ROCKS USING THE “SLOT-DRILL” COMPLETION

A Thesis

Submitted to the Graduate Faculty of the  
Louisiana State University and  
Agricultural and Mechanical College  
in partial fulfillment of the  
requirements for the degree of  
Master of Science in Petroleum Engineering

in

Craft and Hawkins Department of Petroleum Engineering

by  
Hassan Abdelrahman Amer  
B.S., The American University in Cairo, 2019  
August 2021

## Acknowledgments

I would like to thank God Almighty for giving me the strength to conduct this study. It is with genuine pleasure to express my gratitude to my advisor and mentor, Dr. Olufemi Olorode, for inspiring me and financially supporting my MS studies at the Petroleum Engineering Graduate Program at LSU. His inspirations, timely suggestions, and enthusiasm were incredibly beneficial and much appreciated. I am thankful to Dr. Paulo Waltrich, Dr. Jianhua Chen, and Dr. Shengli Chen for serving as committee members. Special thanks to Dr. Bin Wang for his help with my research.

I want to show appreciation to the following people who always motivated me in every possible way and pushed me the extra mile: to my parents, Dr. Abdelrahman Amer and Mahitab Shafik, my sisters Yara, Maha, Nada, and Jana, and my grandmother Afaf (RIP).

I am also thankful for my friends A. Ikbariah, H. Alqrenawi, Y. Elnoamany, M. Ramadan, H. UR Rashid, and O. Hassan for their continuous laughter and support throughout the years.

# Table of Contents

Acknowledgments . . . . .	ii
List of Tables . . . . .	v
List of Figures . . . . .	vii
Nomenclature . . . . .	xiii
Abstract . . . . .	xv
Chapter 1. Introduction . . . . .	1
1.1. Research Objectives . . . . .	2
1.2. Proposed Slot-Drill EOR Technology . . . . .	2
1.3. Thesis Outline . . . . .	6
Chapter 2. Present Status of the Problem . . . . .	8
2.1. Simulation Studies and Field Pilots for Shale EOR methods. . . . .	8
2.2. Governing Equations for Compositional Reservoir Simulation. . . . .	13
2.3. Natural Fracture Modeling in Reservoir Simulation . . . . .	17
2.4. Molecular Diffusion Models. . . . .	19
Chapter 3. Diffusion Models Implementation for Primary Systems. . . . .	24
3.1. Effect of Matrix Permeability . . . . .	25
3.2. Effect of Grid Resolution . . . . .	28
3.3. Effect of Gravity Segregation . . . . .	31
Chapter 4. Natural Fracture Network Connectivity and Uncertainty Analyses. . . . .	32
4.1. Computation of Percolation Threshold for Naturally-Fractured Reservoirs. . . . .	32
4.2. Application of Percolation Theory to Slot-Drilled Shale Reservoirs. . . . .	37
4.3. Natural Fracture Network Conductivity Analyses. . . . .	40
Chapter 5. SDEOR Simulation Results for Fractured Shale Formations. . . . .	46
5.1. Simulation Study of the Long-term Performance of the SDEOR Technology. . . . .	46
5.2. Performance Comparison Between CGEOR and the SDEOR technology. . . . .	51
5.3. Evaluation of the Recovery Mechanisms in SDEOR. . . . .	55
5.4. Simulation Results for the SDEOR Technology Application in Heterogeneous Shale Formations. . . . .	69
5.5. Effect of the SD Fracture Conductivity on the SDEOR Technology Performance. . . . .	72
5.6. Waterflooding Application to Fractured Shale Formations using the SDEOR Technology. . . . .	74
5.7. SDEOR Application to Shale Formations . . . . .	75



Chapter 6. Conclusions and Recommendation for Future Work. . . . .	89
6.1. Summary and Conclusions . . . . .	89
6.2. Recommendations for Future Work . . . . .	91
Appendix A. Fluids Compositional Input Data . . . . .	95
Appendix B. Permissions for Published Work . . . . .	98
References . . . . .	99
Vita . . . . .	106

## List of Tables

2.1	A summary of simulation results for EOR gas injection into different shale oil formations (Du and Nojabaei, 2019).	12
3.1	Reservoir input parameters for diffusion model implementation for primary gas recovery.	25
3.2	Percentage increase of gas production for different values of matrix permeabilities by modeling diffusion in a coarse grid ( $\times 64$ ).	27
3.3	Percentage increase of gas production for different values of matrix permeabilities by modeling diffusion in a coarse grid ( $\times 1024$ ).	27
3.4	Percentage increase of gas production for different grid refinement resolutions by incorporating diffusion modeling.	29
4.1	Reservoir input parameters for the base case simulation.	38
4.2	Different NF network conductivities for $k_m = 1\text{e-}2$ md.	41
5.1	SD-EOR performance summary under different flooding periods in a reservoir with 1024 conductive NFs.	49
5.2	Input parameters for CGEOR in MSHF completion.	52
5.3	Performance comparison between SDEOR and CGEOR after 8 years.	53
5.4	Results summary for the role of $\Delta P_{\text{diff}}$ in oil recovery for SDEOR technology under constant injection rates and a $P_{\text{wf}}$ of 1,000 psia after 30 years.	58
5.5	Results summary for the SDEOR technology application for cases where $P_{\text{wf}}$ is above and below $P_b$ (1,820 psia) with a constant $q_{\text{inj}}$ of 10 Mscf/D after 30 years.	60
5.6	Results summary for role of gravity-drainage in the SDEOR technology performance. In cases of high matrix permeabilities and nearly vertical fractures, gravity contributes more to oil recovery.	64
5.7	$F_{\text{CD}}$ corresponding to different SD fracture conductivities.	73
5.8	Incremental oil recovery in shale formations from our SDEOR technology and CGEOR.	80
5.9	Results of SDEOR with different gas injectants.	85

A.1	Compositional data for Barnett dry gas formation (Xiong et al., 2015). . . . .	95
A.2	Binary Interaction Coefficients for Barnett dry gas formation (Xiong et al., 2015). . . . .	95
A.3	Compositional data for SDEOR synthetic oil fluid. . . . .	96
A.4	Binary Interaction Coefficients for SDEOR synthetic oil fluid. . . . .	96
A.5	Compositional data for Eagle Ford shale formation, culled from (Yu et al., 2019). . . . .	96
A.6	Binary Interaction Coefficients for Eagle Ford shale formation, culled from (Yu et al., 2019). . . . .	96
A.7	Compositional data for Bakken light oil shale formation, culled from (Yu et al., 2015). . . . .	97
A.8	Binary Interaction Coefficients for Bakken light oil shale formation, culled from (Yu et al., 2015). . . . .	97

## List of Figures

1.1	An illustration of how to cut mechanical SD fractures using a tensioned cable connected via two wellbores (modified from (Coleman and Hester, 2010)). . . .	4
1.2	An illustration for a Slot-Drill completion for creating one artificial fracture for a horizontal well (Carter Jr, 2011). . . . .	4
1.3	An illustration for the proposed Slot-Drill EOR technology. . . . .	5
1.4	A schematic diagram showing the reservoir top where the yellow region represents the actual area of SD fracture. Either (1) a rough semicircular or (2) structured rectangular grids can approximate SD fracture area in a reservoir simulator. . .	5
1.5	Different approximations to SD fracture area using structured grids in MRST simulator. . . . .	6
1.6	Simulation results after 30 years comparing different area approximations for SD fracture, as shown in Figure 1.5. . . . .	6
2.1	A comparison between different NF modeling approaches in reservoir simulations (Courtesy for SimTech, LLC). . . . .	10
2.2	Types of NNCs in EDFM (Moinfar et al., 2012). . . . .	18
3.1	A reservoir model for primary gas production under diffusion modeling, where blue and yellow cells distinguish between HF and horizontal well locations, respectively . . . . .	25
3.2	A semi-log plot for different matrix permeability affecting diffusion contribution to primary gas production gain under coarse ( $\times 64$ ) and fine ( $\times 1024$ ) grids. . . .	28
3.3	A Cartesian plot for different grid resolution levels ( $\times 16$ , $\times 32$ , $\times 64$ , $\times 128$ , $\times 256$ , $\times 512$ , and $\times 1024$ ) affecting diffusion contribution to primary gas production gain: green line refers to dispersion flux from Equation (2.25) and red line refers to the dusty-gas diffusion model in Equation (2.37). . . . .	29
3.4	Different levels of grid resolution ( $\times 16$ , $\times 32$ , $\times 64$ , $\times 128$ , $\times 256$ , $\times 512$ and $\times 1024$ ): blue and yellow areas refer to HF cells and horizontal well location, respectively. . . .	30
3.5	$C_1$ gas composition after 15 years in a reservoir with matrix permeability of 1 nD and grid resolution of $\times 128$ : (left) gravity modeled, as in Equation (2.37), and (right) without gravity, as in Equation (2.38). . . . .	31
4.1	The images show fractured reservoirs populated with stochastic fractures ranging	

	from as little as 8 to as many as 1500 natural fractures. Each image corresponds to one realization from a probabilistic distribution of the location, orientation, and size of the individual fractures that make up the fracture network with the specified number of fractures. . . . .	36
4.2	A log-log plot of CI and $eCI_{i,j,k}$ against fracture intensities. Each point in this figure corresponds to the natural fracture networks shown in Figure 4.1. The dashed green lines indicate the fracture intensity range that defines the percolation threshold. . . . .	38
4.3	The oil recovery factor and cumulative oil production plots show increased production when the fracture intensity exceeds the percolation threshold. The dashed green lines indicate the percolation threshold. . . . .	39
4.4	The plots of $eCI_k$ for each matrix cell show the poor and high fracture connectivities at (left) 16 and (right) 512 natural fractures, respectively. . . . .	40
4.5	Images illustrate different realizations of 512 natural fractures, which are used for uncertainty analysis. . . . .	41
4.6	Results indicate a small variation in the oil recovery factor as the number of high-conductivity fractures increases from 8 to 1024. Several realizations are simulated to quantify the uncertainty associated with different realizations of these conductive natural fracture networks. . . . .	43
4.7	A box-plot for quantifying the uncertainty of SD-EOR oil RF associated with different realizations of low-conductive NF networks. . . . .	44
4.8	Results indicate the robustness of our SDEOR technology when applied to a tight rock with 1024 fractures of high-conductivity, low-conductivity, or with mixed conductivity. For this extreme case of 1024 NFs, EOR oil RF only varies from 13.42% to 13.81% after 8 years of simulation. . . . .	45
4.9	Reservoir grid visualizations for $C_1$ gas composition by the end of 8 years SD-EOR simulation for conductive fracture networks: 16 NFs case (top) and 512 NFs case (bottom). . . . .	45
5.1	These performance plots show the long-term effectiveness of the SDEOR technology, regardless of the presence of natural fractures. The results show that the oil production does not decline until after 30 years, and gas does not break through until after 25 years. . . . .	47
5.2	The blue lines show that the EOR recovery factor stays almost constant regardless of the fracture intensity but increases over time as expected. The red triangles on the y-axis indicate the corresponding recovery factor for a case with no	

	fractures (zero fracture intensity). The percolation threshold is shown as the interval between the two green lines. . . . .	48
5.3	These profiles show how the methane gas composition evolves for a base case without natural fractures (left column) and for a case with 1024 conductive fractures (right column). . . . .	50
5.4	Image shows the simulation domain for the CGEOR method. The natural fractures are shown as yellow planes, while the hydraulic fractures are shown as red vertical planes. . . . .	52
5.5	The results show that SDEOR yields three times more oil than CGEOR, and half as much of associated gas production. The primary recovery from the slot-drilled and MSHF wells match because the total fracture area is the same in both cases. . . . .	53
5.6	Left image shows the methane gas profile after 8 years of simulated SDEOR while right image shows the corresponding methane profile from the CGEOR method. . . . .	54
5.7	Left image shows the profile for the methane mole-fraction, with the last 8 cells in the x-direction taken out, while the right image cuts out half of the matrix cells above the middle of the reservoir. It shows that the methane gas saturates the pore volume in the vicinity of the hydraulic fracture clusters, leading to the limited performance of the CGEOR method. . . . .	55
5.8	Performance plots show the role of the pressure difference between the injector and producer in the SDEOR technology. Figure (5.8a) and (5.8b) presents the plots of cumulative oil and gas production. Lower injection pressures corresponds to lower cumulative gas production, but the same cumulative oil produced compared to higher injection pressures. . . . .	57
5.9	Performance plots for different injection rates showing the effect of $\Delta P_{\text{diff}}$ on oil recovery while applying the SDEOR technology after 30 years at a constant $P_{\text{wf}}$ of 1,000 psia. Increasing $q_{\text{inj}}$ increases $\Delta P_{\text{diff}}$ , and hence increases both oil and gas production. In the 1 MMscf/D case, oil production reaches a plateau shortly after 2.5 years as gas fully saturates the region between the top and bottom SD fractures. . . . .	59
5.10	Performance plots for different $P_{\text{wf}}$ (corresponding to cases below and above $P_b$ as denoted by red and blue curves, respectively) with a constant $q_{\text{inj}}$ of 10 Mscf/D for 30 years while implementing the SDEOR technology. . . . .	60
5.11	Images show $C_1$ vapor mole fraction while simulating the SDEOR technology under a constant $q_{\text{inj}}$ of 10 Mscf/D and different $P_{\text{wf}}$ above and below $P_b$ . $\Delta P_{\text{diff}}$ during injection eventually controls how much oil is produced in both cases. . . . .	61

5.12	Performance plots for the cases with and without gravity demonstrates that gravity plays a significant role in the SDEOR technology. Gravity-drainage increases oil production by 20.54% after 30 years. . . . .	63
5.13	Left and Right images show the profile of methane gas mole fraction with and without gravity, respectively. Gravity tends to stabilizes the injected gas front and delays gas breakthrough, compared to the cases without gravity where injected gas coexists with the reservoir fluid without phase segregation and undergoes an early breakthrough. . . . .	65
5.14	Performance plots show the cumulative oil (Left) and gas (Right) production under the effect of molecular diffusion (modeled using Equation (2.37)). Results show that considering the dusty-gas diffusion only increases cumulative production by 3.46% and 3.54% for oil and gas, respectively, after 30 years when applied to the SDEOR technology in shale formations. . . . .	67
5.15	A plot shows the surface oil viscosity after 30 years while applying the SDEOR technology application. As injected gas intermixes with reservoir oil, its viscosity decreases as depicted by the figure. . . . .	68
5.16	Images show in-situ oil phase viscosity at the beginning (left) and after 30 years (right) of simulating our SDEOR technology while constantly injecting at a $q_{inj}$ of 10 Mscf/D and producing at $P_{wf}$ of 1,000 psia. In-situ oil viscosity decreases as injected gas continuously mixes with residual oil in the reservoir. . . . .	68
5.17	An image shows the Gaussian distribution of matrix porosity in a $200 \times 100 \times 80$ m simulation domain. Matrix porosity ranges between 6% and 10%. . . . .	69
5.18	Plots of matrix permeability distributions using (5.18a) Carman-Kozeny relation and (5.18b) using log-normal distribution. Both approaches are used to generate a heterogenous permeability distribution for the grid blocks in the simulation domain. . . . .	70
5.19	Images of matrix permeability distribution in the grid blocks for simulation domain dimensions of $200 \times 100 \times 80$ m using (5.19a) CK relation and (5.19b) log-normal distribution. . . . .	71
5.20	Performance plots show a comparison of the cumulative oil (Left) and gas (Right) production from a homogenous base case, and two heterogenous permeability distribution cases using CK relation and the log-normal distribution. The results show the robustness of our SDEOR technology application in heterogeneous shale formations as cumulative oil production profile is the same for the 3 cases up to 20 years of production. . . . .	72
5.21	Performance plots show a comparison of the cumulative oil (Left) and gas (Right)	

production for different SD conductivity cases. Results show that SDEOR performance is robust as long as SD fractures are infinite-conductive. . . . .	73
5.22 Performance plots show the cumulative oil (Left) and gas (Right) production for waterflooding application using the SD technology. The results only show 4.19% oil recovery increase after 30 years because of the low formation injectivity. . . .	74
5.23 Images of water saturation maps after 30 years. Left image (5.23a) shows the limited penetration capability of water into the matrix and natural fractures. Right image (5.23b) is a zoomed vertical cross-section that shows water only flows a half meter above the SD fracture (located at 70 meters). . . . .	75
5.24 2-phase envelope for Eagle Ford volatile oil shale (generated using CMG-WinProp 2018.1). . . . .	77
5.25 Performance plots show a comparison of the cumulative oil (Left) and gas (Right) production from primary production, CGEOR, and SDEOR from a representative Eagle Ford shale oil well. The results show that SDEOR yields more than 3.8 times more oil than CGEOR. . . . .	78
5.26 An image for 150 NFs having the same dip ( $60^\circ \sim 90^\circ$ ) and dip direction (S40°E to N50°W) ranges as Bakken shale formation (Sturm and Gomez, 2009). . . . .	79
5.27 2-phase envelope for Bakken volatile oil shale (generated using CMG-WinProp 2018.1). . . . .	79
5.28 Performance plots show a comparison of the cumulative oil (Left) and gas (Right) production from primary production, CGEOR, and SDEOR from a representative Bakken shale oil well. The results show that SDEOR yields more than 3.2 times more oil than CGEOR. . . . .	80
5.29 Performance plots after 30 years for SDEOR technology application to fractured Bakken shale. Results indicate the robustness of our proposed technology as it produces at least four times more oil than primary recovery regardless of the number of sealing or conductive fractures in the reservoir. . . . .	82
5.30 C <sub>1</sub> gas composition maps after 30 years when the SDEOR applies to the Bakken shale for (5.30a) a base case without NFs, (5.30b) with 1024 conductive NFs and (5.30c) with 1024 non-conductive NFs. Adding NFs beyond the percolation threshold distorts the developed stable gas front during injection, and slightly reduces the overall injected gas sweeping efficiency. . . . .	83
5.31 Performance plots show that methane gas injection recovers more oil when compared with the injection of the other heavier gases. . . . .	85



5.32	Images show solvent's gas composition distribution in the grid blocks after simulating Bakken shale for 30 years: (5.32a) CH <sub>4</sub> , (5.32b) N <sub>2</sub> , and (5.32c) CO <sub>2</sub> . The lightest solvent injection (CH <sub>4</sub> ) results in the highest oil RF for the SDEOR technology. . . . .	86
5.33	Images show solvent's K-value distribution in the grid blocks after simulating Bakken shale for 30 years: (5.33a) CH <sub>4</sub> , (5.33c) CO <sub>2</sub> , and (5.33b) N <sub>2</sub> gases. High K-values imply immiscible solvent flooding, such as N <sub>2</sub> . Regardless of the solvent miscibility/immiscibility with the reservoir fluid, applying our SDEOR technology for Bakken shale outperforms the CGEOR method and produces at least 3.43 more oil than primary recovery for the least efficient CO <sub>2</sub> case and up to 5.64 for the most efficient CH <sub>4</sub> case. . . . .	88
6.1	Left image shows an SDEOR test cell with a shale core plug placed between top and bottom endcaps. Right image shows an individual endcap with a groove to simulate flow inside the SD fracture. . . . .	92
6.2	An image of the NER AutoLab 1500 testing equipment. . . . .	92
6.3	A 2D reservoir model after the 3D-pEDFM/EDFM processing. Horizontal arrows indicate standard connection between matrix-matrix and fracture-fracture cells, while the curved purple arrow indicates matrix-fracture non-neighbor connection. . . . .	93
B.1	A permission evidence from SimTech, LLC to use the image in Figure 2.1. . . . .	98

## Nomenclature

$A_{if\perp x} =$  area of fracture projections along each dimension,  $L^2, m^2$

$A_{ij}^p =$  projection area,  $L^2, m^2$

$A^{nnc} =$  area of a non-neighboring connection,  $L^2, m^2$

$d^{nnc} =$  non-neighboring connection distance,  $L, m$

$k_f =$  fracture permeability,  $L^2, m^2$

$k_m =$  matrix permeability,  $L^2, m^2$

$k^{nnc} =$  permeability of a non-neighboring connection,  $L^2, m^2$

$K_i =$  vapor-liquid equilibrium constant for component  $i$

$R =$  residual,  $M^{-1}L^{-3}, kg^{-1}m^{-3}$

$S^\alpha =$  saturation of phase,  $\alpha$

$T_i =$  half transmissibility,  $L^3, m^3$

$T^{nnc} =$  transmissibility factor for a NNC,  $L^3, m^3$

$\vec{x}_e =$  The grid block sizes in the X, Y, and Z directions,  $L, m$

$\vec{x} =$  X, Y, and Z coordinates,  $L, m$

$x_i =$  mole-fraction of component,  $i$  in the liquid phase

$X_i^\alpha =$  mass-fraction of component  $i$  in phase,  $\alpha$

$Y_i =$  mass-fraction of component,  $i$  in the gas phase

$y_i =$  mole-fraction of component,  $i$  in the gas phase

$Z_i =$  overall mass-fraction of component,  $i$

$\phi =$  porosity

$\rho =$  density,  $M/L^3, kg/m^3$

$t =$  time,  $T, s$

## Subscripts

f = fracture

m = matrix

M-M = interaction between two different host matrix cells

pM-F = interaction a projection matrix and a fracture cell

i,j = Cell indices

if = interaction between matrix cell,  $i$  and fracture cell,  $f$

$\alpha$  = fluid phase

## Superscripts

k+1 = current time step

nnc = Non neighbouring connections

## Abstract

Enhanced oil recovery (EOR) is essential in shale/tight formations because primary recovery typically produces less than 10% of the original hydrocarbon in-place (OHIP). This work presents a novel "slot-drill" EOR technology, which involves injecting gas through a horizontal fracture that is cut into the formation near the top of the reservoir (using a tensioned abrasive cutting cable mounted to the drillstring) and producing oil from a second slot-drilled horizontal fracture near the bottom of the reservoir.

The dusty-gas diffusion model was implemented in a compositional simulator to account for the diffusion mechanism expected during the injection of gases in this EOR process. The simulation results indicate that the simulated contribution of molecular diffusion to production increases as the mesh gets finer and matrix permeability decreases. Additionally, a robust 3D projection-based embedded discrete fracture model is used to model the natural fractures in these slot-drilled unconventional oil reservoirs accurately and efficiently. Connectivity and uncertainty analyses are performed to determine the percolation threshold, where natural fractures influence hydrocarbon production appreciably. The results of this work indicate that the proposed technology can yield over a three-fold increase in oil recovery relative to the cyclic gas EOR (CGEOR) method. This simulated recovery is high regardless of the presence of natural fractures or the type of gas/solvent injected (such as  $\text{CH}_4$ ,  $\text{N}_2$ ,  $\text{CO}_2$ , and flue gas). The simulation results also indicate that the continuous gas injection, higher relative oil permeability, and the role of gravity-drainage are the main reasons why the oil recovery from the SDEOR is three times that from the CGEOR method.

In conclusion, this thesis is the first to introduce the SDEOR technology and

demonstrate its potential to improve recovery from challenging unconventional reservoirs (such as the Bakken shale), which has not been successfully enhanced using the conventional cyclic gas EOR. The three-fold to nine-fold improved recovery from the SDEOR, coupled with its applicability regardless of the stress state or rock brittleness, could change how unconventional reservoirs are completed and produced in the future.

## Chapter 1. Introduction

This thesis focuses on the presentation and numerical evaluation of a novel technology of EOR in unconventional reservoirs. The proposed technology utilizes the "Slot-Drill" (SD) completion technique to artificially create fractures in subsurface rocks, regardless of their mechanical properties. This precise determination of fracture placement allows for easier modeling and simulation of the technology, as I explain in detail in the following subsection. The primary value of this work is to present a novel EOR technology that is advantageous to the existing cyclic gas EOR (CGEOR) method used in shale formations. The SDEOR is a groundbreaking technology, and it outperforms CGEOR methods by producing at least three times more oil when applied to Bakken and Eagle Ford shale formations. In this thesis, several simulation studies are presented to assess the performance of the SDEOR technology in fractured formations by quantifying the role of natural fracture conductivity and uncertainty on the short and long-term performance of the SDEOR. Also, the involved recovery mechanisms are evaluated for a better understanding of how SDEOR best works to recover hydrocarbon from tight formations. The tools used in this work include (1) ADFNE (Alghalandis Discrete Fracture Network Engineering), which is an open-source code Alghalandis (2017) to generate stochastic NF networks with arbitrary orientation, length, conductivity, and aperture, (2) in-house 3D projection-based embedded discrete fracture model (3D-pEDFM) algorithm to model both high and low conductive NF networks (Olorode et al., 2020), and (3) the MATLAB Reservoir Simulation Toolkit (MRST) (Krogstad et al., 2015) for compositional simulation runs. The following subsections explain the research objectives and explain the SDEOR technology and how it is numerically modeled using modern reservoir simulators.

## 1.1. Research Objectives

The overall objectives of this work are as follows:

1. To simulate and study the proposed SDEOR method as a novel technology to increase hydrocarbon recovery from shale-oil formations.
2. To evaluate the performance of the SDEOR technology in naturally fractured unconventional reservoirs. We model natural fractures using 3D-pEDFM and perform connectivity and uncertainty analyses to understand natural fracture networks' effect on SDEOR performance.
3. To evaluate the underlying recovery mechanisms for the SDEOR technology (e.g., gravity-drainage, oil viscosity reduction, molecular diffusion, and the pressure differential between the injector and producer wells).
4. To compare and benchmark the performance of the SDEOR technology versus the current CGEOR methods when applied to shale-oil formations (such as Bakken and Eagle Ford).
5. To study the effects of the reservoir heterogeneity, SD fracture conductivity, and the applicability of waterflooding for the SDEOR technology.

## 1.2. Proposed Slot-Drill EOR Technology

The slot-drill (SD) technology is based on ideas involving using a chain cutter that is pulled through massive rock outcrops, as in (Hurd, 1980; Farrar et al., 1991). The proposed application of this concept to cut fractures in the subsurface involves using one or more wells as Coleman and Hester (2010) proposed drilling two wellbores either from two different wellheads or side-tracked from one well. These wellbores are connected at the toe (or end) using a hook and ring-like steel tools. Next, a flexible and tensioned cutting cable ("wire saw") is passed through one of the wellbores's ring-like structures and fished out from the other wellbore with the steel hook. The cable is then pulled back and forth from the wellhead to cut a slot-drilled fracture of the rock mass between the two wellbores, as shown in Figure 1.1.

SDEOR is a novel technique where gas is injected into horizontal fractures created close to the top of the reservoir, while oil is produced from parallel horizontal fractures created close to the bottom of the reservoir. To artificially create these horizontal fractures regardless of the prevailing stress states in the reservoir, this work suggests the use of the SD completion technique (Carter Jr, 2011), where subsurface rock medium can be cut using tensioned abrasive cables mounted to the drillstring post-drilling the wellbore and before the installation of production tubular, as shown in Figure 1.2. Odunowo et al. (2014) simulated primary recovery from SD and multistage hydraulic fractures (MSHF) completions where he concluded that the latter outperformed the SD completion because of the larger fracture areas open to flow. Although two wells are required to create an SD completion (as shown in Figure 1.2), only one of them is needed for primary production. Here, we propose the use of two wells to create two parallel horizontal fractures, as illustrated in Figure 1.3. After the two fractures are created, one of the wells gets plugged at the bottom and is only allowed to inject fluids at the top, while the other is open to flow from the bottom fracture. Furthermore, our proposed completion design is versatile and allows for other injection schemes, in addition to gas injection into the top fracture. Such schemes include water injection into the bottom SD fracture while producing oil from the top one. Unlike MSHF, which orientation is affected by the stress regime and stress-shadowing effects Yew and Weng (2014), SD completion overcomes this dilemma through its wide range of applicability in different rock mediums (e.g. brittle or ductile) regardless of their frackability.

Figure 1.4 is a top view for a reservoir modeled using structured grids where the yellow region represents the actual SD fracture. Due to the limited capabilities of struc-



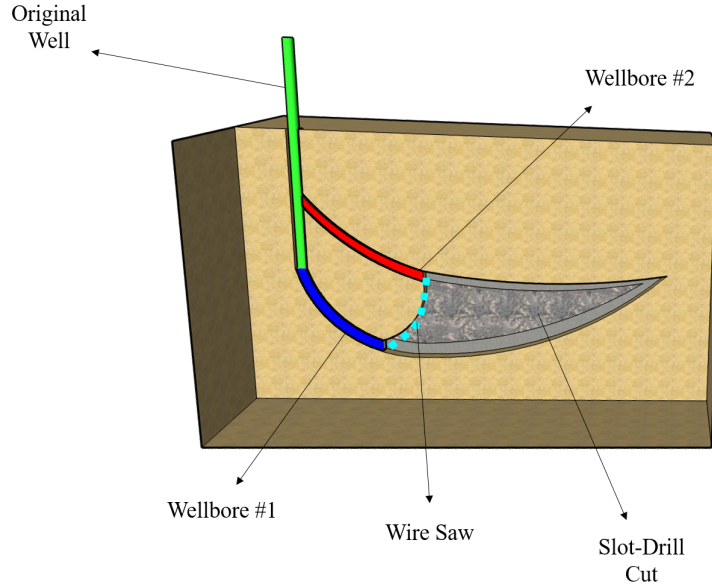


Figure 1.1. An illustration of how to cut mechanical SD fractures using a tensioned cable connected via two wellbores (modified from (Coleman and Hester, 2010)).

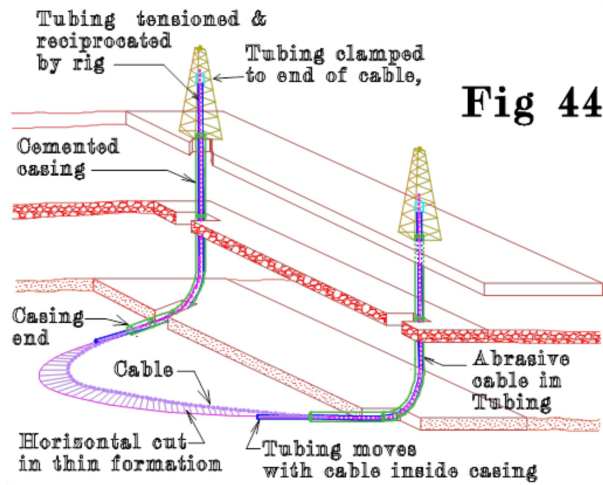


Figure 1.2. An illustration for a Slot-Drill completion for creating one artificial fracture for a horizontal well (Carter Jr, 2011).

tured grids to model smooth edges, we approximate SD fracture area by either a rectangle or a semicircle with rough square edges as Figure 1.5 illustrates. Figure 1.5a is generated by selecting fracture cells in the XY plane satisfying the semicircle equation constraint. We then evaluate how the two different area approximations affect the simulation results by simulating our SDEOR technology for 30 years using a synthetic oil fluid. Figure 1.6

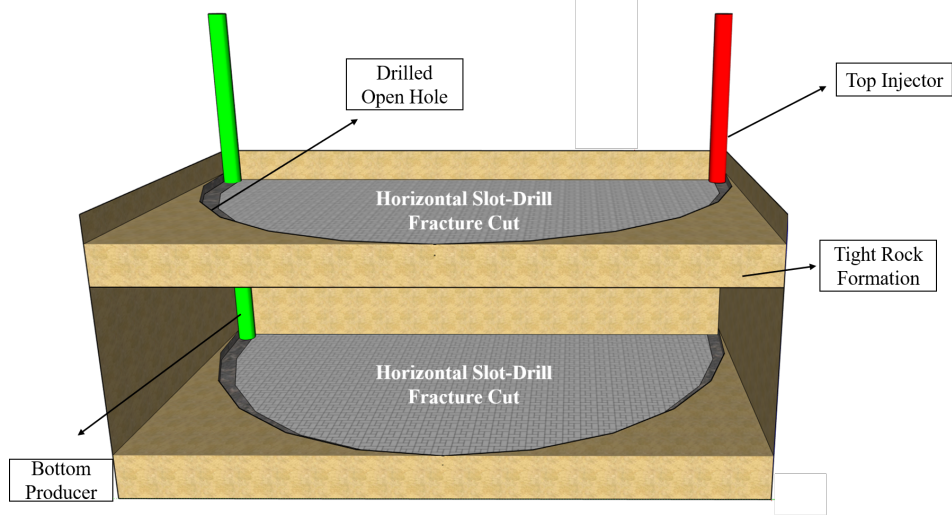


Figure 1.3. An illustration for the proposed Slot-Drill EOR technology.

shows cumulative oil production after 30 years while using rectangular and semicircular area approximations. Results suggest that both area approximations give the same simulation results. We use the semicircular area approximation in this work within the simulation runs.

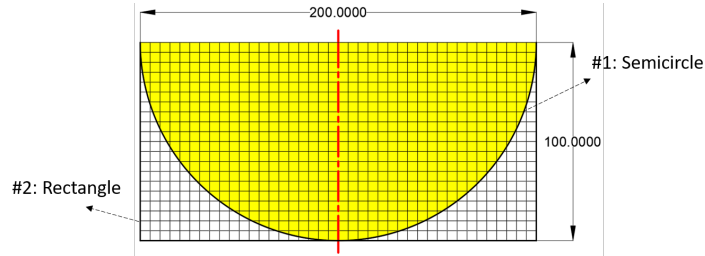
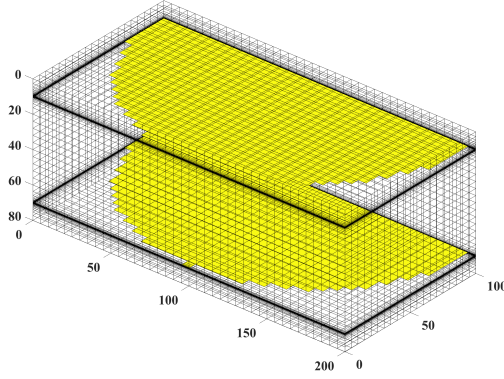
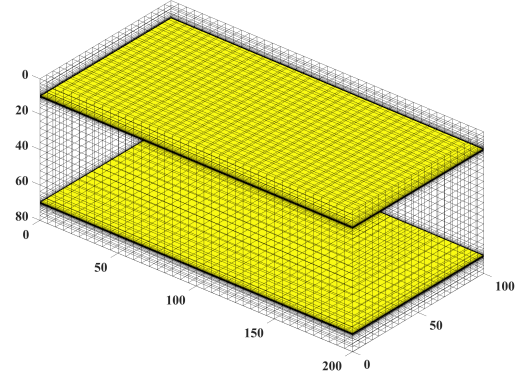


Figure 1.4. A schematic diagram showing the reservoir top where the yellow region represents the actual area of SD fracture. Either (1) a rough semicircular or (2) structured rectangular grids can approximate SD fracture area in a reservoir simulator.



(a) Semicircle



(b) Rectangle

Figure 1.5. Different approximations to SD fracture area using structured grids in MRST simulator.

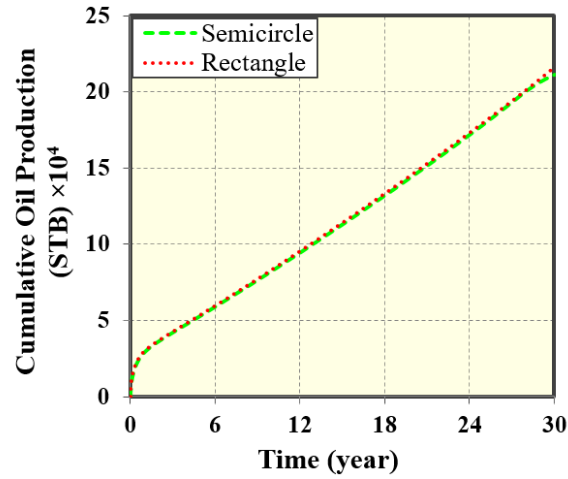


Figure 1.6. Simulation results after 30 years comparing different area approximations for SD fracture, as shown in Figure 1.5.

### 1.3. Thesis Outline

This thesis consists of six chapters and two appendices. Chapter 1 provides background about EOR in tight rocks, research objectives, and an explanation for the proposed SDEOR technology. Chapter 2 discusses the present status of the problem related to simulation studies and field pilots for shale EOR methods, governing equations for compositional reservoir simulation, natural fracture modeling in reservoir simulation, and different molecular diffusion models. Chapter 3 discusses the implementation of diffusion

models for a primary gas production system and studies the effects of matrix permeability, mesh resolution, and gravity on the molecular diffusion contribution to production. Chapter 4 provides an algorithm to compute the percolation threshold for a fractured reservoir system, conductivity, and uncertainty analyses for natural fracture networks and their effects on the SDEOR performance. Chapter 5 presents the results and discussion for different simulation studies related to the SDEOR technology application in shale formations. Chapter 6 provides conclusions and recommendations for future work. Appendix A shows the fluids' compositional input data for the reservoir simulator. Appendix B displays permissions for published work.

## Chapter 2. Present Status of the Problem

This chapter discusses the present status of improving oil recovery in unconventional oil reservoirs using cyclic gas injection. We then present the governing equations that will be used for the compositional simulation of cyclic gas injection and the slot-drill EOR method that will be evaluated in this work. Finally, to ensure that the results of this numerical study apply to actual shale plays, we will account for molecular diffusion in these ultra-low matrix permeability reservoirs and the presence of natural fractures with various orientations and conductivities.

### 2.1. Simulation Studies and Field Pilots for Shale EOR methods.

This section starts by summarizing results from simulation studies and field pilots regarding EOR methods in shale reservoirs. Currently, a combination of horizontal drilling and multistage hydraulic fracturing (MSHF) has resulted in the commercial development of shale or low-matrix permeability resources. The technological advancements over the last couple of years in drilling and completion technologies have enabled operators to drill wells with longer horizontal lateral lengths and to create several fracture clusters with several stages in the wellbore. Nonetheless, the primary recovery in these low-matrix permeability formations is still typically less than 10% of the hydrocarbon initially in-place (Zuloaga-Molero et al., 2016; Alfarge et al., 2017a). More attention is therefore paid to the study of enhanced oil recovery (EOR) in tight rocks, and resulted in several related publications over the last decade that manipulated the use of commercial reservoir simulators to assess the performance of EOR methods in unconventional formations (Yu et al., 2014a,b; Sun et al., 2016; Zhu et al., 2017). The main technique in all of these

previous shale EOR studies is to inject fluids (mostly CO<sub>2</sub> or hydrocarbon gas) through MSHF completion. The injection scheme is altered between continuous flooding (through an injection well) or cyclic (in huff-n-puff mode) as in conventional EOR, where the same wellbore is used for both injection and production following an operational scheme. Considering the two injection schemes, the cyclic gas injection EOR (CGEOR) has proven to be the most successful, based on field and pilot studies in the Eagle Ford shale play (Grinestaff et al., 2020). Moridis et al. (2020) summarized why CGEOR is more successful than the continuous injection, or gas flooding, due to the following reasons. First, the latter injection scheme requires drilling an additional injection well, and due to low-matrix permeability, injection gas will not be able to flow to the production well or preferentially pressurize high-conductive fracture planes surrounding the injection well. Second, CGEOR includes a soaking period that allows the intermixing between the light solvent and in-situ hydrocarbon and hence increases its mobility when it flows back.

The rise of reservoir simulation in the oil and gas industry to simulate EOR processes is due to (1) the significant costs of injecting fluids into shale-oil reservoirs, (2) identification of the optimum EOR mechanism, (3) injection scheme, and (4) optimization of the operational constraints for the injection and production wells. On the other hand, the degree of complexity of these numerical simulations increases due to the existence of NFs in unconventional oil and gas reservoirs. The role of NFs has been reported to have mixed results on the simulation studies. As summarized on page three of Apiwathanasorn et al. (2012), different authors have conflicting views on the significance of the contribution of NFs in unconventional oil and gas reservoirs. The authors performed coupled reservoir simulations to account for NF modeling existing in unconventional reservoirs to resolve

this conflict. The complexity of the reservoir simulation for shale EOR is dependent on the NF model used in the study. Effective continuum matrix/fracture models (such as dual-porosity, dual-permeability, and continuum models, as in Warren and Root (1963); Pruess and Narasimhan (1982)) are most used to model NFs in shale EOR using commercial simulators. Other authors base their models by neglecting the presence of NFs. In contrast with the effective medium models, discrete models (such as discrete fracture models (Kim and Deo, 2000; Karimi-Fard and Firoozabadi, 2001), embedded discrete fracture model (EDFM) (Li and Lee, 2008), projection-based embedded discrete fracture model (pEDFM) (Tene et al., 2017), etc.) are able to account for each individual fracture plane in a naturally-fractured reservoir. Figure 2.1 summarizes the main differences between common NF modeling methods in reservoir simulators; discrete fracture models are advantageous to continuum models when the NF network is unconnected and heterogeneous. This thesis uses the 3D-pEDFM approach to model any stochastic NF network existing in the reservoir, regardless of the aperture, conductivity, and orientation.

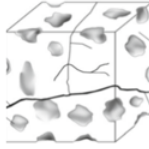
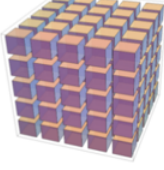
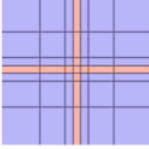
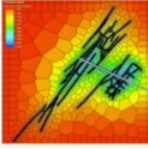
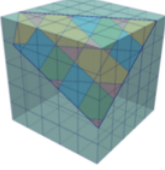
	Complex fracture	Dual-continuum model	Local grid refinement	Unstructured grids	Embedded discrete fracture model
					
			<i>Cipolla et al. (2011)</i>		
<b>Accuracy</b>		✗	✓	✓	✓
<b>Flexibility</b>		✗	✗	✓	✓
<b>Gridding</b>		✓	✓	✗	✓
<b>Computational efficiency</b>		✓	✗	✗	✓

Figure 2.1. A comparison between different NF modeling approaches in reservoir simulations (Courtesy for SimTech, LLC).

Regardless of the fracture model employed, simulation results (as shown in later sections) for our proposed SDEOR technology suggest more recovery than the conventional CGEOR method. For instance, Moridis et al. (2020) employed a single-porosity effective matrix/fracture model for continuous gas injection and showed that the injection of methane gas using the conventional shale EOR method (i.e., using the MSHF completion) did not result in any appreciable increase in oil recovery (relative to primary production) after five years. Other authors (Dahaghi et al., 2010; Eshkalak et al., 2014; Kim et al., 2015; Yu et al., 2014a) have also used the dual continuum models to evaluate CO<sub>2</sub> continuous and cyclic injection in shale-oil reservoirs. Although these methods are computationally faster, they cannot account for the less connectivity or the heterogeneity in the individual fracture sizes, orientation, distribution, and permeability. We focus on presenting the numerical simulation results of the conventional shale EOR methods using EDFM, a discrete NF model. Table 2.1 (modified from Du and Nojabaei (2019)) summarizes some of these EDFM simulation results in formations with low-matrix permeabilities, and provides the corresponding references. These tabulated results, as well as the other numerical and experimental studies summarized in Tables 1 and 2 of Du and Nojabaei (2019), indicate a wide range in the increased oil recovery factor reported by various authors. Since EDFM is unable to account for low-conductive NFs accurately (Tene et al., 2017), the EDFM results in Table 2.1 implicitly assume that all the NFs are conductive, which is very unlikely in reality as NFs can arbitrarily exist at any conductivity. The reason is that the orientation of each NF depends on the prevailing stress regimes when it was created (Shafiei et al., 2018), after which fine-grained/cementing materials could accumulate in these fractures and make them sealing, or have low conductivity, in the prevailing stress



state today. In this thesis, we use the 3D-pEDFM to assess the performance of our proposed SDEOR technology in naturally fractured reservoirs with any arbitrary fracture conductivity.

Table 2.1. A summary of simulation results for EOR gas injection into different shale oil formations (Du and Nojabaei, 2019).

Formation	$k_m$ ( $\mu$ D)	Injected Gas	Injection Mode	Production Period (yrs)	Increased Oil RF (%)	Reference
Middle Bakken	1	CO <sub>2</sub>	Huff-n-Puff	18	+2.56	Zuloaga et al. (2017)
Middle Bakken	1	CO <sub>2</sub>	Continuous Flooding	18	-1.79	Zuloaga et al. (2017)
Middle Bakken	20	CO <sub>2</sub>	Huff-n-Puff	20	+5.9 (3 cycles)	Sun et al. (2019)
Eagle Ford	0.9	CO <sub>2</sub>	Huff-n-Puff	20	+8 (Dco <sub>2</sub> = 0.01 cm <sup>2</sup> /s)	Yu et al. (2019)
Eagle Ford	0.334	Field Gas	Huff-n-Puff	5	+8.75 (single well and 10 cycles)	Ganjdanesh et al. (2019)

Improved oil recovery (IOR) ratio is a standard metric used to assess the performance of EOR methods, and it is defined as the ratio between EOR estimated ultimate recovery (EUR) to the primary EUR. The application of CGEOR in field and pilot studies have yielded mixed results. Several researchers agree that CGEOR has been successful in the Eagle Ford shale formation, with IOR ratios ranging from 1.3 to 1.7 (Grinestaff et al., 2020; Hoffman, 2018). Several authors also agree (Hoffman et al., 2016) that the application of CGEOR has been unsuccessful in the Bakken shale formation. Although Rassenfoss et al. (2017) attributed the lack of incremental oil recovery to the lower matrix permeability of the Bakken, and hence low injectivity, Hoffman et al. (2016) concluded (from his analysis of several EOR field/pilot tests) that early gas breakthrough (or connectivity of the fracture networks with main producer wellbore) rather than poor formation injectivity was the cause of this negligible increment in oil recovery. Although field and pilot studies of the CGEOR in the Eagle Ford formation indicate an IOR ratio of up to 1.7 if hydrocarbon gases are injected at high rates, Jacobs et al. (2019) pointed out that the success of CGEOR in a shale formation depends on its fluid and fracture network properties. The SDEOR technology proposed in this work is able to give IOR ratios of up to 4.17 within

eight years of production, even with fluid, matrix, and fracture properties that are representative of the middle Bakken formation.

## 2.2. Governing Equations for Compositional Reservoir Simulation.

In this section, we summarize the governing equations in compositional simulations that use the natural variables approach, and how MRST simulator discretization schemes work. Without accounting for the presence of natural fractures, the governing equations for the mass conservation of each hydrocarbon component,  $i$ , in the liquid (l) and vapor (v) phases is given as:

$$\frac{\partial}{\partial t} (\phi[\rho^l S^l X_i^l + \rho^v S^v X_i^g]) + \nabla \cdot (\rho^l X_i^l \vec{v}^l + \rho^v X_i^g \vec{v}^v) - (\rho^l X_i^l q^l + \rho^v X_i^g q^v)/V = 0. \quad (2.1)$$

Similarly, the mass conservation equation for water (w) in the aqueous phase is given as:

$$\frac{\partial}{\partial t} (\phi \rho^w S^w) + \nabla \cdot (\rho^w \vec{v}^w) - \rho^w q^w/V = 0, \quad (2.2)$$

where  $\phi$ ,  $\rho^\alpha$ ,  $S^\alpha$ , and  $q^\alpha$  represent the matrix porosity, mass density, saturation, and volumetric withdrawal/injection rate of phase  $\alpha$ , respectively. The symbols  $X_i^l$  and  $X_i^g$  represent the mass fractions of component  $i$  in the liquid and vapor phases, while  $\vec{v}_l$  and  $\vec{v}_v$  are the Darcy velocities for the liquid and vapor hydrocarbon phases, respectively. Note that the division of the source/sink term in Equations (2.1) and (2.2) by bulk volume,  $V$  is needed for dimensional consistency.

We obtain the phase velocities in Equations (2.1) and (2.2) from Darcy's equation as follows:

$$\vec{v}^\alpha = -\mathbf{K} \frac{k^\alpha(S)}{\mu^\alpha} (\nabla p^\alpha - \rho^\alpha g \nabla z), \quad (2.3)$$

where  $\mu^\alpha$  and  $\mathbf{K}$  represent the phase viscosity and absolute matrix permeability, respectively. In the natural variables composition approach (Coats, 1979), which is used in this

work, the primary variables are pressure, vapor and liquid composition of all but the last component, and water saturation ( $p, x_1^l, x_1^g, \dots, x_{n-1}^l, x_{n-1}^g$ , and  $S_w$ ), respectively. The auxiliary thermodynamic equations and constraints needed for compositional simulation are summarized as follows:

$$f_i^g(p, T, y_1, \dots, y_n) - f_i^l(p, T, x_1, \dots, x_n) = 0, \quad \text{for } i \in 1, \dots, n_c, \quad (2.4)$$

$$z_i - Lx_i - (1 - L)y_i = 0, \quad \text{for } i \in 1, \dots, n_c, \quad (2.5)$$

$$\sum_{i=1}^{n_c} x_i = 1, \quad \text{for } i \in 1, \dots, n_c, \quad (2.6)$$

$$\sum_{i=1}^{n_c} y_i = 1, \quad \text{for } i \in 1, \dots, n_c, \quad (2.7)$$

$$S^w + S^l + S^v = 1.0. \quad (2.8)$$

In these equations,  $f_i^g$  and  $f_i^l$  are the fugacities of each component in the gas and liquid phases, respectively. Equation (2.4) ensures that the fugacity of each component in the vapor phase is equal to that of the same component in the liquid phase (which is required at chemical equilibrium), Equation (2.5) ensures that the sum of the number of moles of each component in the liquid and gas phases is equal to its corresponding overall composition, while Equations (2.6), (2.7), and (2.8) ensure that all mole fractions and saturations sum up to one.

We use the Peng-Robinson equation of state (Peng and Robinson, 1976) to compute the fugacities and phase compressibility factors ( $Z^g$  and  $Z^l$ ). Firoozabadi (2015) provides more details on the equation of state, flash procedure, and the equations to compute the fugacities and compressibility factors. To solve the continuous equations in (2.1) and (2.2) numerically, we first perform a temporal discretization using the backward Euler

scheme as follows:

$$\begin{aligned} \frac{1}{\Delta t} \left[ (\phi \rho^l S^l X_i^l + \phi \rho^v S^v X_i^g)^{n+1} - (\phi \rho^l S^l X_i^l + \phi \rho^v S^v X_i^g)^n \right] + \\ \nabla \cdot (\rho^l X_i^l \vec{v}^l + \rho^v X_i^g \vec{v}^v) - (\rho^l X_i^l q^l + \rho^v X_i^g q^v)/V = R_i, \end{aligned} \quad (2.9)$$

$$\frac{1}{\Delta t} \left[ (\phi \rho^w S^w)^{n+1} - (\phi \rho^w S^w)^n \right] + \nabla \cdot (\rho^w \vec{v}^w) - \rho^w q^w/V = R^w. \quad (2.10)$$

In the above equations,  $n + 1$  represents the current time step, while  $n$  represents the previous time step. Note that all other terms without these superscripts are evaluated at the current time step. We then proceed to discretize the flux terms in space using the Finite Volume Method (FVM) with two-point flux approximation (TPFA). The TPFA method involves integrating Equations (2.9) and (2.10) over a control volume, after which the divergence theorem is applied. In this work, we use the discrete divergence (*div*) and gradient (*grad*) operators, which are discussed in the MATLAB reservoir simulation book (Lie, 2019) and implemented as functions in the MATLAB reservoir simulation toolbox (MRST). The resulting discretized form of Equations (2.9) and (2.10) can be written as:

$$\begin{aligned} \frac{V}{\Delta t} \left[ (\phi \rho^l S^l X_i^l + \phi \rho^v S^v X_i^g)^{n+1} - (\phi \rho^l S^l X_i^l + \phi \rho^v S^v X_i^g)^n \right] + \\ \text{div}(\rho^l X_i^l \vec{v}^l + \rho^v X_i^g \vec{v}^v)^{n+1} - (\rho^l X_i^l q^l + \rho^v X_i^g q^v)^{n+1} = R_i^{n+1}, \end{aligned} \quad (2.11)$$

and

$$\frac{V}{\Delta t} \left[ (\phi \rho^w S^w)^{n+1} - (\phi \rho^w S^w)^n \right] + \text{div}(\rho^w \vec{v}^w)^{n+1} - (\rho^w q^w)^{n+1} = R_w^{n+1}, \quad (2.12)$$

where

$$\vec{v}^\alpha = -T_{ik} \lambda_\alpha^{n+1} [\text{grad}(p_\alpha^{n+1}) - \rho_\alpha^{n+1} g \text{grad}(z)], \quad (2.13)$$

$$T_{ik} = [T_{i,k}^{-1} + T_{k,i}^{-1}]^{-1}, \quad (2.14)$$

and

$$T_{i,k} = A_{i,k} \mathbf{K}_i \frac{\vec{c}_{i,k} \cdot \vec{n}_{i,k}}{|\vec{c}_{i,k}|^2}. \quad (2.15)$$

Here,  $V$  and  $A_{i,k}$  refer to the cell volumes and face areas, respectively. The symbol,  $\vec{n}_{i,k}$  is the unit normal in the direction from the centroid of the cell,  $i$  towards the face between cells  $i$  and  $k$ , while  $\vec{c}_{i,k}$  is the vector from the cell centroid to the face centroid. Additionally,  $T_{ik}$  is face transmissibility, while  $T_{i,k}$  is the contribution of a cell to the face transmissibility. This transmissibility ( $T_{i,k}$ ) is referred to as a half-transmissibility because a pair of cells contributes to the transmissibility of each face in the TPFA formulation. Note that the temporal and spatial discretizations of the continuous partial differential equations lead to a mass imbalance, which is represented by the residual ( $R$ ) in Equations eq:speciesBalanceTemp through (2.12). The Newton-Raphson method involves applying the Taylor expansion to the residual at the current time step and current Newtonian iteration to obtain:

$$\frac{\partial R^{k+1}}{\partial X} \Delta X = -R^{k+1}(X), \quad (2.16)$$

where  $X$  denotes the primary variables. The matrix that contains the partial derivatives of the residuals with respect to each of these primary variables ( $\frac{\partial R^{k+1}}{\partial X}$ ) is referred to as the Jacobian matrix. The setup of this matrix is facilitated using automatic differentiation in MRST, and more details on the solution of the system of equations for compositional flow are provided in Møyner et al. (2017). Considering that most shale/tight oil reservoirs are naturally fractured to some extent, this work will involve simulating our proposed SDEOR method in such reservoirs with or without natural fractures. The next section explains how the discretized governing equations are modified to model natural fractures accurately and efficiently.

### 2.3. Natural Fracture Modeling in Reservoir Simulation

There is currently no technology available to accurately determine the location and orientation of natural fractures in the subsurface or quantify their degree of heterogeneity. To account for this uncertainty in determining fracture properties, this work involves the generation of several statistical realizations of the fracture network. This allows us to evaluate the effectiveness of our proposed SDEOR method under different plausible stochastic fracture realizations. Although several models have been proposed to model fluid flow in naturally-fractured reservoirs, we focus on embedded discrete fracture models (EDFM) because they can account for the properties and orientation of each fracture in a reservoir. This section starts with an introduction of EDFM and ends with a discussion of its extension to a projection-based EDFM, which, unlike EDFM, can accurately model low-conductivity fractures.

EDFM uses the concept of non-neighboring connections (NNCs) to couple the flow of fluids in a fracture cell to that of its host (or embedding) matrix cell. The coupling occurs by adding a  $q_i^{nnc}$  term to the semi-discrete form of the governing equation (2.11) as follows:

$$\begin{aligned} & \frac{V}{\Delta t} \left[ (\phi \rho^l S^l X_i^l + \phi \rho^v S^v X_i^g)^{n+1} - (\phi \rho^l S^l X_i^l + \phi \rho^v S^v X_i^g)^n \right] + \\ & \text{div}(\rho^l X_i^l \vec{v}_l + \rho^v X_i^g \vec{v}^v)^{n+1} - (\rho^l X_i^l q^l + \rho^v X_i^g q^v)^{n+1} + q_i^{nnc} = R_i^{n+1}, \end{aligned} \quad (2.17)$$

where  $q_i^{nnc}$  is the mass rate of component  $i$  that is exchanged through the NNC (in units of mass per time). It is given as:

$$q_i^{nnc} = \sum_{m=1}^{N_{nnc}} A_m^{nnc} \sum_{\alpha=1}^{n_p} \frac{k_m^{nnc} k_{r\alpha}}{\mu^\alpha} \rho^\alpha X_i^\alpha \left[ \frac{(p^\alpha - \rho^\alpha g z) - (p_\alpha - \rho_\alpha g z)_m^{nnc}}{d_m^{nnc}} \right], \quad (2.18)$$

where subscript  $m$  is an index from 1 to the total number of non-neighboring connections

for each cell ( $N_{nnc}$ ). The flow potentials of a cell and its non-neighbouring cell are written as  $(p^\alpha - \rho^\alpha g z)$  and  $(p^\alpha - \rho^\alpha g z)^{nnc}$ , respectively. To determine the transmissibility factor ( $T^{nnc}$ ) between any pair of cells that are connected via non-neighboring connections, we need to estimate the area ( $A^{nnc}$ ), permeability ( $k^{nnc}$ ), and distance ( $d^{nnc}$ ) of the non-neighboring connections. This transmissibility factor is given as:

$$T^{nnc} = \frac{k^{nnc} A^{nnc}}{d^{nnc}}. \quad (2.19)$$

The equations to estimate  $A^{nnc}$ ,  $k^{nnc}$ , and  $d^{nnc}$  are different for different types of NNC. Moinfar et al. (2012) provides more details on these equations, as well as the expressions for the three types of NNCs in EDFM, which are shown in Figure 2.2. The projection-

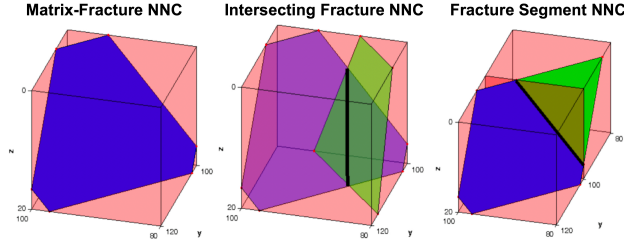


Figure 2.2. Types of NNCs in EDFM (Moinfar et al., 2012).

based EDFM (Tene, 2018) is based on an identification of neighboring projection cells onto which the fracture planes are projected, in addition to the host cell that contains the fracture. It extends the EDFM by adding two more NNC transmissibilities, which enables it to capture the effects of low-conductivity fractures. The first of these is the projection-matrix/fracture transmissibility ( $T_{pMF}$ ), which is given as:

$$T_{pMF} = \frac{A_{\perp x} K_{pMF}}{d_{pMF}}, \quad (2.20)$$

where the harmonic average of the projection matrix and fracture cell permeabilities

$(K_{\text{pMF}})$  is given as:

$$K_{\text{pMF}} = \frac{K_{\text{pM}} K_f}{K_{\text{pM}} + K_f}. \quad (2.21)$$

Here,  $d_{\text{pMF}}$  represents the distance between the centroid of the fracture and that of the projection cell, while  $A_{\perp x}$  is the area of the fracture projection along each spatial dimension.

The projection-matrix/host-matrix transmissibility ( $T_{\text{pMM}}$ ) is the second modification of the pEDFM, as is given as:

$$T_{\text{pMM}} = K \frac{A - A_{\perp x}}{\Delta \vec{x}_e}, \quad (2.22)$$

where  $\Delta \vec{x}_e$  represents the cell size in all three spatial directions (for 3D systems),  $A$  is the area of the face between the projection and the host matrix cells, while  $A_{\perp x}$  is the projection area. Olorode et al. (2020) presents a 3D pEDFM algorithm, and provides further details on its implementation for compositional reservoir simulation.

## 2.4. Molecular Diffusion Models.

This section provides details about different models to calculate the molecular diffusion flux for each component in a compositional reservoir simulation (such as Fick's law and hydrodynamic dispersion model). However, in this work, we model the true molecular diffusion using the dusty-gas model, where diffusion is driven by chemical potential and gravity gradients. It is considered robust and applicable in high-pressure reservoir systems (Schlumberger, 2018).

### 2.4.1. Diffusion Modeling Under Concentration Gradient

This section introduces the basic Fick's first law of molecular diffusion, which assumes diffusion is driven by the gradient of mass fraction of component  $i$  ( $X_i^\alpha$ ). Diffusion



flux in phase  $\alpha$  for component  $i$  ( $J_\alpha^i$ ) in a tortuous porous media is given by the following equation.

$$J_\alpha^i = -\frac{\phi S^\alpha}{\tau^\alpha} D_i^\alpha \rho^\alpha \nabla (X_i^\alpha). \quad (2.23)$$

where  $\phi$  is the matrix porosity,  $S^\alpha$  is the phase saturation, and  $\tau$  is the ratio of the actual length of the flow path in the porous medium to the thickness of the medium in the direction of the flow. We define  $(X_i^\alpha)$  as follows.

$$X_i^\alpha = \frac{M_i x_i^\alpha}{\sum_{j=1}^n M_j x_j^\alpha} \quad (2.24)$$

As we discuss in Subsection 2.4.3 that  $(f_i^\alpha)$  in Equation (2.37) is the true proxy to the chemical potential  $(\mu_i^\alpha)$ , and  $(X_i^\alpha)$  in Equation (2.23) is yet a pseudo-proxy to  $(\mu_i^\alpha)$ . Moreover, diffusion flux becomes zero when  $(\nabla X_i^\alpha)$  is zero, and this occurs while modeling a reservoir system where hydrocarbon species do not undergo any compositional changes, such as primary recovery. We then do not use Equation (2.23) in Chapter 3, where we implement different diffusion modeling for a primary system.

#### 2.4.2. Hydrodynamic Dispersion Modeling

A second molecular diffusion model is referred to the hydrodynamic dispersion, and it is defined as "the mixing of two miscible fluids caused by diffusion, local velocity gradients, locally heterogeneous streamline lengths and mechanical mixing in pore bodies (Lake et al., 2014)". Equation (2.25) calculates hydrodynamic dispersion flux of component  $i$  in phase  $\alpha$  ( $J_\alpha^i$ ) in a tortuous porous media.

$$J_\alpha^i = -\frac{\phi S^\alpha}{\tau^\alpha} D_i^\alpha \nabla (\rho^\alpha X_i^\alpha). \quad (2.25)$$

where the product  $\rho^\alpha X_i^\alpha$  is the mass concentration of component  $i$  in phase  $\alpha$ , and it replaces the  $(X_i^\alpha)$  in Equation (2.23).

### 2.4.3. Dusty-Gas Diffusion Model

Dusty-gas diffusion model is one of the most generalized molecular diffusion models that computes diffusion flux in porous media (Taylor and Krishna, 1993). By neglecting the viscous flow, pressure gradient, Knudsen diffusion, and electrostatic potential, we can re-write the dusty-gas diffusion such that it is driven by the gradients of (1) chemical potential, (2) gravitational potential and (3) temperature as we show in Equation (2.26) below (Schlumberger, 2018).

$$J_i^\alpha = -c^\alpha D_i^a x_i^\alpha \frac{1}{RT} \nabla [\mu_i^\alpha - M_i g(h - h_o) + M_i D_i^T \ln T] \quad (2.26)$$

Under isothermal fluid flow assumption, we re-write Equation (2.26) as follows.

$$J_i^\alpha = -c^\alpha D_i^a x_i^\alpha \frac{1}{RT} \nabla [\mu_i^\alpha - M_i g(h - h_o)] \quad (2.27)$$

Here,  $J_i^\alpha$ ,  $c^\alpha$ ,  $x_i^\alpha$  and  $\mu_i^\alpha$  are the diffusion flux, molar density, mole fraction, and chemical potential of component  $i$  in phase  $\alpha$ , respectively.  $M_i$  and  $D_i^a$  are molar mass and activity-corrected diffusion coefficient of component  $i$ , respectively. We derive an expression for  $D_i^a$  using Fick's law of diffusion, which is given by Equation (2.28) below (Fick, 1855).

$$J_i^\alpha = -c^\alpha D_i^\alpha \nabla x_i^\alpha \quad (2.28)$$

Here,  $D_i^\alpha$  is the effective diffusion coefficient of component  $i$  in phase  $\alpha$ . Equation (2.28) assumes diffusion flux is only driven by the gradient of component  $i$  composition ( $x_i$ ). In addition, it assumes the fluid flow is isothermal and horizontal; therefore, we can re-write Equation (2.26) under the latter assumptions as:

$$J_i^\alpha = -c^\alpha D_i^a x_i^\alpha \frac{1}{RT} \nabla \mu_i^\alpha \quad (2.29)$$

The real proxy to chemical potential for component  $i$  ( $\mu_i$ ) is fugacity of component  $i$  ( $f_i$ ) as we show in the relationship below (Firoozabadi, 2015).

$$\mu_i^\alpha = \mu_{io}^\alpha + RT \ln \left( \frac{f_i^\alpha}{f_{io}^\alpha} \right) \quad (2.30)$$

Substituting with Equation (2.30) in Equation (2.29), we write the diffusion flux ( $J_i^\alpha$ ) as follows

$$J_i^\alpha = -c^\alpha D_i^a x_i^\alpha \nabla \ln (f_i^\alpha) \quad (2.31)$$

Comparing Equation (2.31) to Equation (2.28), and utilizing the chain rule, we write an expression for  $D_i^a$  in terms of  $D_i^\alpha$  as Equation (2.32) shows below. We refer the reader to Schlumberger (2018) for more details on the intermediate steps.

$$D_i^a = \frac{D_i^\alpha}{\partial \ln (f_i^\alpha) / \partial \ln (x_i^\alpha)} = \frac{f_i^\alpha}{x_i^\alpha} \frac{D_i^\alpha}{\partial f_i^\alpha / \partial x_i^\alpha} \quad (2.32)$$

Next, Equation (2.27) has units of ( $\text{mol} \cdot \text{m}^{-2} \cdot \text{s}^{-1}$ ), which is inconsistent with the units of the other flux terms used in MRST compositional simulator ( $\text{kg} \cdot \text{m}^{-2} \cdot \text{s}^{-1}$ ). We next multiply both sides of Equation (2.27) by  $M_i$  as follows.

$$J_i^\alpha = -c^\alpha M_i x_i D_i^a \frac{1}{RT} \nabla [\mu_i^\alpha - M_i g(h - h_o)] \quad (2.33)$$

Since  $c^\alpha$  has the following expression,

$$c^\alpha = \frac{\rho^\alpha}{\sum_{i=1}^n M_i x_i^\alpha} = \frac{\rho^\alpha}{M} \quad (2.34)$$

we show that the quantity ( $c^\alpha M_i x_i$ ), shown in Equation (2.33), is equivalent to ( $\rho^\alpha X_i$ ),

where  $X_i$  is the mass fraction of component  $i$ .

$$c^\alpha x_i M_i = \frac{\rho^\alpha x_i M_i}{M} = \frac{\rho^\alpha M_i}{M} \left( \frac{n_i}{n_{\text{total}}} \right) = \frac{\rho^\alpha M_i}{M} \left[ \frac{\left( \frac{m_i}{M_i} \right)}{n_{\text{total}}} \right] = \frac{\rho^\alpha m_i}{m} = \rho^\alpha X_i \quad (2.35)$$

Now, we can re-write Equation (2.33) where  $J_i^\alpha$  has units of  $(\text{kg} \cdot \text{m}^{-2} \cdot \text{s}^{-1})$  as follows.

$$J_i^\alpha = -\rho^\alpha X_i D_i^a \frac{1}{RT} [RT \nabla \ln(f_i^\alpha) - M_i g \nabla z] \quad (2.36)$$

Here,  $\nabla z$  is the gradient of height difference in the Z direction. Furthermore, and to account for the porous tortuous reservoir media, we modify Equation (2.36) in the following final form.

$$J_i^\alpha = -\rho^\alpha X_i \frac{\phi S^\alpha}{\tau} D_i^a \frac{1}{RT} [RT \nabla \ln(f_i^\alpha) - M_i g \nabla z] \quad (2.37)$$

Under horizontal flow assumption, Equation (2.37) can be re-written as follows.

$$J_i^\alpha = -\rho^\alpha X_i \frac{\phi S^\alpha}{\tau} D_i^a \nabla \ln(f_i^\alpha) \quad (2.38)$$

Now, we can incorporate the diffusion flux ( $J_i^\alpha$ ), given by Equation (2.37), into our compositional simulation equation as we show below (Lake et al., 2014).

$$\partial_t \left[ \phi \sum_{\alpha=l,v} \rho^\alpha S^\alpha X_i^\alpha \right] + \sum_{\alpha=l,v} \nabla \cdot (\rho^\alpha X_i^\alpha \vec{v}^\alpha + J_i^\alpha) - \sum_{\alpha=l,v} \rho_\alpha X_i^\alpha q^\alpha / V = 0. \quad (2.39)$$

Diffusion flux term ( $J_i^\alpha$ ) in Equation (2.39) can be substituted for with any of the previously shown expressions in different diffusion models.

### Chapter 3. Diffusion Models Implementation for Primary Systems.

In this chapter, we study conditions under which diffusion contributes to production in primary recovery from unconventional reservoirs before investigating its role in our SDEOR technology. The wisdom is that physical processes must be fully understood and characterized for primary recovery before applied to EOR due to uncertainties of the recovery mechanisms involved (Thakur et al., 2019). Therefore, we first study how matrix permeability and mesh resolution affect the degree of molecular diffusion contribution to primary production systems before investigating the diffusion effect on our SDEOR technology.

We model diffusion for an ultratight dry gas reservoir completed by a vertical hydraulic fracture (HF) intersecting the reservoir section from top to bottom. Table 3.1 lists the reservoir parameters. Table A.1 and Table A.2 list reservoir fluid input parameters for Equation of State (EOS) and binary interaction coefficients, respectively. Figure 3.1 shows the reservoir 3D model. We model HF explicitly by assigning permeability and porosity values to fracture cells. We place a horizontal well across the reservoir’s central line in the middle of the HF, as denoted by the yellow grid in Figure 3.1. We simulate the reservoir for 15 years, where we plot the cumulative gas production versus time to study the effect of diffusion on production. Since hydrocarbon species do not undergo any compositional changes during primary recovery, we neglect diffusion modeling using Equation (2.23). In the next subsections, we study the effects of matrix permeability, grid resolution, and gravity on diffusion production contribution as modeled by Equations (2.25) and (2.37), respectively.

Table 3.1. Reservoir input parameters for diffusion model implementation for primary gas recovery.

Parameters	SI Unit	Field Unit
Reservoir Model Dimensions	$200 \times 150 \times 120$ m	$656.2 \times 492.1 \times 393.7$ ft
Grid Block Dimensions	$128 \times 9 \times 7$	$128 \times 9 \times 7$
Initial Reservoir Pressure, $p_i$	$3.4474\text{e}+7$ Pa	5,000 psia
Wellbore Flowing Pressure, $p_{wf}$	$3.4474\text{e}+6$ Pa	500 psia
Reservoir Temperature	355.84 K	180°F
Matrix Permeability, $k_m$	$9.87\text{e}-26$ m <sup>2</sup>	1e-9 D
Matrix porosity, $\phi$	0.063	0.063
Hydraulic fracture (HF) porosity, $\phi_{\text{frac}}$	0.50	0.50
HF half-length, $x_f$	75 m	246.1 ft
HF aperture, $w_f$	0.003 m	0.01 ft
HF height, $h_f$	120 m	393.7 ft
HF permeability, $k_f$	$9.87\text{e}-16$ m <sup>2</sup>	1e-3 D
Well radius, $r_w$	0.1 m	0.33 ft
Reservoir Fluid Components	$[C_1, C_2, C_3]$	-
Gas Diffusion Coefficients, $D_i^g$ Xiong et al. (2015)	$[2.8, 2.5, 1.9] \times 10^{-7}$ m <sup>2</sup> /s	$[3.01, 2.7, 2.04] \times 10^{-6}$ ft <sup>2</sup> /s
Components Initial Composition	$[0.991, 0.0088, 0.0002]$	-

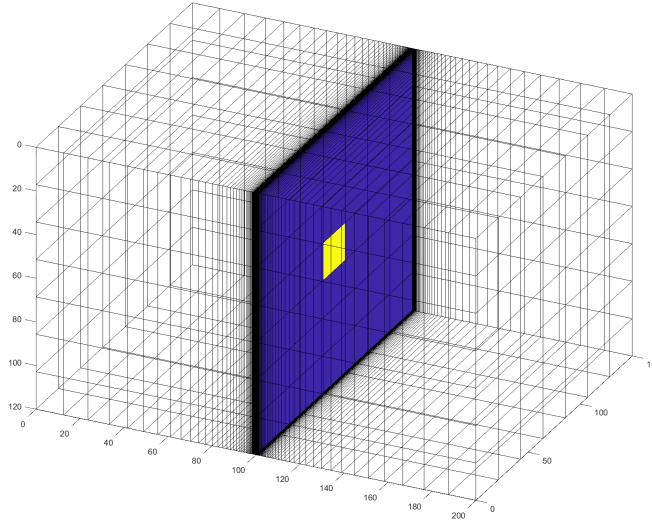


Figure 3.1. A reservoir model for primary gas production under diffusion modeling, where blue and yellow cells distinguish between HF and horizontal well locations, respectively

### 3.1. Effect of Matrix Permeability

Matrix permeability affects the degree of diffusion contribution to production gain.

Here, we study the effect of different matrix permeabilities in coarse and fine grid resolutions. Table 3.2 summarizes the percentage of gas production increase by the end of each

simulation run for diffusion models in Equations (2.25) and (2.37), respectively.

Table 3.2 and Table 3.3 summarize the results of diffusion models' contribution to gas production for different matrix permeabilities in a coarse grid ( $\times 64$ ) and fine grid ( $\times 1024$ ), respectively. Matrix permeability quantifies how much diffusion contributes to production. In ultratight reservoirs, the diffusion effect becomes considerable and adds to cumulative gas production. At lower matrix permeability and due to low flow velocity, diffusion of hydrocarbon species becomes a dominant transportation mechanism, in addition to advection. Conversely, at a higher matrix permeability, and due to high flow velocity, diffusion effects diminish, and advection mainly dominates the hydrocarbon transportation mechanism. Therefore, at  $100 \mu\text{D}$ , for instance, the flow velocity is high enough such that the advection mechanism dominates, and diffusion models only yield 0.00% and 0.31% gas production gain for coarse and fine grids, respectively. These results suggest that the effects of molecular diffusion diminish at higher matrix permeability, and the flow becomes advection-dominated. However, Cronin et al. (2020) argued that larger elements used in simulations could not capture small values of diffusion contribution to production at matrix permeabilities exceeding 10 nd. We proved the opposite to their findings in this work by using very small elements, or a high-resolution grid ( $\times 1024$ ), at higher matrix permeabilities and diffusion ceases to increase gas production as we show in Figure 3.2.

Figure 3.2 is a semi-log plot that shows the effect of matrix permeability on diffusion contribution for coarse and fine grids, respectively. The green line refers to hydrodynamic dispersion, as in Equation (2.25), and the red line refers to diffusion model under chemical potential gradient, as in Equation (2.37). Results suggest that dispersive flux adds more to gas production than diffusion flux in Equation (2.37) since the former cal-

Table 3.2. Percentage increase of gas production for different values of matrix permeabilities by modeling diffusion in a coarse grid ( $\times 64$ ).

Matrix Permeability	Diffusion Contribution to Gas Production, Equation (2.25)	Diffusion Contribution to Gas Production, Equation (2.37)
1 nD	9.4%	4.97%
10 nD	8.13%	2.69%
100 nD	3.9%	1.22%
1 $\mu$ D	0.50%	0.34%
100 $\mu$ D	0.00%	0.00%

Table 3.3. Percentage increase of gas production for different values of matrix permeabilities by modeling diffusion in a coarse grid ( $\times 1024$ ).

Matrix Permeability	Diffusion Contribution to Gas Production, Equation (2.25)	Diffusion Contribution to Gas Production, Equation (2.37)
10 nD	21.91%	2.22%
100 nD	14.99%	1.01%
1 $\mu$ D	1.63%	0.33%
100 $\mu$ D	0.314%	0.313%

culates the flux based on the gradient of  $(\rho^\alpha X_i^\alpha)$ , but the expression for  $(\rho^\alpha)$  is already dependent on the pressure (P) as follows.

$$\rho^\alpha = \frac{MP}{zRT} \quad (3.1)$$

Therefore, Equation (2.25) additionally accounts for the pressure gradient in calculating the dispersion flux, which was once accounted for in the mass flux term, so that it shows more contribution to gas production than the diffusion model given in Equation (2.37), and hence the difference between the green and red lines in Figure 3.2. Again, diffusion contribution diminishes when matrix permeability exceeds 1  $\mu$ D as advection dominates the mechanisms of hydrocarbon flow.



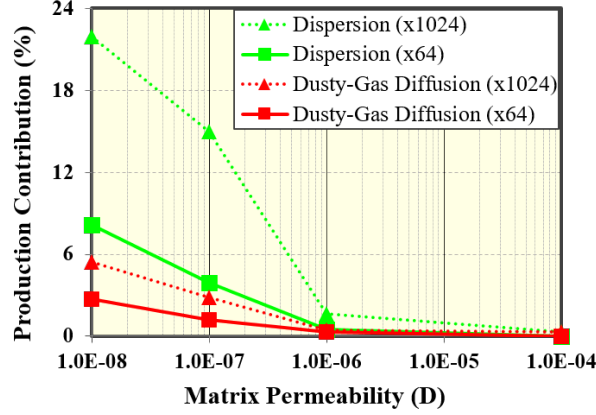


Figure 3.2. A semi-log plot for different matrix permeability affecting diffusion contribution to primary gas production gain under coarse ( $\times 64$ ) and fine ( $\times 1024$ ) grids.

### 3.2. Effect of Grid Resolution

In this subsection, and for the same reservoir and fluid parameters in Table 3.1, Table A.1, and Table A.2, we study the effect of grid resolution used in reservoir simulation on diffusion contribution to hydrocarbon recovery.

We refine the reservoir model in the X direction by systematically increasing the number of grids in that direction. Grids are geometrically spaced, and they start from the reservoir's X-axis midpoint to the reservoir's outer boundary (left or right) so that the length of the smallest grid equals half of the HF aperture. This gridding allows for HF explicit modeling by assigning permeability and porosity values for fracture cells. In this context, we refer to  $\times 16$  resolution, for instance, as a mesh setup such that there are 16 grids in the x-direction starting from the reservoir's midpoint to the boundary, and we have a total of 36 grids in the X-direction under  $\times 16$  resolution. Figure 3.4 refers to different levels of grid resolutions with a matrix permeability of 1 nD.

Table 3.4 summarizes the results of diffusion models' contributions to gas production for different levels of grid refinement. The results suggest that by increasing the grid

resolution, diffusion contribution to gas production increases because fine grids can correctly capture the transient changes occurring around the HF plane since it is the region with the highest pressure changes. Other low-resolution models are susceptible to truncation errors during the simulation and cannot capture the correct role of molecular diffusion. Figure 3.3 shows the effects of different diffusion models in contributing to cumulative gas production after 15 years of simulation. Again, dispersion flux, given in Equation (2.25), overestimates diffusion contribution than diffusion model given in Equation (2.37) as we discussed in the previous subsection.

Table 3.4. Percentage increase of gas production for different grid refinement resolutions by incorporating diffusion modeling.

Grid Resolution	Diffusion Contribution to Gas Production, Equation (2.25)	Diffusion Contribution to Gas Production, Equation (2.37)
$\times 16$	4.1%	6.07%
$\times 32$	4.71%	7.68%
$\times 64$	4.97%	9.40%
$\times 128$	5.23%	11.39%
$\times 256$	5.59%	13.32%
$\times 512$	6.04%	14.82%
$\times 1024$	6.50%	15.77%

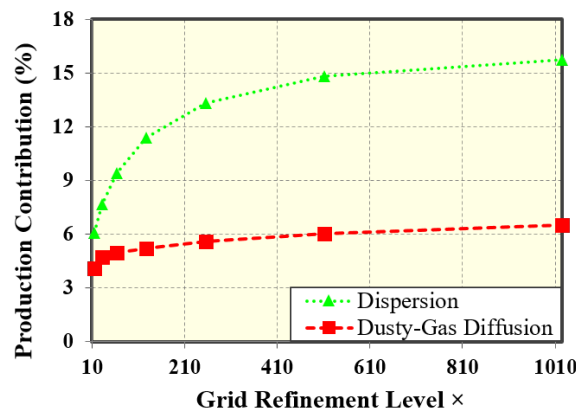
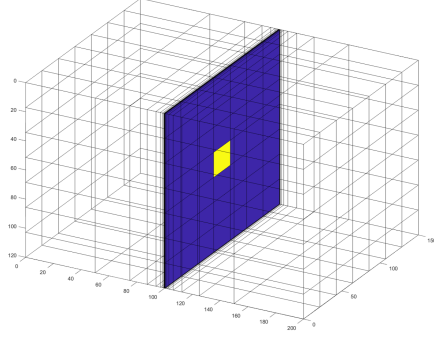
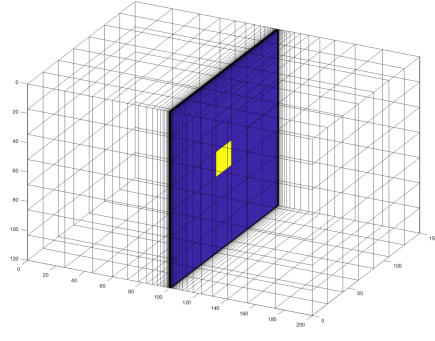


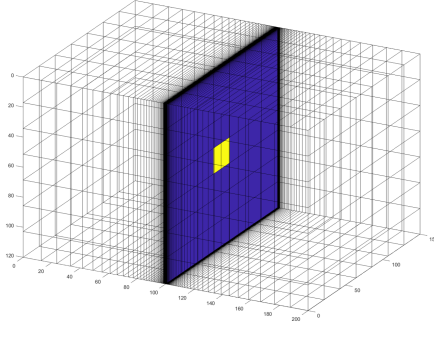
Figure 3.3. A Cartesian plot for different grid resolution levels ( $\times 16$ ,  $\times 32$ ,  $\times 64$ ,  $\times 128$ ,  $\times 256$ ,  $\times 512$ , and  $\times 1024$ ) affecting diffusion contribution to primary gas production gain: green line refers to dispersion flux from Equation (2.25) and red line refers to the dusty-gas diffusion model in Equation (2.37).



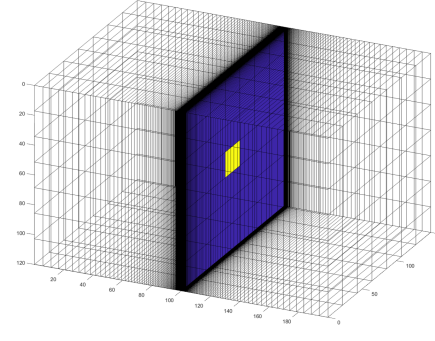
(a)  $\times 16$  Resolution



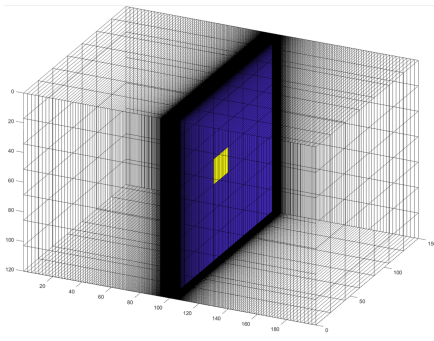
(b)  $\times 32$  Resolution



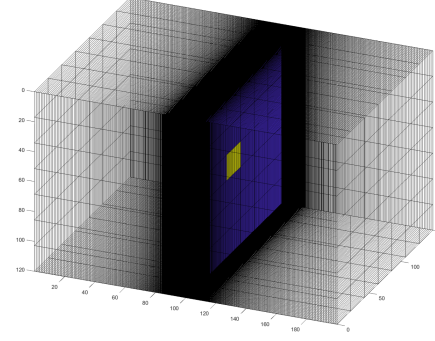
(c)  $\times 64$  Resolution



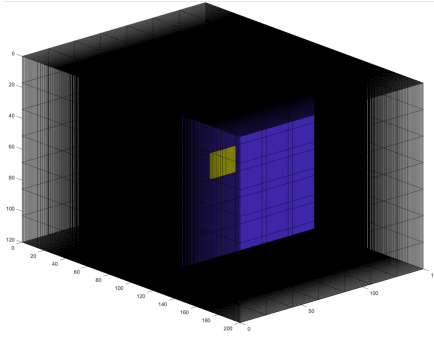
(d)  $\times 128$  Resolution



(e)  $\times 256$  Resolution



(f)  $\times 512$  Resolution



(g)  $\times 1024$  Resolution

Figure 3.4. Different levels of grid resolution ( $\times 16$ ,  $\times 32$ ,  $\times 64$ ,  $\times 128$ ,  $\times 256$ ,  $\times 512$  and  $\times 1024$ ): blue and yellow areas refer to HF cells and horizontal well location, respectively.

### 3.3. Effect of Gravity Segregation

In this subsection, we study the effect of gravity on chemical species distribution while modeling diffusion for primary gas recovery by simulating gas production for 15 years using the same reservoir parameters listed in Table 3.1, and with a grid resolution of  $\times 128$ . We compare results from Equation (2.37), which incorporates the gradient of gravitational potential, and Equation (2.38), which does not. Figure 3.5 shows  $C_1$  gas composition at the end of the simulation run for the two different equations, respectively. The gravity component term ( $M_i g \nabla z$ ) increases as we go from top to bottom, and hence the diffusion flux ( $J_i^\alpha$ ) decreases from top to bottom. Therefore,  $C_1$  has the least compositional changes in the bottom layer away from the HF plane, and this explains that  $C_1$  gas composition profile looks like an inverse-bell shape, as we show in Figure 3.5a. Nonetheless, while modeling diffusion without the gravity component as in Equation (2.38),  $C_1$  gas composition profile is homogeneously distributed from top to bottom and is symmetric across the HF plane, as we show in Figure 3.5b.

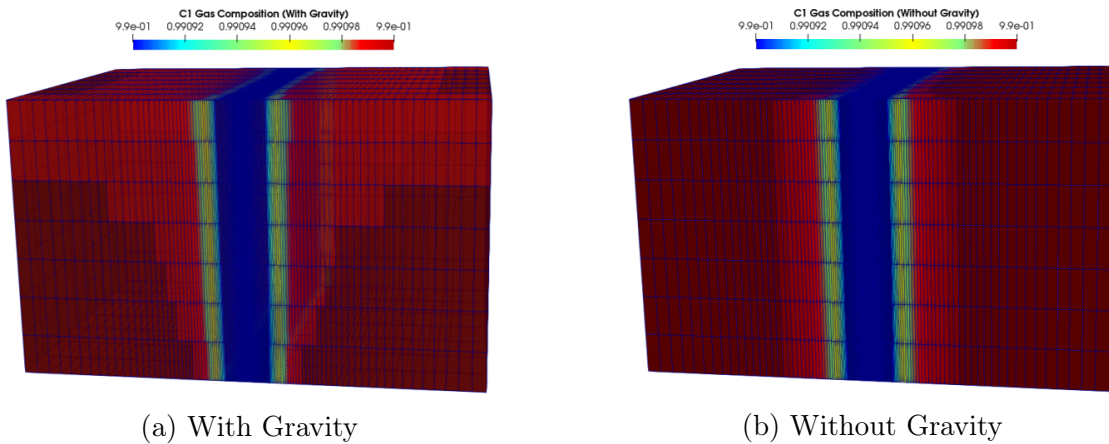


Figure 3.5.  $C_1$  gas composition after 15 years in a reservoir with matrix permeability of 1 nD and grid resolution of  $\times 128$ : (left) gravity modeled, as in Equation (2.37), and (right) without gravity, as in Equation (2.38).

## Chapter 4. Natural Fracture Network Connectivity and Uncertainty Analyses.

This chapter studies the effects of NF networks on SDEOR technology performance by computing the percolation threshold for a given NF network in a reservoir domain. First, we quantify the NF connectivity by introducing a computational algorithm to calculate the percolation threshold for the entire domain. Second, we apply the percolation theory to a primary production system for a well completed using the SD fracture. Third, we apply the percolation theory to quantify the uncertainty related to NF stochastic occurrence/conductivity in the reservoir and its effect on SDEOR technology performance. In this chapter, all simulation results are performed using MRST, where the generalized minimal residual method (GMRES) is used as a linear solver, and incomplete lower-upper (ILU) factorization is used as a pre-conditioner. In addition, the simulation runs capture the short-term production effects after eight years. Later, we present results for percolation theory application to SDEOR long-term production after 60 years in Section 5.1.

### 4.1. Computation of Percolation Threshold for Naturally-Fractured Reservoirs.

This section discusses NF network connectivity analysis for naturally-fractured reservoirs based on the dimensionless connectivity indices given in Haridy et al. (2019). Although Haridy et al. (2019) computed these indices for each cell in the reservoir, we extend the approach to compute the connectivity, crossing, and extended connectivity indices for the entire simulation domain as follows:

$$CI = \frac{\text{Total number of fracture-fracture intersections in the reservoir domain}}{\text{Total number of fractures in the reservoir}}, \quad (4.1)$$

$$CR_{i,j,k} = \frac{\text{Total number of matrix face-fracture intersections in x, y, and z directions}}{\text{Total number of fractures in the reservoir}}, \quad (4.2)$$

and

$$eCI_{i,j,k} = CR_{i,j,k} + CI. \quad (4.3)$$

In these equations,  $CI$ ,  $CR_{i,j,k}$ , and  $eCI_{i,j,k}$  are the connectivity, crossing, and extended connectivity indices, respectively. The subscripts  $i$ ,  $j$ , and  $k$  are used to indicate that the crossing and extended connectivity indices are computed for the x, y, and z-directions.

The connectivity index is computed by looping through all the fracture planes in the domain, counting the number of fracture-fracture intersections, and dividing that by the total number of fracture planes in the reservoir. The crossing index in the x-direction ( $CR_i$ ) is computed by looping through all the cell faces in the x-direction, counting the total number of fractures that intersect these faces, and dividing this by the total number of natural fractures in the reservoir simulation domain. The same procedure is repeated for  $CR_j$  and  $CR_k$ , except that we only use the y and z faces in these cases, respectively. The extended connectivity index ( $eCI_{i,j,k}$ ) is computed as the summation of  $CI$  and  $CR_{i,j,k}$ . Our computation of a scalar value for each of these indices in the entire domain facilitates the analysis of the fracture percolation threshold for fractured petroleum reservoirs, as we summarize in the following steps.

The density of a fracture network can be represented by fracture intensity, which can be characterized using different measures, as in Niven and Deutsch (2010). In this work, fracture intensity (in units of 1/ft, or  $\text{ft}^{-1}$ ) is calculated by summing the areas of all the natural fracture planes in the reservoir ( $A_i$ ), and dividing that by the bulk volume

of the reservoir ( $V$ ), as follows:

$$\text{Fracture Intensity} = \frac{\sum_{i=1}^n A_i}{V} \quad (4.4)$$

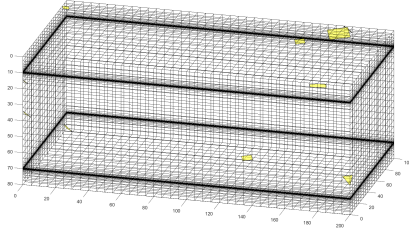
The level of connectivity of a fracture network can be assessed by computing its percolation threshold, which is the interval above which the fracture network begins to contribute significantly towards the production from the fractured reservoir. The steps required to determine the percolation threshold for a fractured reservoir stimulated using our proposed SDEOR method are as follows:

1. Set up a reservoir model such that each matrix cell has dimensions exceeding the average length of any given natural fracture (NF) plane. Tables 4.1, A.3, and A.4 list the reservoir, binary interaction coefficients, and compositional data used in the model.
2. Increase the number of NFs in the reservoir, ranging from 8, 16, 32, 64, 128, 256, 512, 750, 1024, to 1500.
3. Compute CI,  $\text{eCI}_{i,j,k}$  and fracture intensity (as in Equations (4.1), (4.3), and (4.4)) for each realization of the specified number of NFs, as shown in Figure 4.1.
4. Create a log-log plot of CI and  $\text{eCI}_{i,j,k}$  against fracture intensity (Figure 4.2).
5. Determine the percolation threshold at the fracture intensity range, where CI and  $\text{eCI}_{i,j,k}$  show a transition from a non-linear to a linear relationship (Haridy et al., 2019). This range is delineated by the two dashed green lines in Figure 4.2.

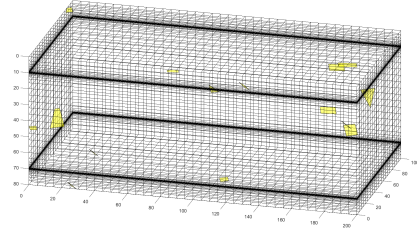
It is worth mentioning that in this and subsequent subsections of this work, the reservoir matrix is meshed as shown in Figure 4.1. The high resolution of the grids close to the top and bottom of the domain is to allow the modeling of a horizontal SD fracture close to the top of the reservoir (for gas injection) and a parallel SD fracture close to the bottom of the reservoir (for oil production). So, we use an explicit model for SD fractures where we assign permeability and porosity values for each fracture cell different than a matrix

cell. For the primary production cases studied in this subsection, we only consider an oil producer placed near the bottom of the reservoir and completed using one horizontal SD fracture. For SDEOR cases, we consider one gas injection well placed near the top of the reservoir alongside additional oil production well near the bottom of the reservoir.

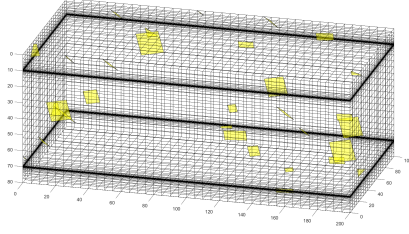




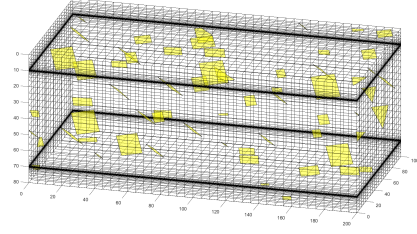
(a) 8 NFs



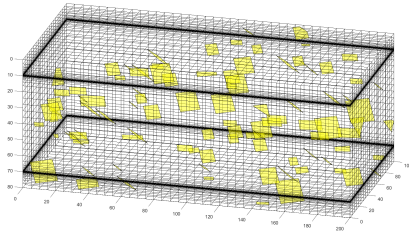
(b) 16 NFs



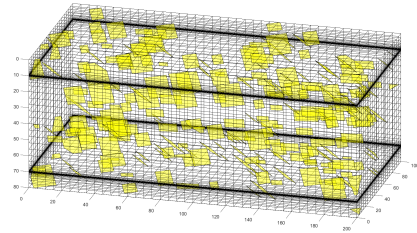
(c) 32 NFs



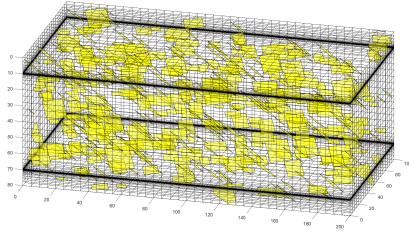
(d) 64 NFs



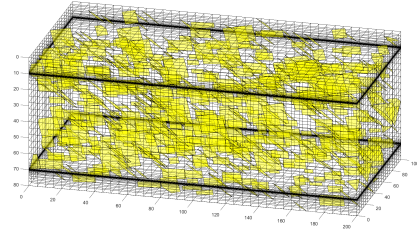
(e) 128 NFs



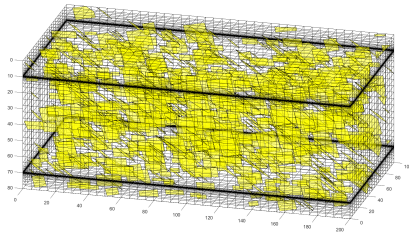
(f) 256 NFs



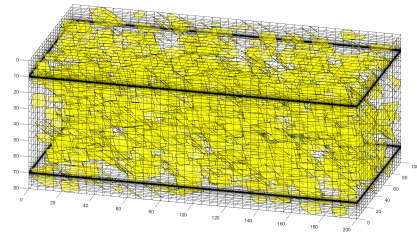
(g) 512 NFs



(h) 750 NFs



(i) 1024 NFs



(j) 1500 NFs

Figure 4.1. The images show fractured reservoirs populated with stochastic fractures ranging from as little as 8 to as many as 1500 natural fractures. Each image corresponds to one realization from a probabilistic distribution of the location, orientation, and size of the individual fractures that make up the fracture network with the specified number of fractures.

Following the enumerated steps, the percolation threshold is determined to be at a fracture intensity between  $0.005 \text{ ft}^{-1}$  and  $0.014 \text{ ft}^{-1}$ . This corresponds to having 70 to 260 natural fractures in the domain. At fracture intensity values above the percolation threshold, adding more stochastic fractures to the reservoir results in an appreciable contribution to hydrocarbon production. This contribution could be positive or negative, depending on the value of the fracture conductivity, as demonstrated in the following subsections.

#### **4.2. Application of Percolation Theory to Slot-Drilled Shale Reservoirs.**

We verify the applicability of the percolation theory by simulating eight years of primary oil production from a producing well, which is completed using an SD fracture near the bottom of the reservoir domain. Table 4.1 summarizes the input parameters for shale-oil reservoir simulated in this section, while Figure 4.3 presents the plots of the simulated oil recovery factor (RF) and cumulative oil production ( $N_p$ ) against fracture intensity. As expected, the RF and  $N_p$  increase when the fracture intensity exceeds the percolation threshold, illustrated with the dashed green lines. An inspection of Figures 4.1(g) - (j) (which correspond to the last four points in Figure 4.3) indicates that the fractures contribute to production at these significant numbers of connected fractures, which are above the percolation threshold. These connected fractures create a preferential path for the fluids in the porous medium to flow towards the well, thus increasing production appreciably. Below the percolation threshold, the contribution of the fractures to oil production is negligible because the fractures are scanty and disconnected from one another, as shown in Figures 4.1(a) - (d).

Table 4.1. Reservoir input parameters for the base case simulation

Parameters	SI Unit	Field Unit
Reservoir Model Dimensions	$200 \times 100 \times 80$ m	$656.2 \times 492.1 \times 393.7$ ft
Grid Block Dimensions	$40 \times 20 \times 78$	$40 \times 20 \times 78$
Initial Reservoir Pressure, $p_i$	$3.93\text{e}+7$ Pa	5,700 psia
Wellbore Flowing Pressure, $p_{wf}$	$1.7237\text{e}+7$ Pa	2,500 psia
Reservoir Temperature	353 K	175°F
Matrix Permeability, $k_m$	$9.85\text{e}-18$ m <sup>2</sup>	10e-6 D
Matrix porosity, $\phi$	0.07	0.07
Injection Rate, $q_{inj}$	$0.003277$ m <sup>3</sup> /s	10,000 scf/D
Well radius, $r_w$	0.1 m	0.33 ft
# NFs (Base Case)	256	256
NF porosity, $\phi_{NF}$	0.5	0.5
NF permeability, $k_{NF}$	$9.83\text{e}-16$ m <sup>2</sup>	1e-3 D
NF aperture, $w_{NF}$	$3.05\text{e}-3$ m	0.01 ft
# SD fractures	2	2
SD fracture porosity, $\phi_{SD}$	0.33	0.33
SD fracture permeability, $k_{SD}$	$9.87\text{e}-12$ m <sup>2</sup>	10 D
SD fracture aperture, $w_{SD}$	0.01 m	0.033 ft
SD fracture Spacing	60 m	196.85 ft

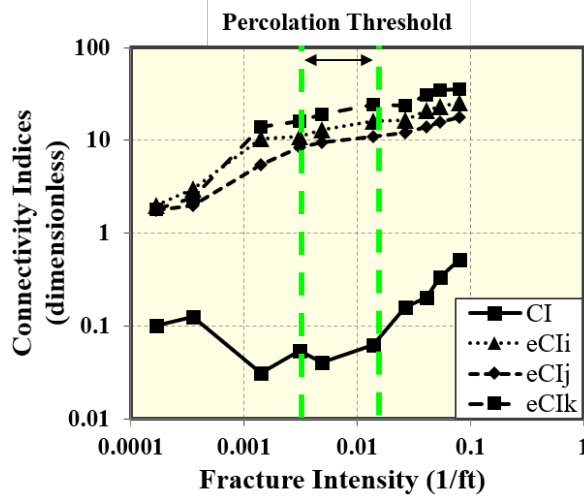


Figure 4.2. A log-log plot of CI and  $eCI_{i,j,k}$  against fracture intensities. Each point in this figure corresponds to the natural fracture networks shown in Figure 4.1. The dashed green lines indicate the fracture intensity range that defines the percolation threshold.

To explain why natural fractures do not contribute appreciably to production when the fracture connectivity is below the percolation threshold, we modify Equations (4.1),

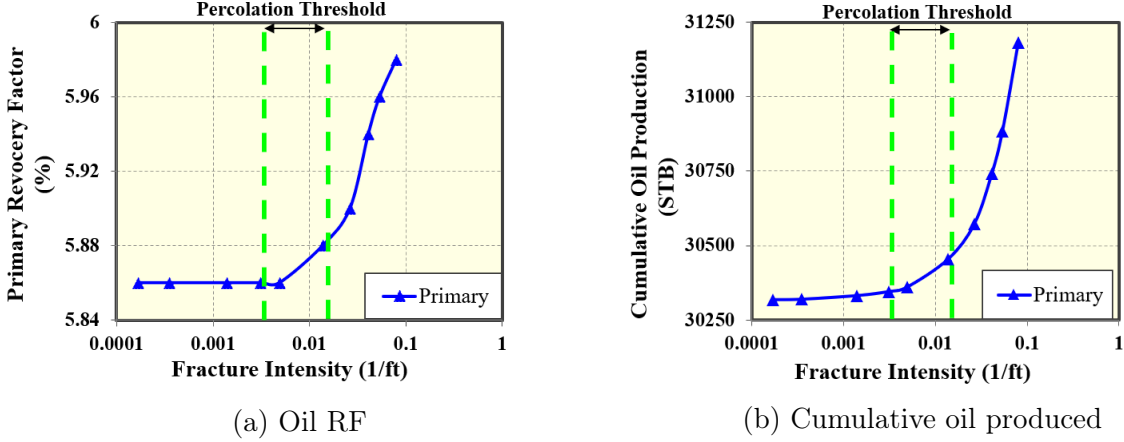


Figure 4.3. The oil recovery factor and cumulative oil production plots show increased production when the fracture intensity exceeds the percolation threshold. The dashed green lines indicate the percolation threshold.

(4.2), and (4.3) to calculate the connectivity indices per cell, instead of the entire domain.

The modified equations are as follows:

$$CI_{\text{cell}} = \frac{\text{Total number of fracture-fracture intersections in the matrix cell}}{\text{number of fracture planes in the matrix cell}} \quad (4.5)$$

$$(CR_{i,j,k})_{\text{cell}} = \frac{\text{Total number of matrix face-fracture intersections in x, y and z directions}}{\text{number of fracture planes in the matrix cell}} \quad (4.6)$$

$$(eCI_{i,j,k})_{\text{cell}} = (CR_{i,j,k})_{\text{cell}} + CI_{\text{cell}} \quad (4.7)$$

Figure 4.4 presents the  $eCI_{k_{\text{cell}}}$  values (calculated using Equation (4.7)) for 16 and 512 natural fractures, which are respectively below and above the percolation threshold. The focus on the extended connectivity index in the z-direction is as fluid flow is established following the pressure differential between the top injector and bottom producer as we discuss the SDEOR main recovery mechanism. As shown in Figure 4.4a, the system with 16 natural fractures illustrates the limited fracture connectivity between the fractured producer near the bottom of the reservoir and fluids farther away from it. The legend in this Figure shows that most of the matrix cells have  $eCI_k$  values of zero. In contrast, Figure

4.4b shows a system of 512 natural fractures, where the  $eCI_k$  values are greater than zero in several matrix cells, which means that more NF planes are capable of crossing the cell boundaries in the Z direction. This figure provides visual evidence for the significant connectivity of the fractures in reservoirs that have fracture intensities above the percolation threshold. It is also in agreement with the results presented previously in Figure 4.3.

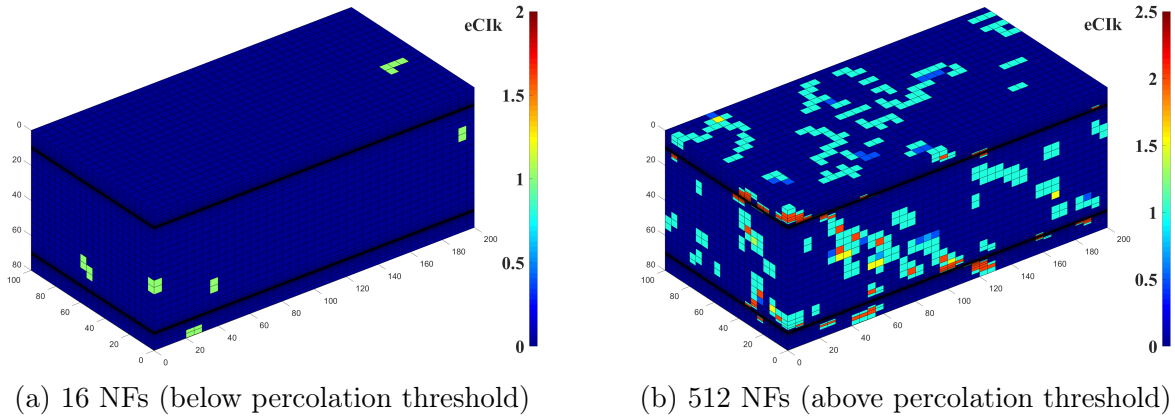


Figure 4.4. The plots of  $eCI_k$  for each matrix cell show the poor and high fracture connectivities at (left) 16 and (right) 512 natural fractures, respectively.

### 4.3. Natural Fracture Network Conductivity Analyses.

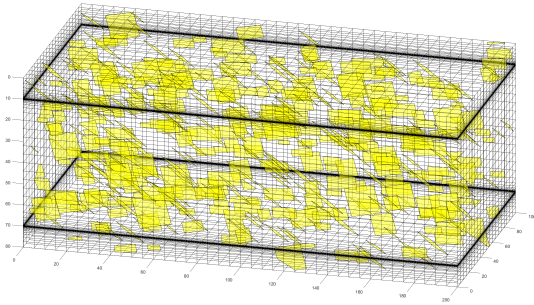
This subsection presents the simulation results of the continuous injection of methane gas into an SD fracture close to the top of the fractured reservoir while simultaneously producing oil from the SD fracture close to the bottom of the reservoir. Considering that there is currently no technology available to locate all the natural fractures in the subsurface, we simulate a few realizations of the same number of natural fractures and evaluate the effect of the uncertainties in the fracture properties (such as location, orientation, and size) on production. For example, Figure 4.5 provides different realizations of 512 NFs occurrence, and shows that even with a specified average fracture dip and strike, fracture properties can vary. This work also accounts for the fact that the



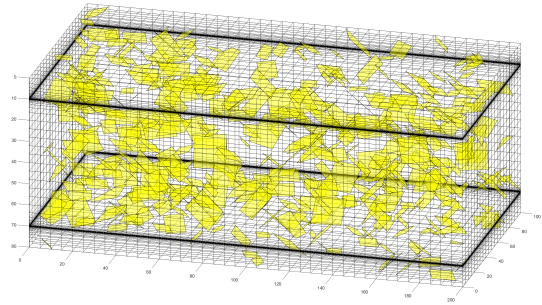
conductivity of natural fractures could vary widely, ranging from highly conductive to very low conductive fractures or fractures with mixed conductivities. Table 4.2 presents the permeability and conductivity values for the high and low conductive fractures used in this subsection.

Table 4.2. Different NF network conductivities for  $k_m = 1\text{e-}2$  md.

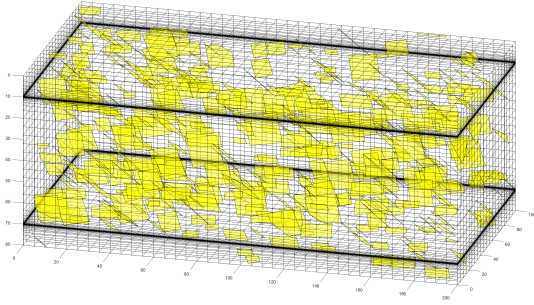
NF Network Type	NF Permeability (md)	NF Conductivity (md·ft)
High Conductive	10	1
Low Conductive	1e-5	1e-6



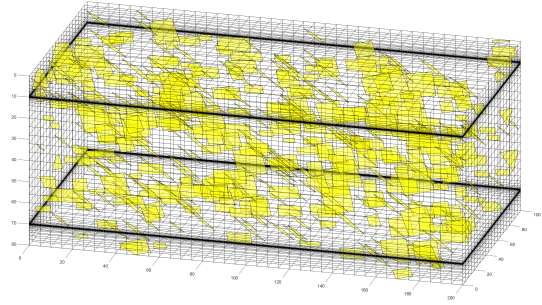
(a) realization #1



(b) realization #2



(c) realization #3



(d) realization #4

Figure 4.5. Images illustrate different realizations of 512 natural fractures, which are used for uncertainty analysis.

#### 4.3.1. Study of SDEOR performance in reservoirs with only high-conductivity natural fractures

Figure 4.6 provides a box-plot that quantifies the uncertainty in the recovery factor from SDEOR in a reservoir model with several realizations of highly conductive NFs

only. It shows that within the eight years of simulated production, the recovery factor remains above 13.64%, regardless of the number of fractures simulated. This indicates that the proposed SDEOR method is applicable regardless of the amount of conductive natural fractures in the domain. As the number of conductive fractures increases above the percolation threshold, the recovery factor slightly increases. This is in agreement with the role of fractures in enhancing oil recovery in a gravity drainage process. Comparing the SDEOR recovery factor to its corresponding value during primary recovery (which is 5.9% from Figure 4.3a), it is clear that continuous methane gas injection through our proposed technology results in a two-fold increase in production over only eight years of production.

To provide further insight into the SDEOR process in fractured shale-oil reservoirs, we present the profile of methane in Figure 5.3. The image on the left shows an almost piston-like displacement when the number of fractures in the domain is negligible (16 NFs in this case). However, as the number of fractures increases, the injected methane flows to various parts of the reservoir, as in Figure 4.9b. Here, the network of 512 NFs is able to transport the methane gas towards the top of the formation due to buoyancy (i.e., upward migration). This could lead to the formation of a secondary gas cap if the process is simulated for a much longer duration than the eight years simulated in this case. Subsequent sections will involve simulating injection and production for up to 60 years in order to study the long-term performance of our proposed SDEOR technology.

#### **4.3.2. Study of SDEOR performance in reservoirs with only low-conductivity natural fractures**

Figure 4.7 provides a box-plot that shows how the oil recovery factor for the SDEOR changes as the number of low-conductive fractures increases. To account for the

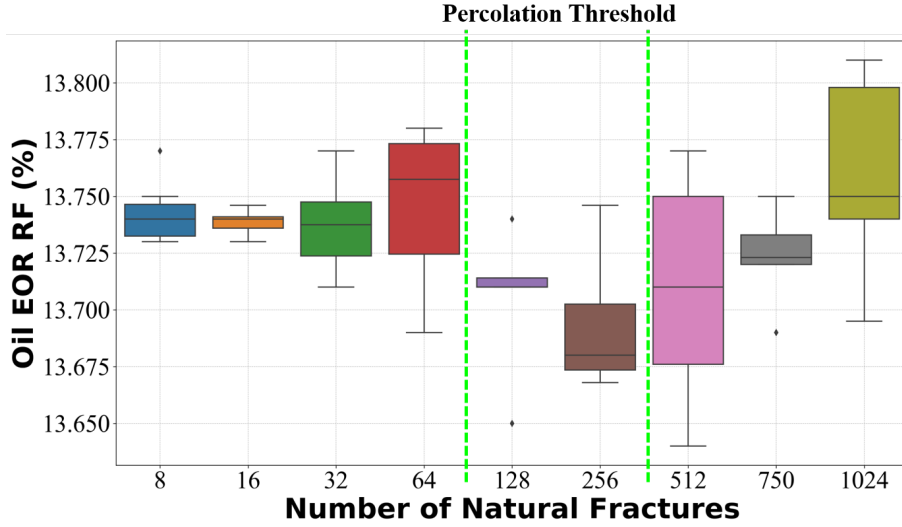


Figure 4.6. Results indicate a small variation in the oil recovery factor as the number of high-conductivity fractures increases from 8 to 1024. Several realizations are simulated to quantify the uncertainty associated with different realizations of these conductive natural fracture networks.

uncertainty in the fracture location, orientation, and permeability, we simulated several different realizations for each given number of natural fractures. The results show that although the oil recovery factor decreases slightly as the number of fractures increases, the proposed SDEOR technique still provides a two-fold increase in recovery (compared to the primary recovery factor of 5.9%) even with up to 1024 sealing fractures.

#### 4.3.3. Study of SDEOR performance in realistic reservoirs with stochastic distribution of fracture conductivity

Considering that the fractures in shale-oil reservoirs were formed under different prevailing stress states and at different points in their geologic history, these fractures could vary over a wide range of conductivity. To account for this uncertainty in fracture conductivity, we simulate a case with 1024 NFs and with the mixed fracture conductivity such that high conductivity fractures have permeability values sampled from a normal distribution with a range of 10 md to 100 md. Meanwhile, low conductivity fractures have a



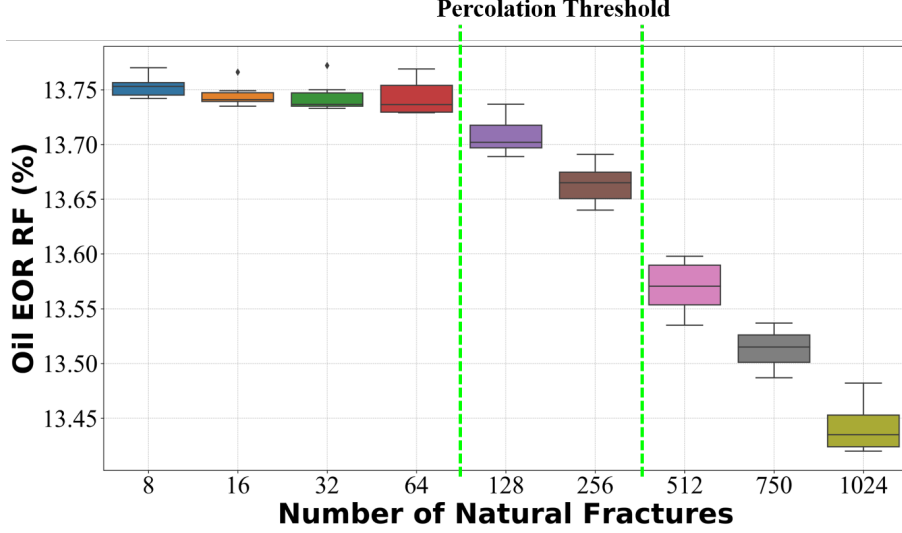


Figure 4.7. A box-plot for quantifying the uncertainty of SD-EOR oil RF associated with different realizations of low-conductive NF networks.

permeability range between 1 nd and 100 nd. The high-conductivity fractures have permeability values sampled from a normal distribution with a mean of 82 mD and standard deviation of 52 mD, while the low-conductivity fractures have a mean and standard deviation of 9 nD and 6 nD, respectively. The aperture ( $w_f$ ) of each fracture in the network is computed from the cubic law for fracture permeability ( $K_f$ ) as follows:

$$w_f = \sqrt{12K_f} \quad (4.8)$$

We use Equation (4.8) to make sure that each NF has an aperture value consistent with its corresponding permeability ( $K_f$ ) and hence conductivity ( $K_f w_f$ ). For instance, high-conductive NFs must have larger  $w_f$  than low-conductive ones. Figure 4.8 provides a box-plot that shows the oil recovery factor for SDEOR for three cases of high, mixed, and low fracture conductivities with different realizations. Again, and in all three cases, SDEOR technology can double oil RF (compared to primary production) regardless of stochastically existing fractures at any conductivity after eight years, as demonstrated in this sec-

tion.

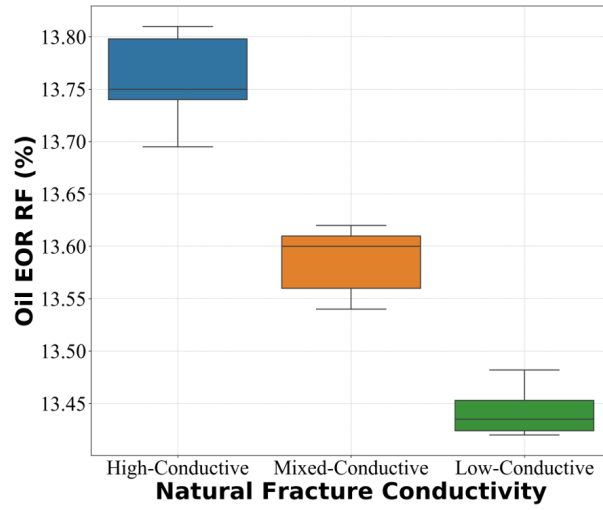


Figure 4.8. Results indicate the robustness of our SDEOR technology when applied to a tight rock with 1024 fractures of high-conductivity, low-conductivity, or with mixed conductivity. For this extreme case of 1024 NFs, EOR oil RF only varies from 13.42% to 13.81% after 8 years of simulation.

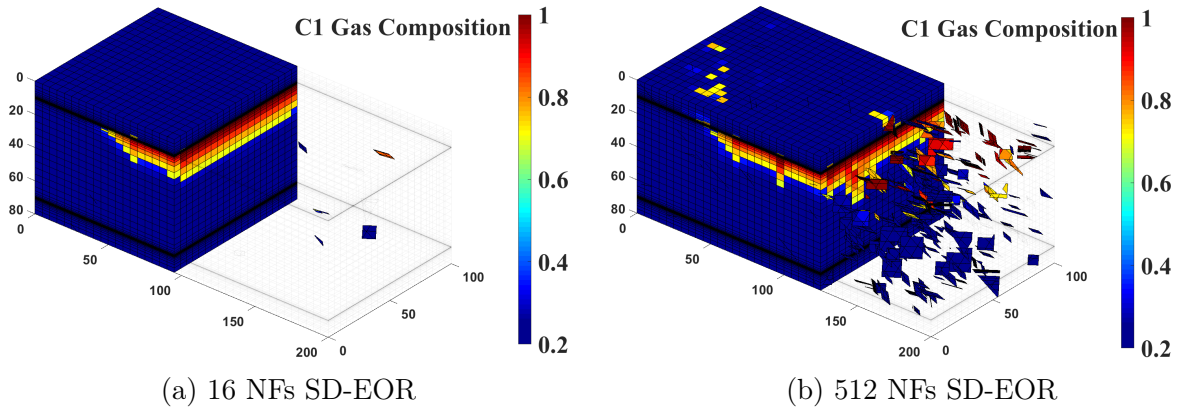


Figure 4.9. Reservoir grid visualizations for  $C_1$  gas composition by the end of 8 years SD-EOR simulation for conductive fracture networks: 16 NFs case (top) and 512 NFs case (bottom).

## **Chapter 5. SDEOR Simulation Results for Fractured Shale Formations.**

This chapter presents and discusses different simulation studies for the SDEOR technology. I start by presenting the long-term simulation to study the performance of SDEOR technology in fractured formations. I next present studies to evaluate the recovery mechanisms involved in the SDEOR technology. Subsequent sections discuss the effect of matrix heterogeneity, SD fracture conductivity, and the waterflooding applicability for the SDEOR technology. Finally, I compare the performance of the SDEOR to the CGEOR method when applied to representative unconventional reservoirs (such as Bakken and Eagle Ford shale-oil formations).

### **5.1. Simulation Study of the Long-term Performance of the SDEOR Technology.**

In this subsection, we assess the long-term performance of the proposed SDEOR technology in fractured shale-oil reservoirs by simulating up to 60 years of production. Figure 5.1 presents the plots of the cumulative oil and gas production for a base-case simulation with no natural fractures, a primary recovery case, as well as a case with 64 natural fractures (which is below the percolation threshold), and another with 1024 fractures, which is well above the percolation threshold determined from the previous subsection. Compared to the primary recovery (green line), this figure shows that SDEOR results in a drastic increase in cumulative oil production, regardless of the number of natural fractures in the reservoir. Performing the simulation for up to 60 years shows the long-term effectiveness of the proposed technology because the cumulative oil production increases at a constant rate for 30 years. It is worth noting that the injected gas does not break through

before approximately 25 years of production (even with as many as 1024 conductive natural fractures), and the cumulative gas production is the same in all SDEOR cases after 40 years of production. This is because of the role gravity plays in stabilizing the gas front and preventing early gas breakthrough through the fracture network.

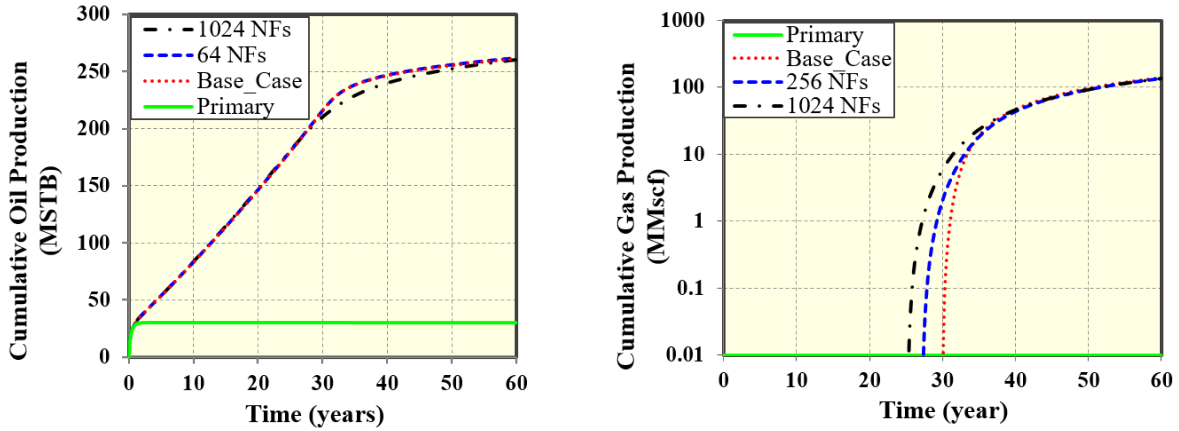


Figure 5.1. These performance plots show the long-term effectiveness of the SDEOR technology, regardless of the presence of natural fractures. The results show that the oil production does not decline until after 30 years, and gas does not break through until after 25 years.

To further show the robustness of SDEOR in the presence of natural fractures ranging from 0 to 1024 and at different times in the life of the reservoir (at 8, 15, 30, and 60 years), we provide a plot of the SDEOR recovery factor in Figure 5.2. The nearly horizontal nature of this plot in the near and long term buttresses the conclusion that the recovery does not depreciate appreciably regardless of the presence or amount of natural fractures in the reservoir. The red triangles plotted on the y-axes correspond to the base case with no natural fractures, which technically corresponds to a case with zero fracture intensity. Figure 5.3 shows the time evolution of the injected methane gas profile after 8, 15, 30, and 60 years in a reservoir with no natural fractures (base case) and another with

1024 fractures. As time advances, the injected methane composition migrates towards the bottom producer, while some of this gas also moves to the top of the reservoir due to buoyancy.

Table 5.1 summarizes the performance results of the SDEOR technology by comparing its recovery factor with those from primary production. We also provide the change in recovery factor (relative to primary recovery), as well as the IOR ratio, which can be as high as 8.58 after 60 years of production. To show the game-changing potential of the SDEOR technology in comparison to the application of CGEOR in use today, the next section provides a comparison of both technologies using the same reservoir model.

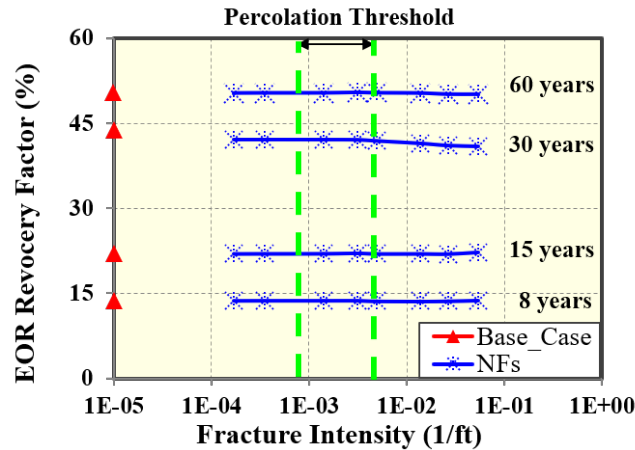


Figure 5.2. The blue lines show that the EOR recovery factor stays almost constant regardless of the fracture intensity but increases over time as expected. The red triangles on the y-axis indicate the corresponding recovery factor for a case with no fractures (zero fracture intensity). The percolation threshold is shown as the interval between the two green lines.

Table 5.1. SD-EOR performance summary under different flooding periods in a reservoir with 1024 conductive NFs.

Flooding Period (years)	Primary Oil	SDEOR Oil	Increased Oil RF (%)	IOR Ratio
	RF	RF (1024 NFs)		
8	5.48	13.75	+8.27	2.37
15	5.48	22.15	+16.67	3.79
30	5.48	40.95	+35.47	6.94
60	5.48	50.14	+44.66	8.58

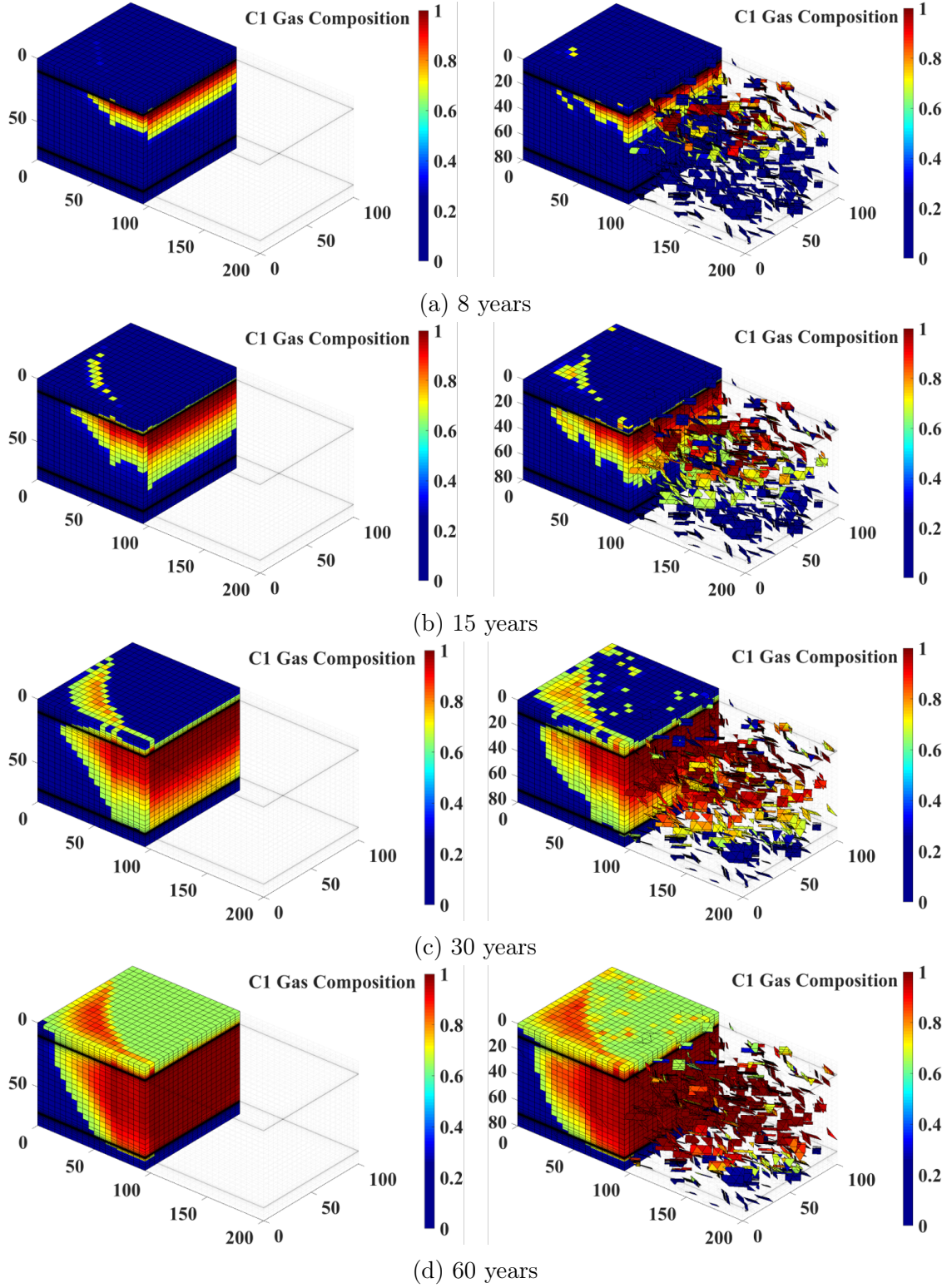


Figure 5.3. These profiles show how the methane gas composition evolves for a base case without natural fractures (left column) and for a case with 1024 conductive fractures (right column).

## 5.2. Performance Comparison Between CGEOR and the SDEOR technology.

This section compares our proposed technology’s production performance to the CGEOR method used in multistage hydraulically fractured (MSHF) horizontal wells. The compositional fluid parameters and binary interaction coefficients used in both SDEOR and CGEOR models are provided in Tables A.3 and A.4. To make a meaningful comparison between these two EOR technologies, we ensured that the total surface area of all the fractures in the CGEOR model shown in Figure 5.4 is equal to the area of one slot-drilled fracture shown in Figure 1.5a. The completion parameters for the slot-drilled fracture are presented in Table 4.1, while those for the MSHF wells are summarized in Table 5.2. Unlike the previous SDEOR simulation results presented in previous sections, this case was simulated at the same injection and flowing bottomhole pressures for the CGEOR case (in Table 5.2). Although methane gas is injected in both methods, SDEOR involves continuous gas injection, whereas in CGEOR, we simulated injection, soaking, and production for 25, 5, and 70 days, respectively. As reported in Jacobs et al. (2019), this approach of minimizing the duration of injection and soaking is typically optimal in CGEOR. So, we use an optimal CGEOR operation schedule to avoid artificially making the CGEOR suboptimal.

Figure 5.5 shows that the primary production from both slot-drilled and hydraulically fractured wells are practically identical because both methods model the same total fracture surface area. The other plots in this figure show that SDEOR yields much higher oil production and less much less gas than CGEOR. The increased oil production could yield a sharp increase in the revenue from unconventional oil reservoirs, while the reduced gas production will minimize the costs of handling the associated gas. The slope of the left



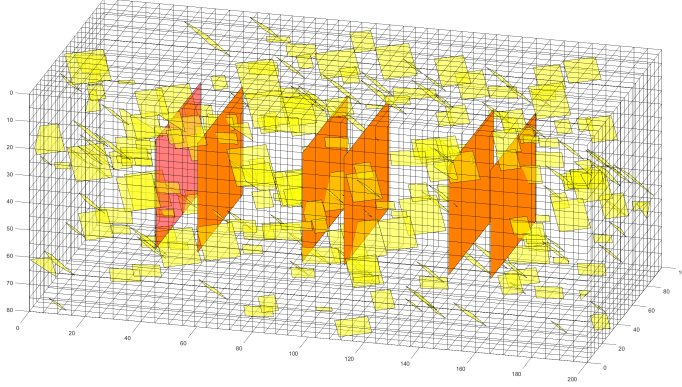


Figure 5.4. Image shows the simulation domain for the CGEOR method. The natural fractures are shown as yellow planes, while the hydraulic fractures are shown as red vertical planes.

Table 5.2. Input parameters for CGEOR in MSHF completion

Parameters	Field Unit	SI Unit
Injection Pressure, $P_i$	6,700 psia	4.6195e+7 Pa
Wellbore Flowing Pressure, $P_{wf}$	2,500 psia	1.7237e+7 Pa
Fracture half-length, $x_f$	98.4252 ft	30 m
Fracture width, $w_f$	0.00984 ft	0.003 m
Cluster spacing	49.21 ft	15 m
Fracture spacing	123.03 ft	37.5 m
Fracture permeability, $k_f$	1000 md	9.9 E-14 $m^2$
Fracture porosity, $\phi_{frac}$	0.5	0.5
Well radius, $r_w$	0.32 ft	0.1 m
Injection period (Jacobs et al., 2019)	25 days	25 days
Soaking period	5 days	5 days
Production period	70 days	70 days
Cycle duration	100 days	100 days

image changes after 4.5 years because the gas breaks through, as shown in the right image.

Table 5.3 further quantifies the magnitude of the increase in recovery from the SDEOR in comparison to the CGEOR technology. It shows that over the first eight years of production, our proposed SDEOR technology yields three times more oil than the CGEOR method and 12 times more oil than primary oil production. This drastic increase in the EUR from SDEOR in comparison to CGEOR could be attributed to the role gravity plays

in stabilizing the gas front in fractured unconventional reservoirs, as well as the fact that CGEOR only produces oil for a fraction of the life of the well and is either shut-in or injecting gas at other times.

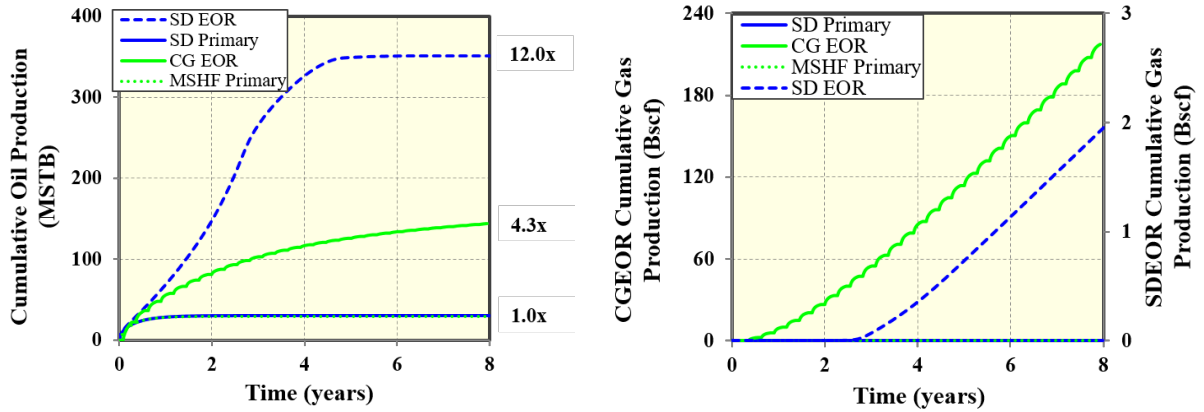


Figure 5.5. The results show that SDEOR yields three times more oil than CGEOR, and half as much of associated gas production. The primary recovery from the slot-drilled and MSHF wells match because the total fracture area is the same in both cases.

Table 5.3. Performance comparison between SDEOR and CGEOR after 8 years.

Recovery Mechanism	Oil RF (%)	EUR (Mstb)	IOR Ratio
Primary	6	30	N/A
CGEOR	26	131	4.3
SDEOR	70	352	12

Figure 5.6 presents the methane gas profile after eight years of simulation for both EOR techniques. The left image shows that the injected gas efficiently displaces the oil towards the slot-drilled fracture at the bottom of the reservoir. The red-colored cells delineate the portions of the reservoir that have been swept by the injected gas. The presence of some blue-colored cells in the domain after eight years indicates that we could recover more oil if the simulation is run for longer periods. The methane gas profile on the right of Figure 5.6 shows that some of the injected gas gets to the boundary of the domain af-

ter eight years of simulated production. Figure 5.7 presents slices of the domain in the x- and z-directions. It shows that the injected gas travels horizontally in the reservoir as expected. The concentration of methane gas near the fracture surfaces results in high and low relative permeabilities to gas and oil, respectively. This consequently leads to a reduced oil flow and an increased gas flow towards the hydraulically fractured well and is a fundamental limitation of the CGEOR method. The use of a pair of slot-drilled fractures in the SDEOR technology avoids this limitation. The marked change in relative permeability explains why the cumulative oil production from SDEOR continues to increase while that of CGEOR flattens out, and the well produces a lot more gas instead (as shown in Figure 5.5).

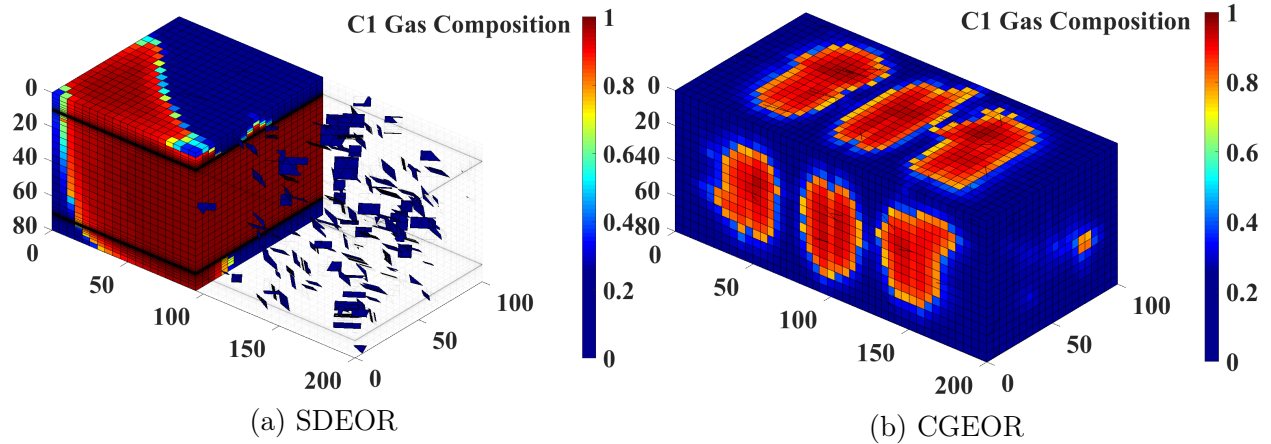


Figure 5.6. Left image shows the methane gas profile after 8 years of simulated SDEOR while right image shows the corresponding methane profile from the CGEOR method.

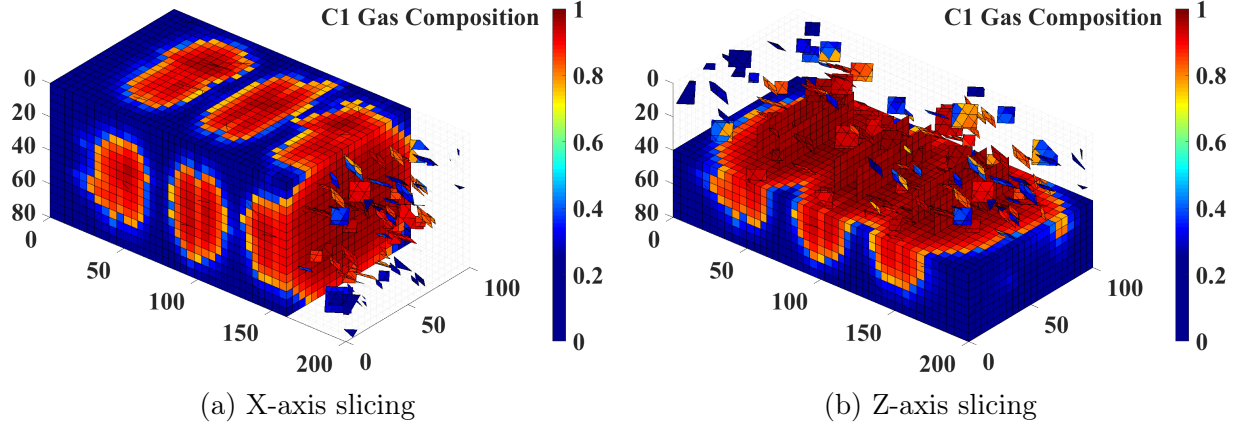


Figure 5.7. Left image shows the profile for the methane mole-fraction, with the last 8 cells in the x-direction taken out, while the right image cuts out half of the matrix cells above the middle of the reservoir. It shows that the methane gas saturates the pore volume in the vicinity of the hydraulic fracture clusters, leading to the limited performance of the CGEOR method.

### 5.3. Evaluation of the Recovery Mechanisms in SDEOR.

In this section, we study the role of different EOR mechanisms in the proposed SDEOR technology. Understanding the physical mechanisms that control the performance of the SDEOR process could facilitate the design of efficient field implementation of this technology. Here, we focus on four main recovery mechanisms:

1. Pressure-driven recovery
2. Gravity drainage
3. Molecular diffusion
4. Oil viscosity reduction

#### 5.3.1. The Role of the Pressure Difference Between the Injector and Producer.

The magnitude of the pressure difference between the injector and the producer wells ( $\Delta P_{\text{diff}}$ ) controls the oil recovery efficiency under the SDEOR technology application in shale formations. In the following, We study the role of  $\Delta P_{\text{diff}}$  created by injecting at

either a constant pressure ( $P_{inj}$ ) or a constant injection rate ( $q_{inj}$ ), or by producing at different flowing bottomhole pressures ( $P_{wf}$ ).

### **Effect of Injection Pressure ( $P_{inj}$ ).**

First, we assess the role of  $\Delta P_{diff}$  in SDEOR oil recovery due to different ( $P_{inj}$ ) by simulating a reservoir producing at a constant  $P_{wf}$  of 2,500 psia for eight years, given that  $P_{inj}$  exceeds the initial reservoir pressure ( $P_i$ ) with a pressure difference of  $\Delta P_{inj}$ . In Figure 5.8, we show simulation results for cases corresponding to  $P_{inj}$  from 5,700 to 7,700 psia, and hence a  $\Delta P_{inj}$  range between 3,200 to 5,200 psia. Although  $\Delta P_{diff}$  controls how rapid injection gas saturates the region between the top and bottom SD fractures, the cumulative oil production converges to the same value of 366 MSTB (which corresponds to an oil RF of 71.6% and an IOR ratio of 12.13) for all the simulated cases. Lower  $\Delta P_{diff}$  results in lower cumulative gas production, as shown in Figure 5.8b, which could be a vital criterion in reducing the handling cost of the associated produced gas from the SDEOR proposed technology.

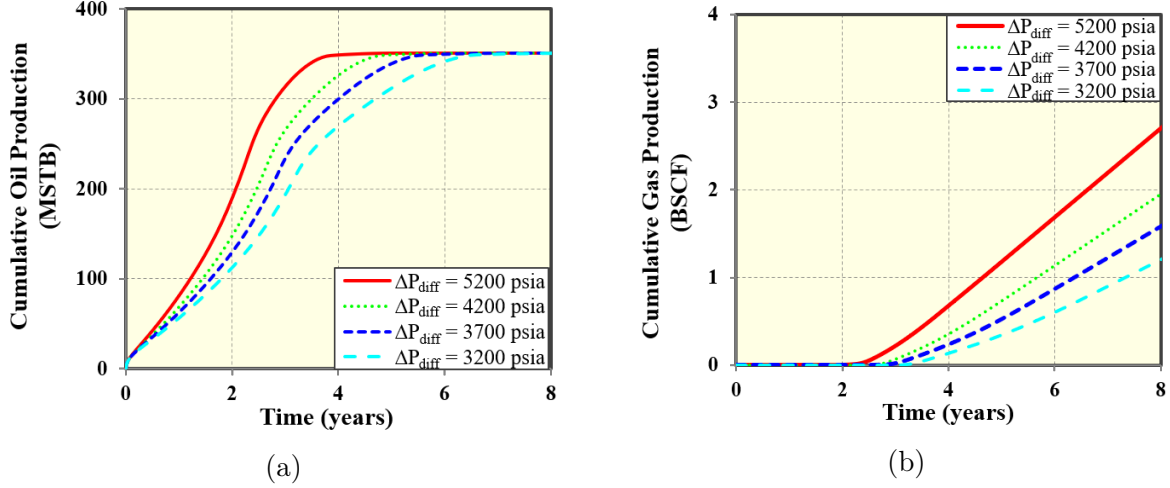


Figure 5.8. Performance plots show the role of the pressure difference between the injector and producer in the SDEOR technology. Figure (5.8a) and (5.8b) presents the plots of cumulative oil and gas production. Lower injection pressures corresponds to lower cumulative gas production, but the same cumulative oil produced compared to higher injection pressures.

### Effect of Injection Rate ( $q_{\text{inj}}$ ).

Second, we assess the role of  $\Delta P_{\text{diff}}$  in the SDEOR oil recovery by simulating a reservoir with different  $q_{\text{inj}}$  (100 scf/D, 10 Mscf/D, and 1 MMscf/D) producing at a constant  $P_{\text{wf}}$  of 1,000 psia for 30 years. We run the simulations longer to allow the injected gas to penetrate the low-permeability matrix and sweep the hydrocarbon between the top and bottom SD fractures. Under constant  $q_{\text{inj}}$ ,  $P_{\text{inj}}$  varies during the injection period, so we use Equation (5.1) to estimate an average  $P_{\text{inj}}$  value to calculate  $\Delta P_{\text{diff}}$ .

$$\bar{P}_{\text{inj}} = \frac{1}{t} \int_0^t P_{\text{inj}}(t) dt, \quad (5.1)$$

where  $\bar{P}_{\text{inj}}$  and  $t$  are the average injection pressure and total injection duration, respectively. Figure 5.9 is a performance plot for the SDEOR technology evaluated under different  $q_{\text{inj}}$  for 30 years and at a  $P_{\text{wf}}$  of 1,000 psia. For each injection rate case, we compute both  $\bar{P}_{\text{inj}}$  and  $\Delta P_{\text{diff}}$ . Results suggest that the  $\Delta P_{\text{diff}}$  controls how much cumulative oil can

be produced and the expected reservoir's production lifetime; for instance, injecting at 1 MMscf/D ( $\Delta P_{\text{diff}} = 5,668$  psia) results in an oil RF of 73.64% after approximately 2.5 years only as injected gas fully saturates the stimulated reservoir volume (SRV) between the two SD fractures. Depending on the formation injectivity, gas source availability, and surface pumping equipment, we prove that our technology can appreciably result in a long-term significant oil production increase even at the lowest  $\Delta P_{\text{diff}}$  values corresponding to a  $q_{\text{inj}}$  of 100 scf/D. SDEOR technology has the competitive edge of producing oil at an IOR ratio of 4.93 (approximately 493% more oil) while injecting at only 100 scf/D with  $\Delta P_{\text{diff}}$  of 353 psia, where the CGEOR methods require at least two orders of magnitude higher  $q_{\text{inj}}$  only to increase oil production by less than 10% (see Table 2.1). Although we show that higher injection rates result in higher oil RFs, the associated cumulative gas production ( $G_p$ ) drastically increases as in the case of 1 MMscf/D where  $G_p$  reaches 10 Bscf after 30 years, which is two orders of magnitude higher than cases with lower  $q_{\text{inj}}$ . Table 5.4 summarizes the results for oil recovery under different  $q_{\text{inj}}$  for the SDEOR technology.

Table 5.4. Results summary for the role of  $\Delta P_{\text{diff}}$  in oil recovery for SDEOR technology under constant injection rates and a  $P_{\text{wf}}$  of 1,000 psia after 30 years.

Injection Rate	$\bar{P}_{\text{inj}}$ (psia)	$\Delta P_{\text{diff}}$ (psia)	Oil RF (%)	Increased Oil RF (%)	IOR Ratio
100 scf/D	1,353	353	29.02	23.18	4.93
10 Mscf/D	1,691	691	43.9	38.06	7.43
1 MMscf/D	6,668	5,668	73.64	67.8	12.45

### Effect of Bottomhole Flowing Pressure ( $P_{\text{wf}}$ ).

Third, we assess the role of  $\Delta P_{\text{diff}}$  in SDEOR oil recovery by simulating a reservoir with varying  $P_{\text{wf}}$  (which may occur because of artificial lift methods) above and below the bubble point pressure ( $P_b$ ) while injecting at a constant rate of 10 Mscf/D for 30 years.

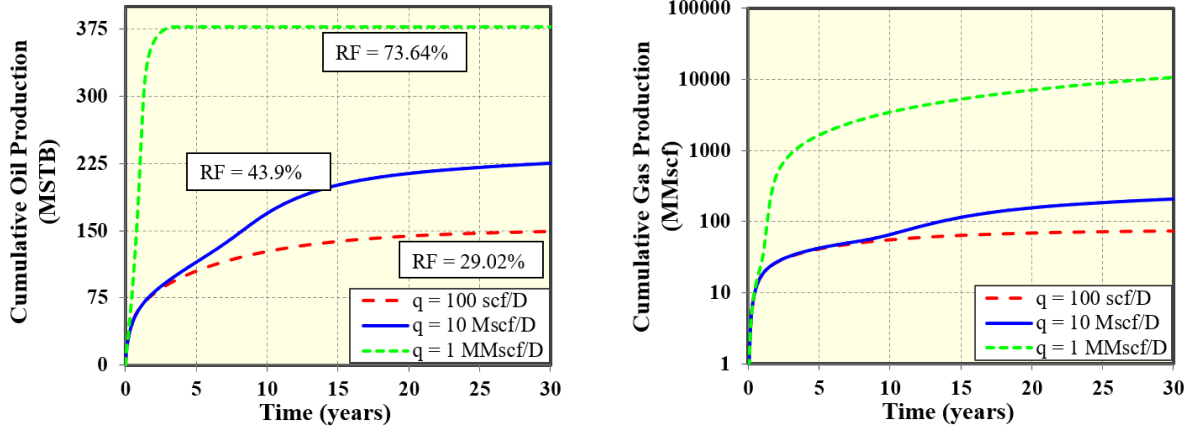


Figure 5.9. Performance plots for different injection rates showing the effect of  $\Delta P_{\text{diff}}$  on oil recovery while applying the SDEOR technology after 30 years at a constant  $P_{\text{wf}}$  of 1,000 psia. Increasing  $q_{\text{inj}}$  increases  $\Delta P_{\text{diff}}$ , and hence increases both oil and gas production. In the 1 MMscf/D case, oil production reaches a plateau shortly after 2.5 years as gas fully saturates the region between the top and bottom SD fractures.

The simulated fluid system has a  $P_b$  of 1,820 psia. Figure 5.10 shows performance plots corresponding to cases above and below  $P_b$ .

$P_{\text{wf}} > P_b$  : The application of the SDEOR technology, in this case, yields a constant oil production rate as cumulative oil production exhibits a linear relationship with time. The injected gas front is steadily developing, horizontally spreading, and is stabilized by means of gravity, as Figure 5.11a shows an image of  $C_1$  vapor mole fraction after 30 years when injected gas has not broken through into the bottom producer well, and  $G_p$  is zero throughout.

$P_{\text{wf}} < P_b$  : The application of the SDEOR technology in this case results in instantaneous gas production and  $G_p$  reaches 208 MMscf after 30 years. Figure 5.11b shows an image of  $C_1$  vapor mole fraction after 30 years, which exhibits a vortex-like distribution with an unstable gas front. Although associated gas production decreases the oil recovery efficiency, we prove that  $\Delta P_{\text{diff}}$  during the injection period controls how much oil SDEOR



can eventually recover, as we show next.

Table 5.5 summarizes the results for oil RF under the SDEOR application in cases where  $P_{wf}$  is above and below  $P_b$ . Again, oil RF is a function of  $\Delta P_{diff}$ , as previously demonstrated for cases with constant  $P_{inj}$  and  $q_{inj}$ . The slight difference between oil RFs after 30 years for cases below and above  $P_b$  (2.34%) is due to the corresponding  $\Delta P_{diff}$  of 691 and 430 psia, respectively. It is recommended that operators maintain  $P_{wf}$  above  $P_b$  to deter the cost associated with handling produced gas while recovering appreciable oil in the long run. If the economic assessment of the shale formation mandates short-term oil production, keeping  $P_{wf}$  below  $P_b$  shall boost oil recovery efficiency because of the higher  $\Delta P_{diff}$ .

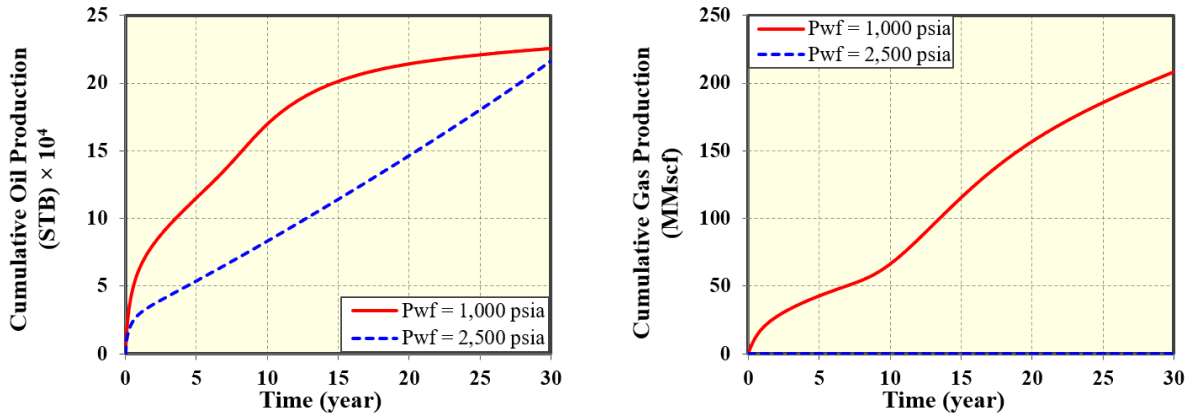


Figure 5.10. Performance plots for different  $P_{wf}$  (corresponding to cases below and above  $P_b$  as denoted by red and blue curves, respectively) with a constant  $q_{inj}$  of 10 Mscf/D for 30 years while implementing the SDEOR technology.

Table 5.5. Results summary for the SDEOR technology application for cases where  $P_{wf}$  is above and below  $P_b$  (1,820 psia) with a constant  $q_{inj}$  of 10 Mscf/D after 30 years.

$\bar{P}_{inj}$ (psia)	$P_{wf}$ (psia)	$\Delta P_{diff}$ (psia)	Oil RF (%)	Increased Oil RF (%)	IOR Ratio
2,930	2,500 ( $> P_b$ )	430	41.63	35.79	7.12
1,691	1,000 ( $< P_b$ )	691	43.97	38.13	7.47

Results from this subsection explain why our proposed SDEOR technology is ad-

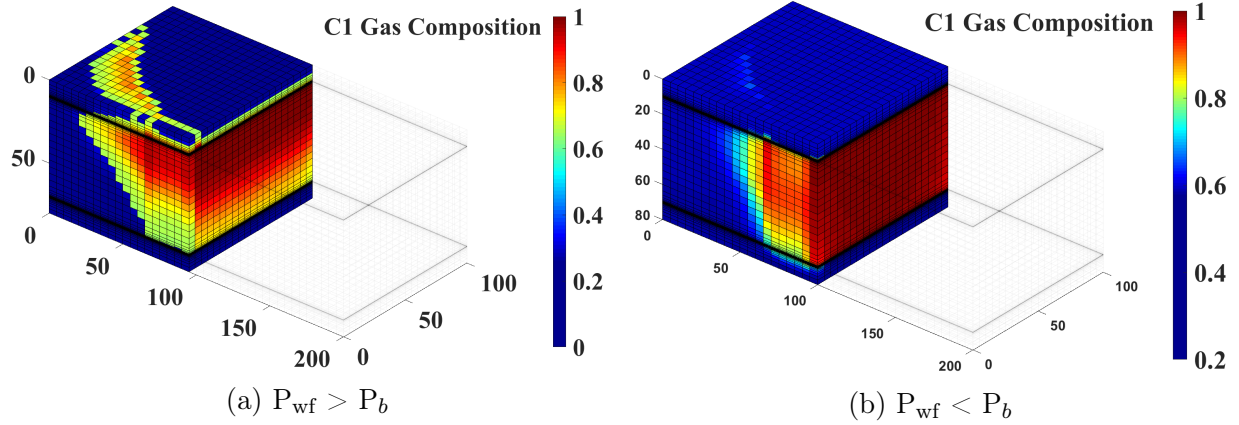


Figure 5.11. Images show  $C_1$  vapor mole fraction while simulating the SDEOR technology under a constant  $q_{inj}$  of 10 Mscf/D and different  $P_{wf}$  above and below  $P_b$ .  $\Delta P_{diff}$  during injection eventually controls how much oil is produced in both cases.

vantageous to CGEOR methods in shale plays. The discussed role of  $\Delta P_{diff}$  provides reservoir pressure maintenance 100% of the production duration. However, pressure support in CGEOR only occurs during the injection and soaking periods, representing at most 70% of the overall production period as presented in Section 5.2. Continuous injection mode in our SDEOR technology ensures that the bottom producer well is always pressure-supported, making our technology's performance unrivaled compared to CGEOR methods.

### 5.3.2. The Role of Gravity Drainage.

In this subsection, we investigate the role of gravity drainage as a mechanism in oil recovery for our proposed SDEOR technology. We evaluate the gravity-drainage effects on the SDEOR performance by simply turning it on or off in the reservoir simulator. Ignoring gravity in the simulations implies that the Darcy phase velocity expression in Equation (2.3) is modified as follows.

$$\bar{v}^\alpha = -\mathbf{K} \frac{k^\alpha(S)}{\mu^\alpha} \nabla p^\alpha \quad (5.2)$$

Equation (5.2) assumes that the injected light gas coexists with the heavier oil mixture without separation based on density differences, as gravity does not play a role.

Our simulation results show that gravity results have a higher contribution to oil production when matrix permeability increases and when reservoirs have dense networks of high-conductive natural fractures. Considering that shale-oil reservoirs are typically naturally fractured and are of low matrix permeabilities, we present the results for a shale reservoir with a matrix permeability of 50  $\mu\text{D}$  and 512 natural fractures (which is above the percolation threshold, as we showed in Section 4.1). The simulation results, given in Figure 5.12, show that gravity accounts for about 20% of the oil production after 30 years of simulated production. This effect could be even more significant if the simulation is run for a longer duration or if more and larger sub-vertical fractures are simulated as we show in Table 5.6. In Figure 5.13, we show the profiles for the mole fraction of methane gas ( $C_1$ ) after 30 years when gravity is turned on (left column images) and when it is turned off (right column images). Images after 15 and 30 years indicate that gravity helps stabilize the injected gas front and delays the breakthrough of the gas at the producer, as confirmed by the cumulative gas production presented in Figure 5.8b, and hence more oil recovery efficiency. These results indicate that the role of gravity in our proposed SDEOR technology could be the game-changer in shale plays like the Bakken, which are known to have low matrix permeabilities and a complex network of fractures. In such systems, the CGEOR method has not been successful, as discussed in Kuuskraa et al. (2020). This could be attributed to the predominantly horizontal flow expected during CGEOR through the sub-vertical fractures. However, in SDEOR and due to the vertical flow in the fractures, gravity appears to halt early gas production through the high-conductive

fractures by the buoyancy of the injected gas.

Again, simulation results suggest that the effect of gravity drainage on increasing oil recovery under the SDEOR technology increases in cases of (1) longer, (2) high-conductive, and (3) vertical NF planes. Additionally, and unlike the MSHF completion in CGEOR methods, our proposed SDEOR technology utilizes a gravity-drainage mechanism by mechanically creating horizontal SD fractures to control the flow direction of the injected gas downwards towards the bottom producer instead of preferentially flowing into high-conductive paths in the domain.

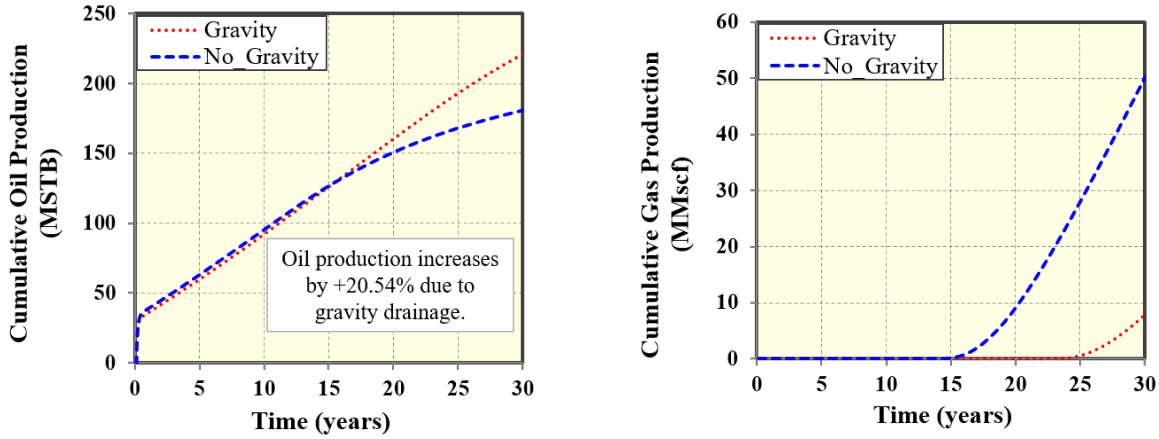
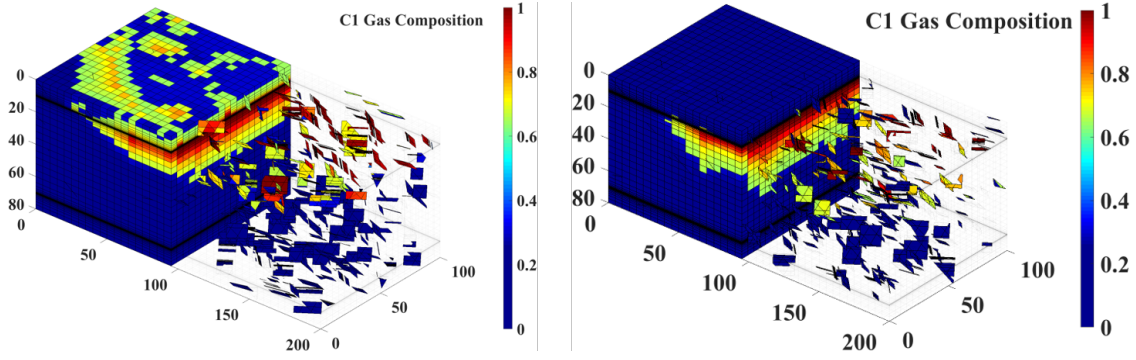


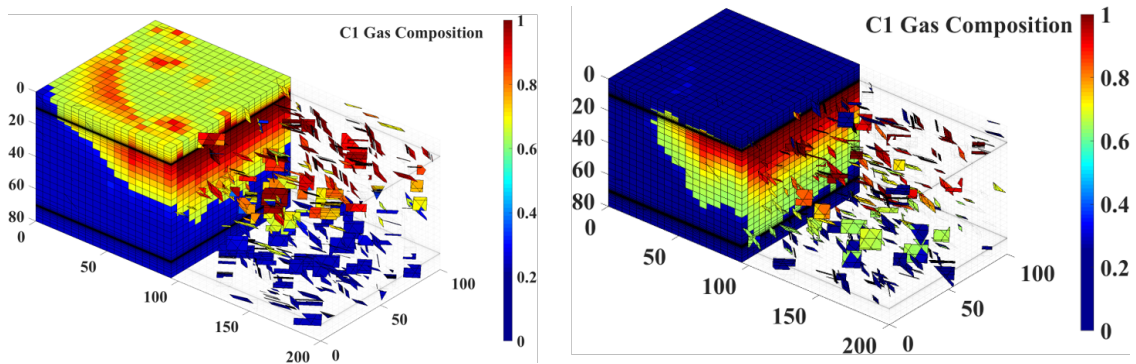
Figure 5.12. Performance plots for the cases with and without gravity demonstrates that gravity plays a significant role in the SDEOR technology. Gravity-drainage increases oil production by 20.54% after 30 years.

Table 5.6. Results summary for role of gravity-drainage in the SDEOR technology performance. In cases of high matrix permeabilities and nearly vertical fractures, gravity contributes more to oil recovery.

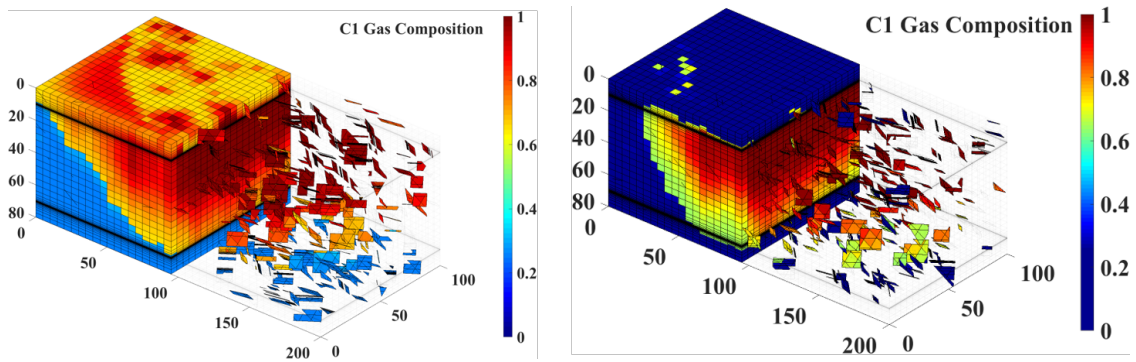
		<b>Matrix Permeability (<math>K_m</math>)</b>	
		<b><math>10\mu\text{D}</math></b>	<b><math>50\mu\text{D}</math></b>
<b>NF Orientation</b>	<b>Sub-Horizontal</b>	+4.27%	+20.64%
	<b>Sub-Vertical</b>	+5.28%	+22.47%



(a) 8 years



(b) 15 years



(c) 30 years

Figure 5.13. Left and Right images show the profile of methane gas mole fraction with and without gravity, respectively. Gravity tends to stabilize the injected gas front and delays gas breakthrough, compared to the cases without gravity where injected gas coexists with the reservoir fluid without phase segregation and undergoes an early breakthrough.

### 5.3.3. The Role of Molecular Diffusion.

In this subsection, we investigate the role of molecular diffusion as a recovery mechanism for SDEOR technology. We use the dusty-gas model in Equation (2.37) to compute the diffusion flux in both gas and oil phases. Although diffusion results for the base case parameters given in Table 4.1 do not show hydrocarbon production increase, we model diffusion for the same reservoir system, but with a 1 nD matrix permeability, a 100 scf/D constant  $q_{inj}$ , and a high-resolution mesh along the Z direction (grid dimensions are  $40 \times 20 \times 125$ ) to exaggerate the diffusion effect. Figure 5.14 shows the performance plots after 30 years and suggests that cumulative oil and gas production increases by 3.46% and 3.54%, respectively. This slight percentage increase in both gas and oil cumulative production indicates that molecular diffusion is not the main recovery mechanism for the SDEOR technology, and the hydrocarbon recovery process is pressure-dominated, as demonstrated in Subsection 5.3.1. However, and in the CGEOR methods, molecular diffusion is considered the main recovery mechanism during the soaking period where the injected gas diffuses into the fractured matrix system and does have a positive net effect on the hydrocarbon recovery (Yu et al., 2015; Zhang et al., 2018).

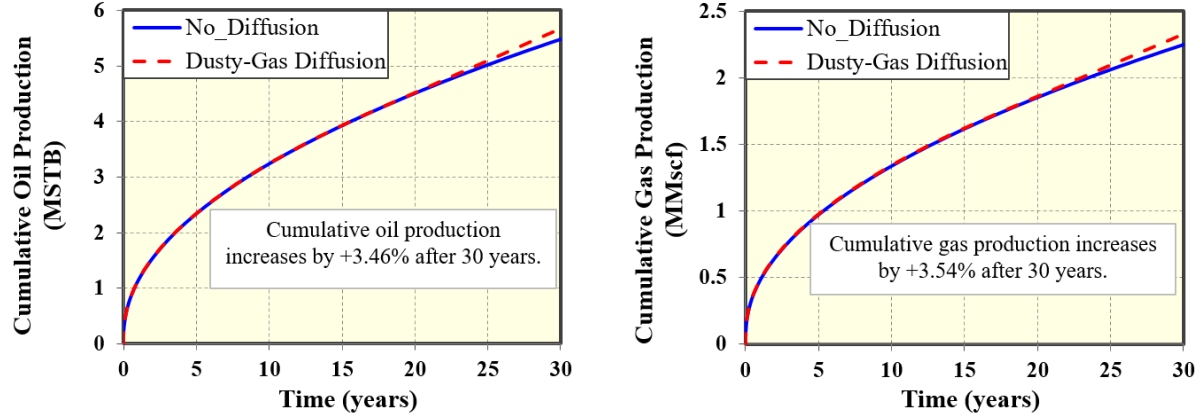


Figure 5.14. Performance plots show the cumulative oil (Left) and gas (Right) production under the effect of molecular diffusion (modeled using Equation (2.37)). Results show that considering the dusty-gas diffusion only increases cumulative production by 3.46% and 3.54% for oil and gas, respectively, after 30 years when applied to the SDEOR technology in shale formations.

#### 5.3.4. The Role of Oil Viscosity Reduction

In this subsection, we study the role of oil viscosity reduction as a recovery mechanism for our proposed SDEOR technology. During the continuous gas injection into the top injector, gas intermixes with oil in the reservoir, and the oil phase viscosity decreases. Again, we simulate our SDEOR technology by injecting at a constant  $q_{inj}$  of 10 Mscf/D with a  $P_{wf}$  of 1,000 psia for 30 years. We compute the surface oil phase viscosity using the Lohrenz-Bray-Clark (LBC) compositional viscosity model (Lohrenz et al., 1964), as we show in Figure 5.15. The surface produced oil viscosity reduces initially from 0.017 cp to 0.0139 cp (-18.23% change) after 30 years. We also show that the in-situ oil phase viscosity decreases during the gas injection, as images in Figure 5.16 show. This is because oil phase mobility ( $\frac{K_o}{\mu_o}$ ) increases as its viscosity decreases, and it easily flows towards the bottom producer. We notice a slight decrease in oil viscosity because we simulate a low-



viscosity simple fluid mixture as the commercial shale oil plays are usually volatile oils. Higher viscosity mixtures, however, undergo significant oil phase viscosity reductions at one or two orders of magnitude when mixed with miscible gas injection during HnP or continuous gas methods (Hao et al., 2020; Zou et al., 2017).

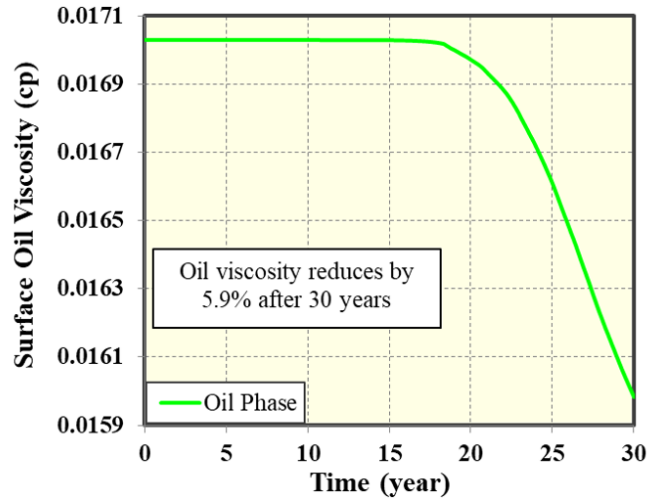


Figure 5.15. A plot shows the surface oil viscosity after 30 years while applying the SDEOR technology application. As injected gas intermixes with reservoir oil, its viscosity decreases as depicted by the figure.

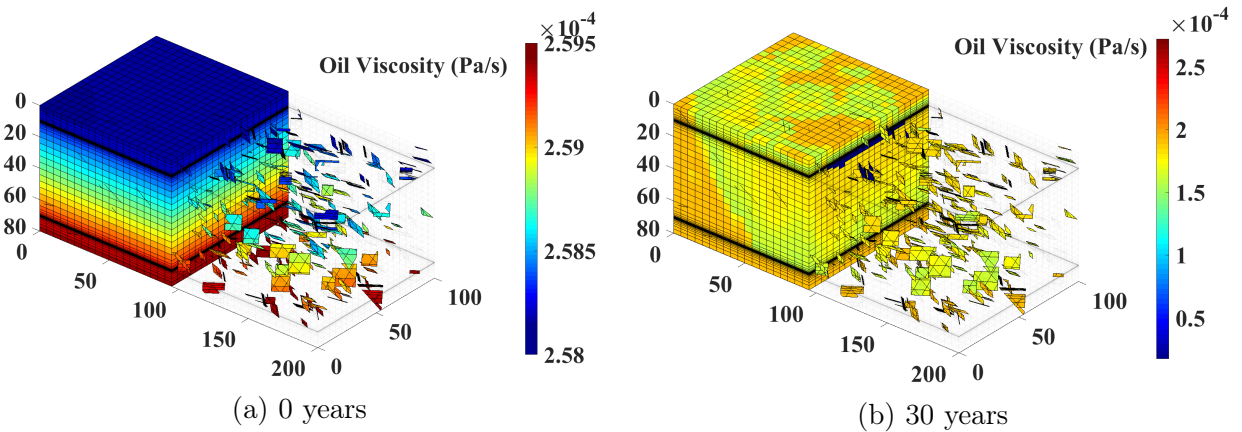


Figure 5.16. Images show in-situ oil phase viscosity at the beginning (left) and after 30 years (right) of simulating our SDEOR technology while constantly injecting at a  $q_{inj}$  of 10 Mscf/D and producing at  $P_{wf}$  of 1,000 psia. In-situ oil viscosity decreases as injected gas continuously mixes with residual oil in the reservoir.

#### 5.4. Simulation Results for the SDEOR Technology Application in Heterogeneous Shale Formations.

In this subsection, we assess the performance of our proposed SDEOR technology against matrix heterogeneity expected in our target shale formations. We study heterogeneity effects for both the matrix porosity and the matrix permeability. First, we sample matrix porosity values from a Gaussian distribution ranging from 6% to 10% with a mean value of 8% and a standard deviation of 1.5%. Figure 5.17 shows an image of the porosity distribution at each grid block in the domain. Second, and to generate a representative

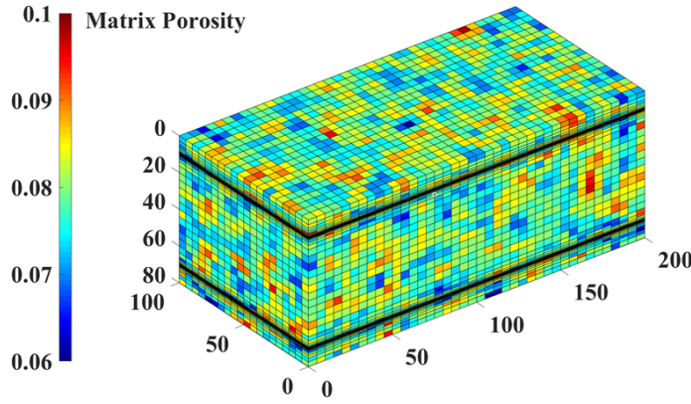


Figure 5.17. An image shows the Gaussian distribution of matrix porosity in a  $200 \times 100 \times 80$  m simulation domain. Matrix porosity ranges between 6% and 10%.

matrix permeability distribution, we start by computing permeability as a function of the sampled porosity using the Carman-Kozeny (CK) relation, and next, we independently sample permeability from a log-normal distribution.

Equation (5.3) computes Carman-Kozeny permeability as a function of porosity, grain size, and tortuosity.

$$K = \frac{1}{72\tau} \frac{\phi^3 d_p^2}{(1 - \phi)^2}, \quad (5.3)$$

where  $\tau$  is the tortuosity, and  $d_p$  is the average particle diameter, which we assume equal to 1 micron for clay-type grain size expected in low-permeability shale formations (Kowal-

ski, 2010). Figure 5.18a shows the permeability distribution computed using Equation (5.3), while Figure 5.19a shows an image of the grid block permeability in the simulation domain. The mean permeability value is  $10.7 \mu\text{D}$  with a standard deviation of  $1.72 \mu\text{D}$ . We independently sample matrix permeability for each grid block using a log-normal distribution with the following probability density function (pdf) expression.

$$f(x) = \frac{1}{\sqrt{2\pi}\sigma x} \exp \left[ -\frac{\ln(x - \mu)^2}{2\sigma^2} \right], \quad (5.4)$$

where  $\mu$  and  $\sigma$  are the mean and standard deviation, respectively. Figure 5.18b shows the permeability distribution calculated using Equation (5.4), while Figure 5.19b shows an image of the grid block permeability in the simulation domain. The mean permeability value is  $10.24 \mu\text{D}$  with a standard deviation of  $4.93 \mu\text{D}$ .

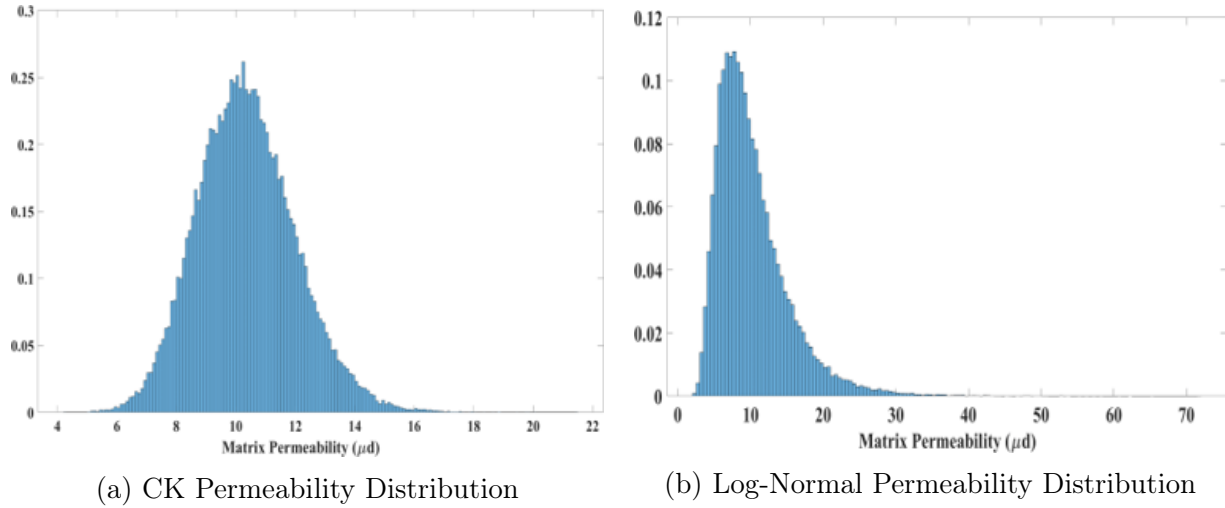


Figure 5.18. Plots of matrix permeability distributions using (5.18a) Carman-Kozeny relation and (5.18b) using log-normal distribution. Both approaches are used to generate a heterogeneous permeability distribution for the grid blocks in the simulation domain.

We simulate our SDEOR technology for 30 years using a constant  $q_{\text{inj}}$  of  $10 \text{ Mscf/D}$  and a  $P_{\text{wf}}$  of  $2,500 \text{ psia}$  for a base case of homogenous matrix permeability of  $10 \mu\text{D}$ , and two heterogeneous matrix permeability cases corresponding to CK relation and the log-

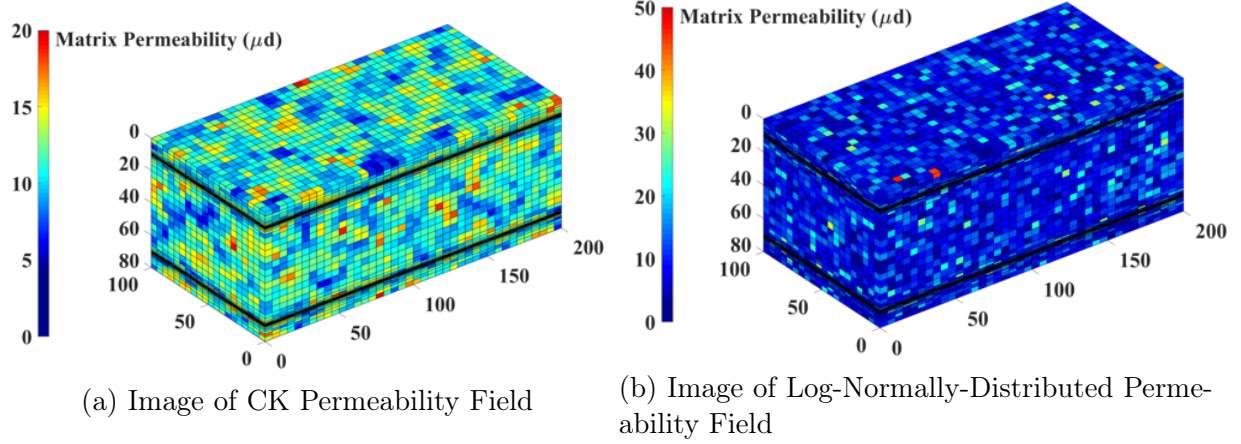


Figure 5.19. Images of matrix permeability distribution in the grid blocks for simulation domain dimensions of  $200 \times 100 \times 80$  m using (5.19a) CK relation and (5.19b) log-normal distribution.

normal distribution. We show the performance plots in Figure 5.20. Results suggest the robustness of our SDEOR technology application for heterogeneous shale formations as the cumulative oil production profile is the same for the homogenous case and the two other heterogeneous cases up to 20 years of operation. The change in cumulative oil production slopes corresponds to when the injected gas breaks through into the bottom producer. CK heterogeneous case (solid red line) has the highest oil recovery after 30 years because the permeability distribution has the highest mean value of  $10.71 \mu\text{D}$ , compared to other cases. The gravity-drainage mechanism becomes more efficient matrix permeability increases, as we demonstrated in Subsection 5.3.2. So, CK heterogeneous case has the highest oil recovery as gravity stabilizes the injected gas front and delays its breakthrough, compared to other cases.

Results from this subsection suggest that our SDEOR technology is advantageous to CGEOR methods when applied to heterogeneous shale formation. The latter shows a faster decrease in the rate of oil recovery factor (Chen et al., 2014), whereas our SDEOR

technology has a constant rate of oil recovery (i.e., a straight-line cumulative oil production line), as we show in Figure 5.20.

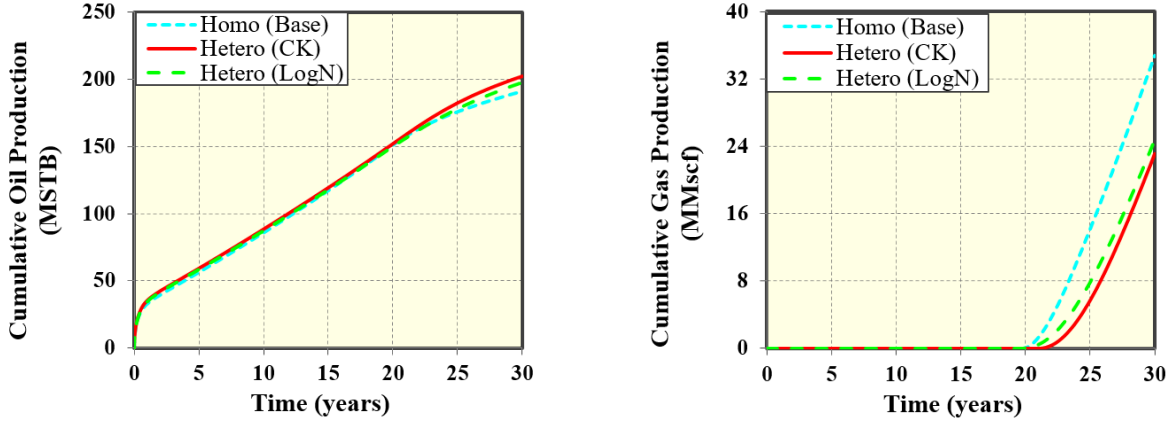


Figure 5.20. Performance plots show a comparison of the cumulative oil (Left) and gas (Right) production from a homogenous base case, and two heterogenous permeability distribution cases using CK relation and the log-normal distribution. The results show the robustness of our SDEOR technology application in heterogeneous shale formations as cumulative oil production profile is the same for the 3 cases up to 20 years of production.

### 5.5. Effect of the SD Fracture Conductivity on the SDEOR Technology Performance.

In this subsection, we study the effect of SD fracture conductivity on the performance of our proposed SDEOR technology. Under a normal stress state, vertical stress ( $\sigma_v$ ) is the maximum principle stress (Zoback, 2010). So, the horizontal SD fracture conductivity may decrease over time because of  $\sigma_v$  that may lead to proppant embedment or SD fracture closure. Figure 5.21 shows performance plots for different SD fracture conductivity cases. We next calculate the dimensionless fracture conductivity ( $F_{CD}$ ) for SD fractures using the following equation.

$$F_{CD} = \frac{K_{SD}w_{SD}}{K_m X_{SD}}, \quad (5.5)$$

Where  $K_{SD}$ ,  $w_{SD}$ , and  $X_{SD}$  are the permeability, width, and half-length for the SD fracture, respectively.  $K_m$  is the matrix permeability. Table 5.7 gives  $F_{CD}$  values corresponding to each SD fracture conductivity case.  $F_{CD}$  values above 50 correspond to SD fractures with infinite conductivity, where there is not a pressure drop inside the fracture and the flow is linear (Wattenbarger et al., 1998).

Results from this subsection suggest that our SDEOR performance is robust as long as the SD fracture has infinite conductivity. However, SDEOR oil recovery efficiency deteriorates as SD fractures become finite-conductive, corresponding to a two-order magnitude reduction of our base case SD fracture conductivity as we showed in Figure 5.21.

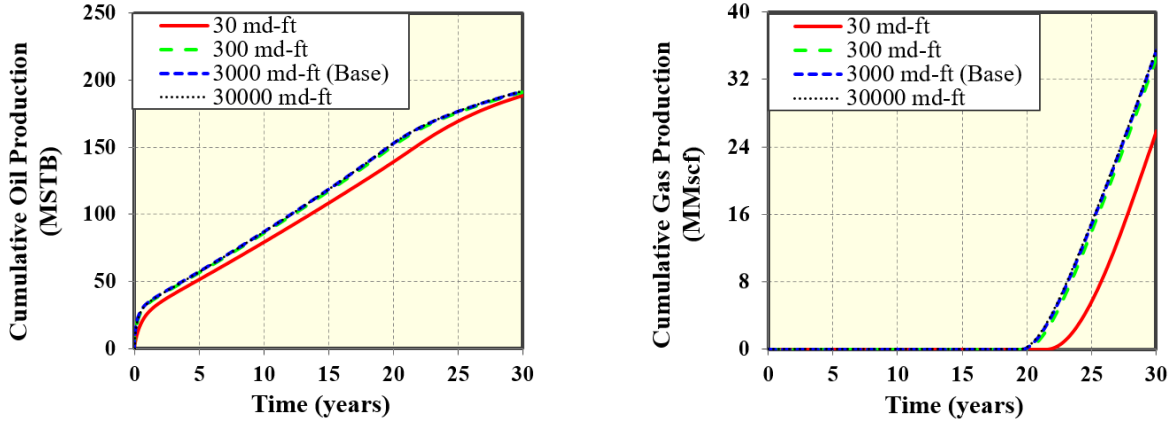


Figure 5.21. Performance plots show a comparison of the cumulative oil (Left) and gas (Right) production for different SD conductivity cases. Results show that SDEOR performance is robust as long as SD fractures are infinite-conductive.

Table 5.7.  $F_{CD}$  corresponding to different SD fracture conductivities.

SD Fracture Conductivity (md-ft)	$F_{CD}$	Conductivity Type
30	9	Finite ( $F_{CD} < 50$ )
300	92	Infinite
3000 (base case)	915	Infinite
30000	9146	Infinite

## 5.6. Waterflooding Application to Fractured Shale Formations using the SDEOR Technology.

In this subsection, we extend the applicability of our SDEOR technology completion to shale formations and show its adaptability to different operation configurations. We showed previously in Figure 1.3 that the top well is used for gas injection while the bottom well is for oil production. Here, we use the bottom well for water injection and the top well for oil production. We simulate waterflooding into the bottom well by injecting at a constant  $q_{inj}$  of 0.1 bbl/D because of the low formation injectivity. Figure 5.22 shows the performance plots of the waterflooding application after 30 years. Oil RF only increases by 4.19% after 30 years, and cumulative oil production flattens after only two years. The slight increase in oil production occurs because injected water only saturates a region half a meter above the SD fracture area (as shown in the zoomed image in Figure 5.23b) with limited penetration capability into the matrix and fracture, as shown in the image of Figure 5.23a.

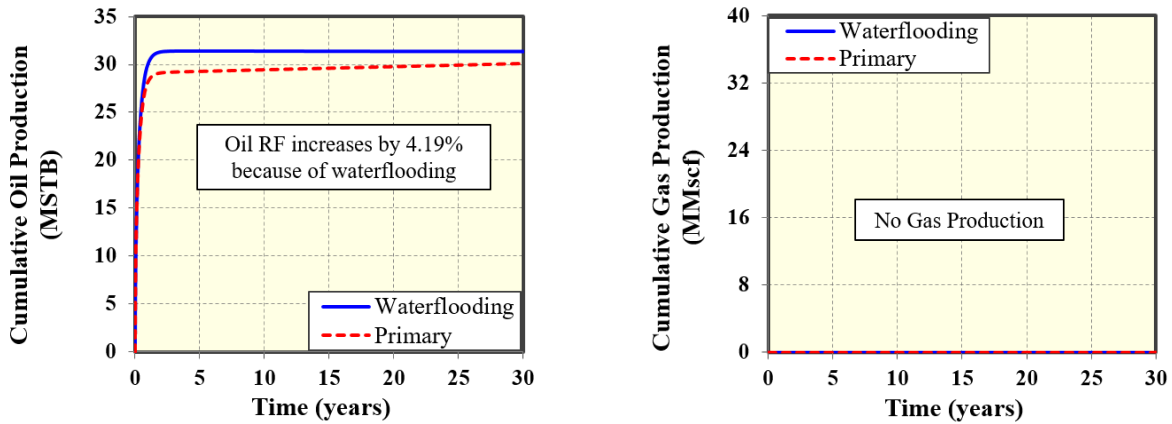
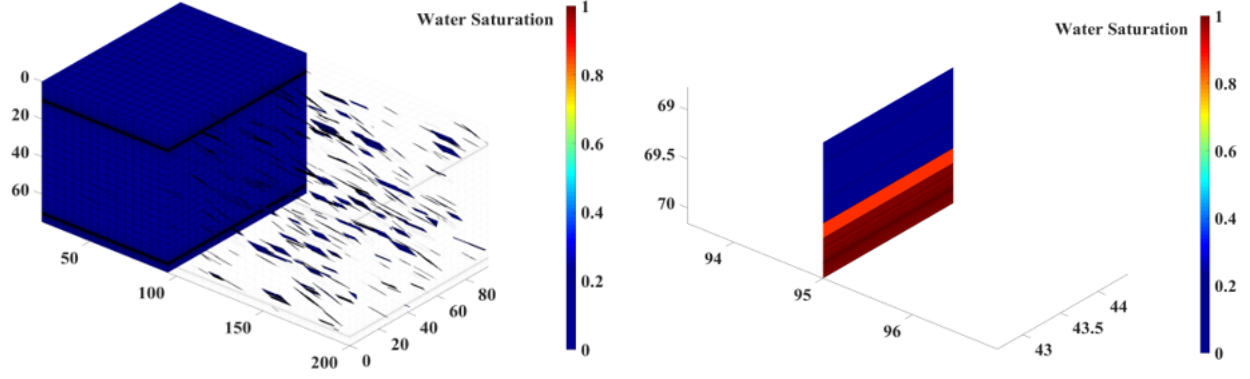


Figure 5.22. Performance plots show the cumulative oil (Left) and gas (Right) production for waterflooding application using the SD technology. The results only show 4.19% oil recovery increase after 30 years because of the low formation injectivity.





(a) An image of water saturation map after 30 years

(b) A zoomed image of water saturation map after 30 years above SD fracture

Figure 5.23. Images of water saturation maps after 30 years. Left image (5.23a) shows the limited penetration capability of water into the matrix and natural fractures. Right image (5.23b) is a zoomed vertical cross-section that shows water only flows a half meter above the SD fracture (located at 70 meters).

Although waterflooding does not yield higher oil RF when applied to our base case, results from this subsection show the application robustness of our SDEOR technology depending on the densities of the injected and produced fluids. If the injection fluid has a higher density than the reservoir fluid, the bottom well shall be completed as an injector well, and the top well as a producer, and vice versa.

## 5.7. SDEOR Application to Shale Formations

In this section, we numerically evaluate the application of SDEOR in comparison to CGEOR in actual shale plays. To ensure that the CGEOR cases simulated are not under-performing by sub-optimal operating conditions (in comparison to SDEOR), we will simulate the cyclic injection of methane gas under efficient operating conditions as follows:

1. Use optimum field injection, soaking, and production durations of 60, 14, and 180 days (2, 0.5, and 6 months), respectively (Kuuskraa et al., 2020).
2. Operate at  $P_{wf}$  above  $P_b$  to prevent the vaporization of the oil and ensure optimum



CGEOR recovery factor (Sun et al., 2019).

3. Start CGEOR after the cumulative oil production from primary recovery flattens out.

Next, we present the results from the simulation of two shale formations: (1) the Eagle Ford and (2) Bakken shale formations. In both cases, we simulate primary production for three years, after which we simulate both CGEOR and SDEOR for eight additional years.

**Eagle Ford Shale:** To model a volatile oil Eagle Ford shale reservoir, we use the fluid composition data presented in Tables A.5 and A.6. Most of the reservoir input parameters used are given in Table 4.1, but to model a representative Eagle Ford shale reservoir, we use  $P_i$ ,  $P_{wf}$ , and  $q_{inj}$  values of 7,000 psia, 2,500 (above  $P_b = 1,560$  psia), and 100 Mscf/D, respectively. Figure 5.24 is the 2-phase envelope for Eagle Ford shale volatile oil. Additionally, we do not simulate NFs in Eagle Ford because Raterman et al. (2018) analyzed whole cores retrieved from producing Eagle Ford wells and confirmed the scarcity of natural fractures in the field from the SRV in the stimulated region around the multilateral shale wells. Figure 5.25 compares the performance of our SDEOR technology against CGEOR and shows that SDEOR produces 3.8 times more oil than CGEOR after 11 years only. The slope change of the SDEOR cumulative oil production (dotted blue line) corresponds to when the injected gas breaks through into the bottom producer after six years (which is confirmed in the right plot in Figure 5.25). This observation indicates that the production of associated gas is typically negligible while most of the oil is being recovered during SDEOR, which will minimize the costs associated with gas handling in the surface facilities. As explained in Section 5.3.2, the reduction in gas production until gas breaks

through is because of the role of gravity in stabilizing the gas front in SDEOR from fractured reservoirs.

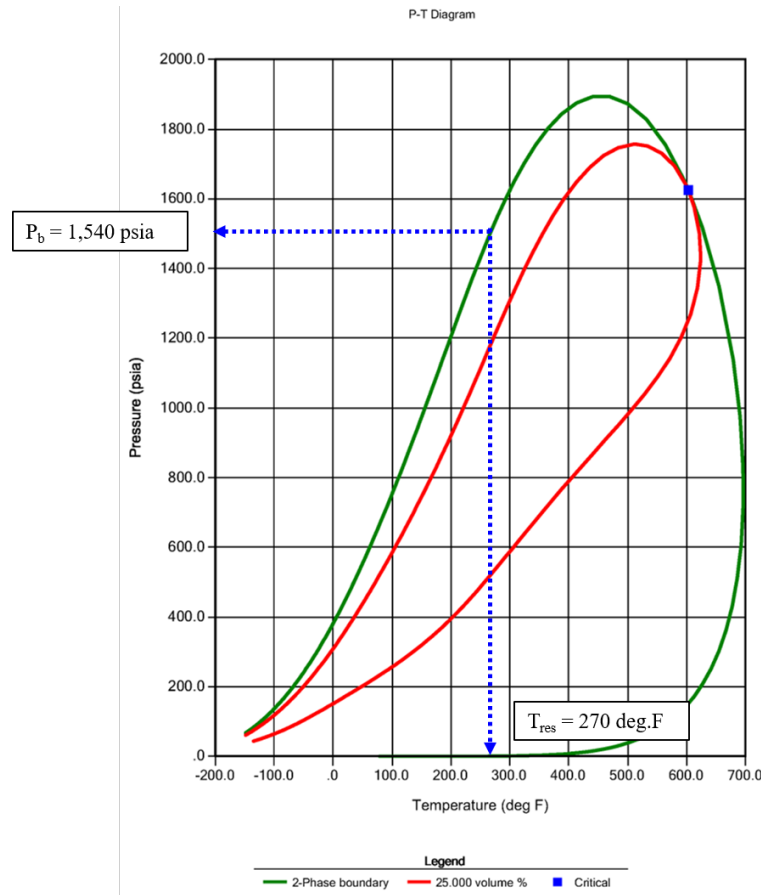


Figure 5.24. 2-phase envelope for Eagle Ford volatile oil shale (generated using CMG-WinProp 2018.1).

This drastic increase in oil recovery from SDEOR compared to CGEOR even in shale reservoirs with little or no fractures shows the applicability in such shale plays. In the next case, we present SDEOR simulation results for the Bakken shale (which has lots of complex natural fractures), where CGEOR methods have not successfully increased the recovery.

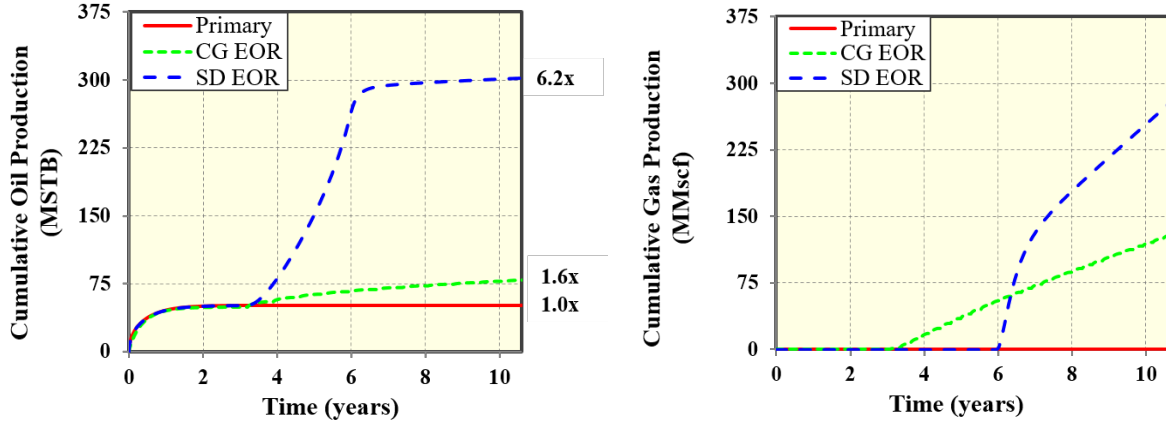


Figure 5.25. Performance plots show a comparison of the cumulative oil (Left) and gas (Right) production from primary production, CGEOR, and SDEOR from a representative Eagle Ford shale oil well. The results show that SDEOR yields more than 3.8 times more oil than CGEOR.

**Bakken Shale:** To model a volatile oil Bakken shale reservoir, we use the fluid composition data presented in Tables A.7 and A.8. Most of the reservoir input parameters used are given in Table 4.1, but to model a representative Bakken shale reservoir, we use  $P_i$ ,  $P_{wf}$ , and  $q_{inj}$  values of 6,700 psia, 3,000 (above  $P_b = 1,640$  psia), and 30 Mscf/D, respectively. Figure 5.27 is the 2-phase envelope for Bakken shale volatile oil. We simulate 150 sub-vertical natural fracture planes with 1.5 md-ft conductivity, dip ranging from  $60^\circ$  to  $90^\circ$  (with a mean of  $80^\circ$ ), and dip direction between  $N50^\circ W$  and  $S40^\circ E$ , as interpreted from the formation micro-imager (FMI) logs (Sturm and Gomez, 2009) (as shown in Figure 5.26). Figure 5.28 compares the performance of our SDEOR technology against CGEOR and shows that SDEOR produces 3.2 times more oil than CGEOR after 11 years only. CGEOR yields in cumulative gas production of 15.2 MMscf, whereas our SDEOR technology does not yield any gas production after 11 years because the injected gas has not yet broken through the bottom producer. This result ensures the flexibility in de-

signing the SDEOR technology to optimize the duration of oil production before the gas breakthrough by modifying the injection rates or pressures based on the permeability and thickness of the shale formation.

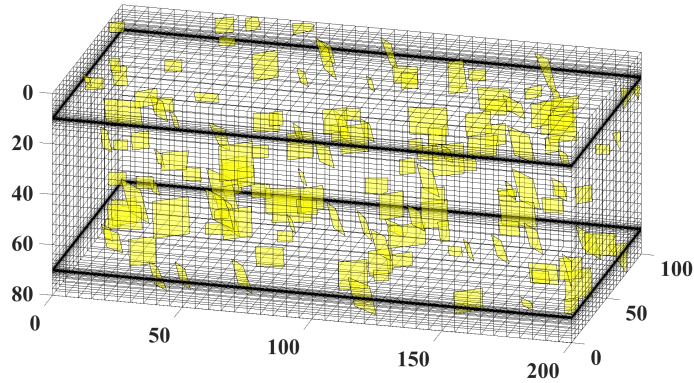


Figure 5.26. An image for 150 NFs having the same dip ( $60^\circ \sim 90^\circ$ ) and dip direction ( $S40^\circ E$  to  $N50^\circ W$ ) ranges as Bakken shale formation (Sturm and Gomez, 2009).

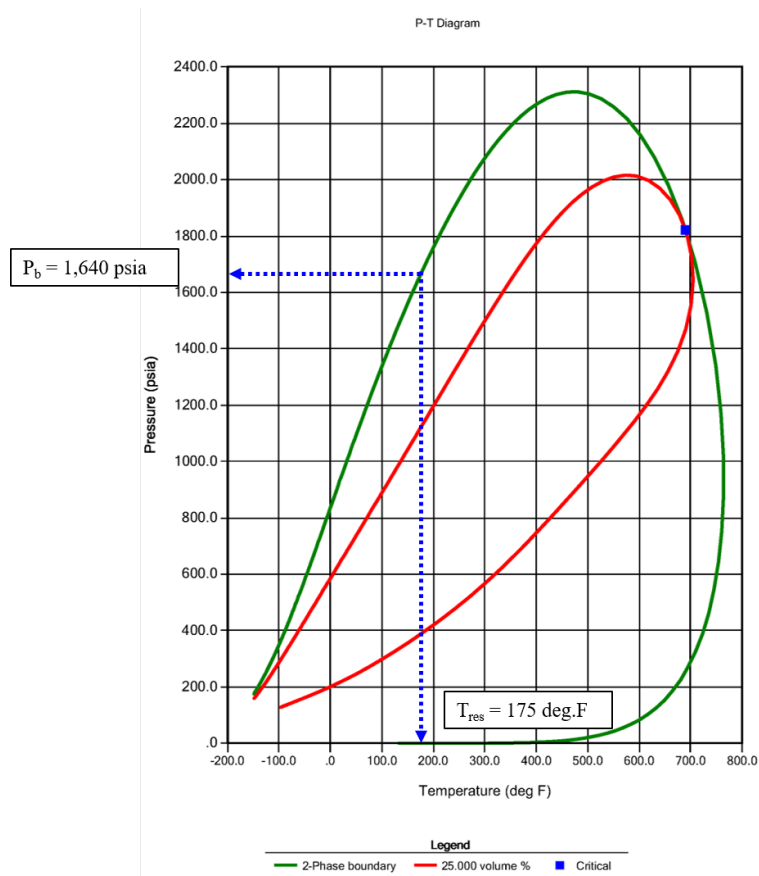


Figure 5.27. 2-phase envelope for Bakken volatile oil shale (generated using CMG-WinProp 2018.1).

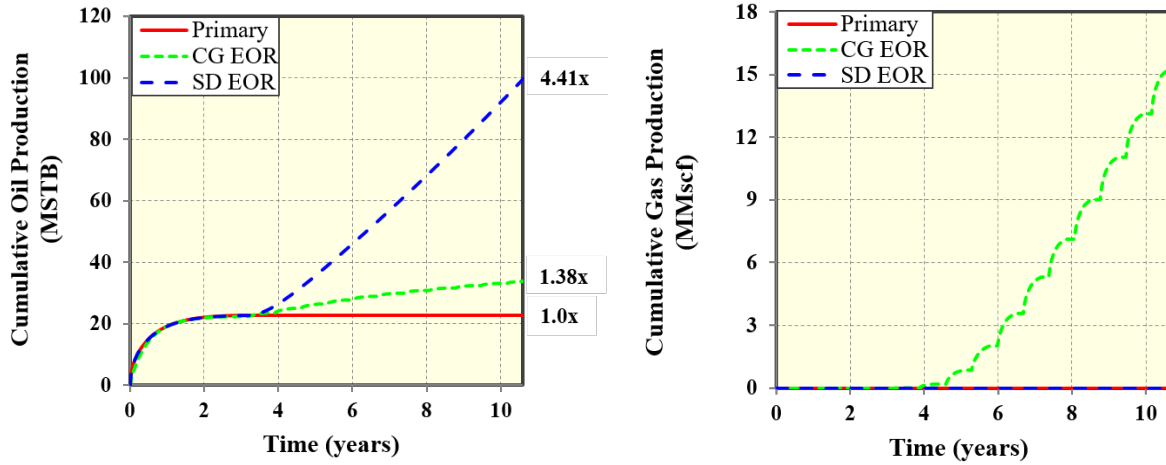


Figure 5.28. Performance plots show a comparison of the cumulative oil (Left) and gas (Right) production from primary production, CGEOR, and SDEOR from a representative Bakken shale oil well. The results show that SDEOR yields more than 3.2 times more oil than CGEOR.

Table 5.8 summarizes the results of the simulated recoveries from both the Eagle Ford and Bakken shale plays using SDEOR and CGEOR. The IOR ratios for the CGEOR method lies within the published range for the Eagle Ford (1.34 – 1.62) and Bakken (1.11 – 1.41) shale plays (Kuuskraa et al., 2020). The consistent superiority of our SDEOR technology in producing at least three times more oil than CGEOR proves that it is a game-changer technology in recovering oil from shale-oil formations.

Table 5.8. Incremental oil recovery in shale formations from our SDEOR technology and CGEOR.

Shale Formation	Recovery Mechanism	Oil RF (%)	EUR (Mstb)	IOR Ratio
Eagle Ford Shale	Primary	10.7	49.2	N/A
	CGEOR	17.1	77.9	1.6
	SDEOR	66.0	302.8	6.2
Bakken Shale	Primary	5.0	24.1	N/A
	CGEOR	6.8	33.2	1.38
	SDEOR	21.8	106.2	4.41

In the next two subsections, we extend the results for our SDEOR technology to Bakken shale because CGEOR field pilots have reported being unsuccessful and operationally challenging as injected gas quickly dispersed into the natural fractures without achieving a high-pressure soaking period for a substantial oil production increase. The goal is to study the performance of the SDEOR technology in Bakken shale-oil reservoirs while injecting at a constant  $q_{inj}$  of 10 Mscf/D for 30 years under the following unfavorable EOR conditions (Pospisil et al., 2020):

1. The presence of natural fracture networks at low and high conductivities.
2. Operating at  $P_{wf}$  (1,000 psia) below both  $P_b$  (1,640 psia) and the minimum miscibility pressure (MMP) for different solvents used (such as  $CH_4$ ,  $N_2$ , Flue Gas, and  $CO_2$ ).

#### **5.7.1. Study of SDEOR performance in Bakken shales with different fracture conductivities**

Again, we simulate production from the Bakken shale for 30 years under both primary recovery and the SDEOR technology using compositional data inputs given in Table A.7 and Table A.8. The SDEOR cases studied include a base case without natural fractures, one with 1024 conductive natural fractures and another with 1024 non-conductive (NC) natural fractures. We select the 1024 NFs network realization to get meaningful results as connectivity exceeds the percolation threshold, as illustrated in Section 4.1. Figure 5.29 shows performance plots for these cases compared to primary recovery after 30 years. Implementing our proposed SDEOR technology to Bakken formation increases oil production by at least five times with a +29.45% increase in oil RF, which proves the unrivaled performance compared to CGEOR results reported in the literature and as we showed in the performance comparison in Table 2.1 and Table 5.8, respectively.

Figure 5.30 shows  $C_1$  gas composition profiles for the SDEOR cases in Bakken formation without NFs, with 1024 conductive NFs, and with 1024 non-conductive NFs. Adding stochastic fracture networks slightly decreases the sweeping efficiency as injected gas flows through paths of least resistance, causing gas fingering, upward migration to the reservoir's top portions, and distortion to the stable gas front initially established for the base case in Figure 5.30a. Nonetheless, we still get a substantial increase in oil RF and produce four times more oil while applying the SDEOR technology to Bakken shale with high and low conductive NF networks. These results confirm the applicability of this technology in unfractured shale-oil reservoirs like the Eagle Ford shale play (Rateman et al., 2018) and in densely fractured reservoirs like the Bakken shale play (Kuuskraa et al., 2020).

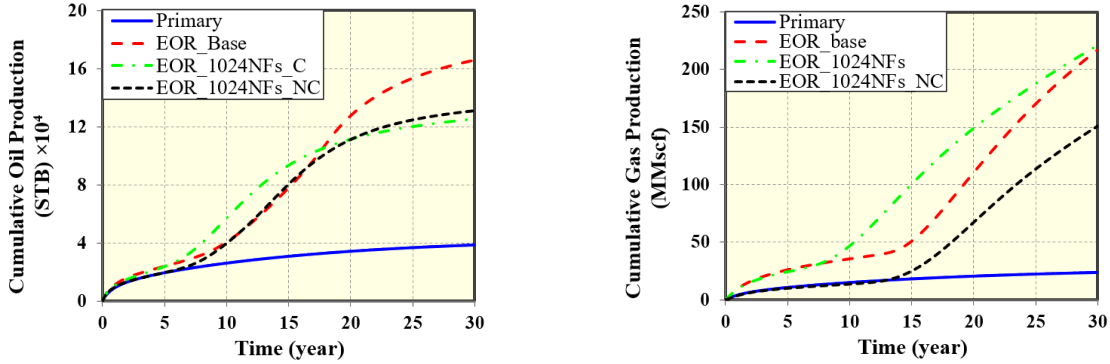


Figure 5.29. Performance plots after 30 years for SDEOR technology application to fractured Bakken shale. Results indicate the robustness of our proposed technology as it produces at least four times more oil than primary recovery regardless of the number of sealing or conductive fractures in the reservoir.

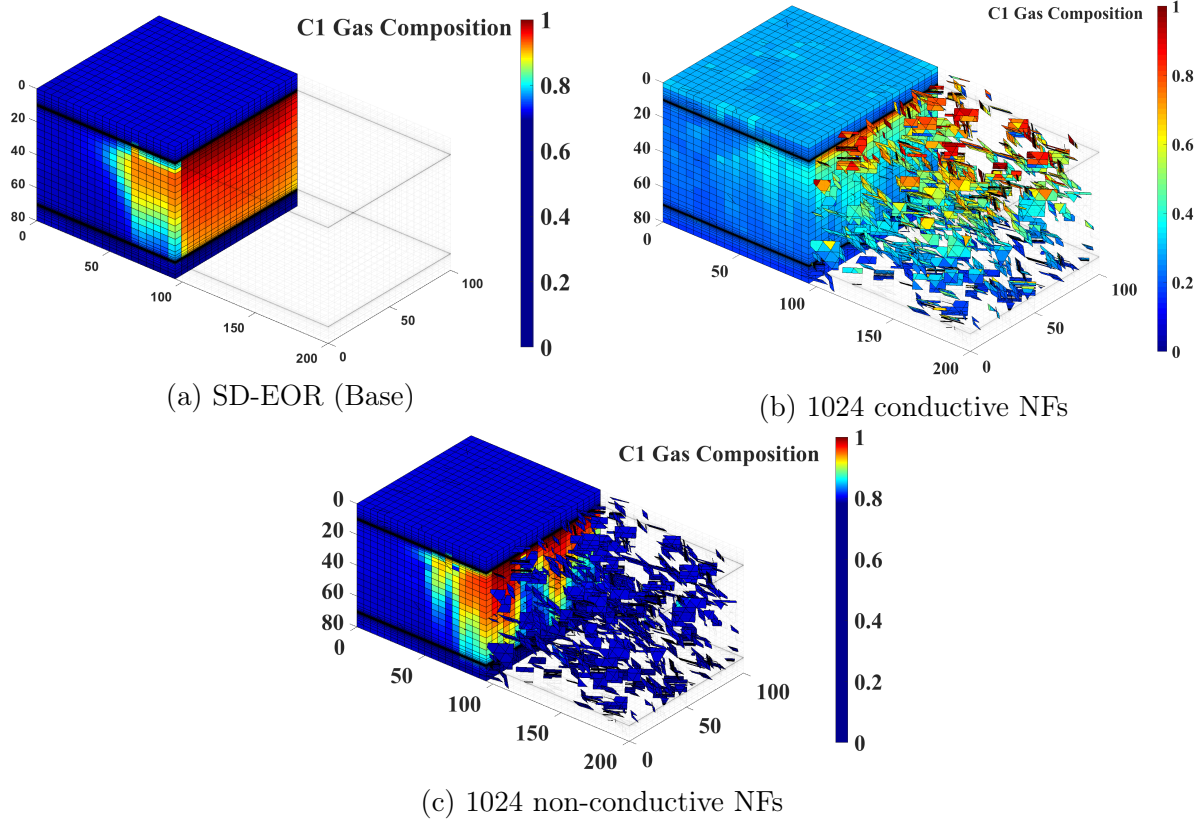


Figure 5.30.  $C_1$  gas composition maps after 30 years when the SDEOR applies to the Bakken shale for (5.30a) a base case without NFs, (5.30b) with 1024 conductive NFs and (5.30c) with 1024 non-conductive NFs. Adding NFs beyond the percolation threshold distorts the developed stable gas front during injection, and slightly reduces the overall injected gas sweeping efficiency.

### 5.7.2. Study of SDEOR performance in Bakken shales with different solvents

In this subsection, we apply our SDEOR technology to Bakken shale under different solvent injection methods, such as  $CH_4$ ,  $N_2$ , flue gas, and  $CO_2$ . Figure 5.31 shows a comparison of the cumulative oil (Left) and gas (Right) production when these different gases are injected, while Table 5.9 summarizes these results and provides the molecular weight of each of the injected gases. The dotted lines in the figure correspond to the results when gravity is turned off, while the solid lines of the same color are the results for the corresponding case with gravity turned on. The difference between the cases with and



without gravity is more significant for the lighter gases (methane and nitrogen) than the heavier gases. Comparing the results of the different injectants (with gravity) also indicates that the recovery increases as the molecular weight of the injected gas decreases. This is because of the increased role of gravity when lighter gases are injected because the density difference between injected gas and the original reservoir fluid (buoyancy effects) is higher. It is worth noting from the last column in Table 5.9 that although all gases were simulated at the same value of injection rate, the corresponding injection pressure for each case was different. This is expected considering that in the Peacemann well model (as shown in Equation (5.6), Schlumberger (2018)), the injection rate ( $q$ ) is inversely proportional to the viscosity ( $\mu$ ), but directly proportional to the pressure difference between the cell and injection pressures. So, as the gas viscosity increases for the denser gases, the pressure difference will increase, resulting in lower injection pressures at a fixed value of cell pressure. This explains the lower values of  $\Delta P_{\text{diff}}$  for denser gases because  $\Delta P_{\text{diff}} = P_{\text{inj}} - P_{\text{wf}}$ , and  $P_{\text{wf}}$  is fixed at 1,000 psia. Since SDEOR is a pressure drive recovery, as presented earlier in Section 5.3.1, higher  $\Delta P_{\text{diff}}$  corresponds to higher oil recovery, and hence  $\text{CH}_4$  is the most oil recovery efficient.

$$P_{\text{gb}} - P_w = \frac{q\mu}{2\pi kh} \ln \left( \frac{\Delta x}{r_w} \right), \quad (5.6)$$

where  $P_{\text{gb}}$ ,  $P_w$ ,  $\mu$ ,  $q$ ,  $k$ ,  $h$ ,  $\Delta x$ , and  $r_w$  are average grid block pressure, pressure at wellbore ( $P_{\text{inj}}$  in this case), fluid viscosity, flow rate, permeability, grid thickness, grid block x-dimension, and wellbore radius.

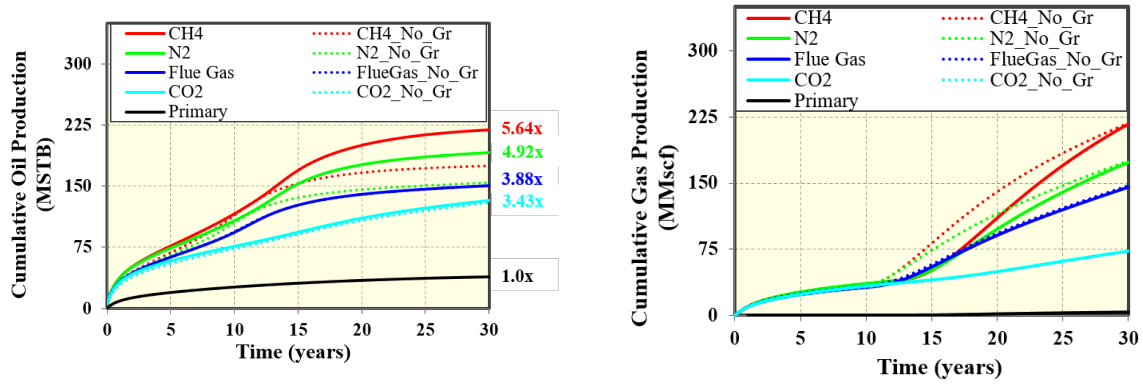


Figure 5.31. Performance plots show that methane gas injection recovers more oil when compared with the injection of the other heavier gases.

Table 5.9. Results of SDEOR with different gas injectants.

Solvent Method	Molecular Weight	Oil RF (%)	Increased Oil RF (%)	IOR Ratio	$\Delta P_{\text{diff}}$ (psia)
CH <sub>4</sub>	16.04	37.70	29.45	5.64	950
N <sub>2</sub>	28.01	32.85	24.6	4.92	890
Flue Gas (25% CO <sub>2</sub> + 75% N <sub>2</sub> )	32.01	31.79	23.54	3.88	850
CO <sub>2</sub>	44.01	29.40	21.15	3.43	770

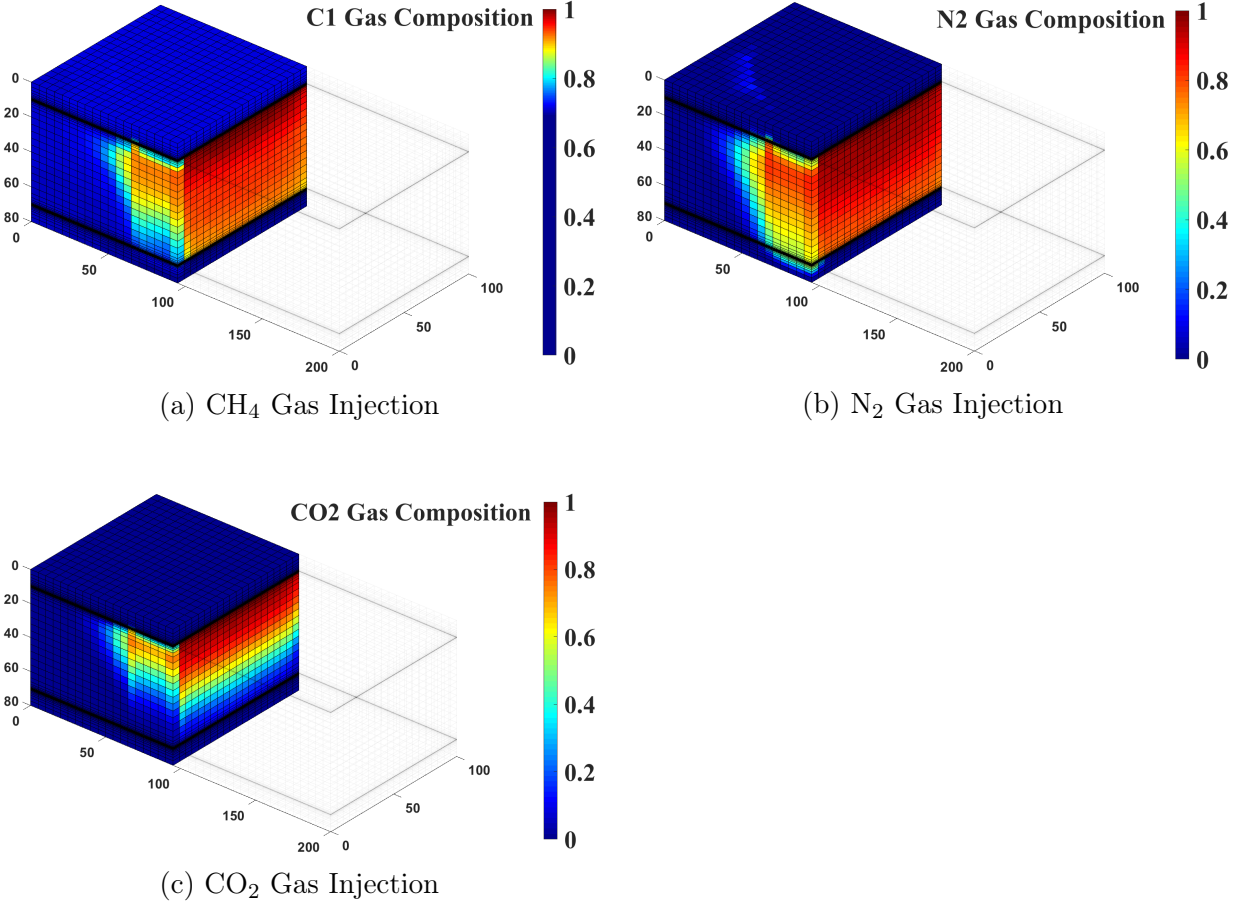


Figure 5.32. Images show solvent's gas composition distribution in the grid blocks after simulating Bakken shale for 30 years: (5.32a) CH<sub>4</sub>, (5.32b) N<sub>2</sub>, and (5.32c) CO<sub>2</sub>. The lightest solvent injection (CH<sub>4</sub>) results in the highest oil RF for the SDEOR technology.

Additionally, we investigate the effects of the miscibility developed between the injectant and reservoir fluid and its effect on our SDEOR technology performance. We start by computing the vapor-liquid equilibrium ratio, or K-value, for each solvent after 30 years, as we define in Equation (5.7) below.

$$K_i = \frac{y_i}{x_i} \quad (5.7)$$

$y_i$  and  $x_i$  are the vapor and liquid composition of component  $i$ , respectively. Figure 5.33 shows images of K-values computed for each grid block for the different solvents used after

30 years. High  $K$ -values indicate that the solvent's  $y_i$  exceeds  $x_i$  and suggest more immiscibility development, and the solvent mostly remains in a gaseous state. So,  $N_2$  gas has the highest tendency to develop immiscibility, as Image 5.33b shows  $K$ -values up to 12 in some grid blocks near the top and bottom SD fractures. Conversely,  $CO_2$  solvent injection shows the highest tendency to develop miscibility as  $K$ -values do not exceed 4, as Image 5.33c shows. Alfarge et al. (2017b) published a comprehensive literature survey about solvent injection methods for shale plays. They showed that  $CO_2$  is the most used solvent for miscible flooding (in CGEOR methods) as it has a low minimum miscibility pressure (MMP) ranging from 2,300 to 3,000 psia and has the most oil recovery efficiency compared to other solvents developing immiscibility, or near miscibility, such as  $N_2$  and  $CH_4$ , respectively.

Again, our SDEOR technology works differently than the CGEOR method because of the involved role of pressure and gravity-drainage mechanisms. Hydrocarbon recovery from Bakken shale under our technology is robust regardless of implementing a miscible/immiscible solvent flooding. We show that the lightest  $CH_4$  (near-miscible flooding) can appreciably recover 5.5 times more oil (+29.45%) compared to primary recovery, and the heaviest  $CO_2$  solvent (miscible flooding) recovers at least 3.4 times more oil (+21.15%). One advantage of  $CH_4$  injection is its low capital expenditure (CAPEX) because it is readily available from associated gas production in the fields, and it can be re-injected on-site.

The field-scale simulation results in these subsections for Bakken shale conclude about the robustness of our proposed SDEOR technology in oil recovery because it (1) extends the reservoir's production lifetime up to 30 years, (2) adapts to different solvent

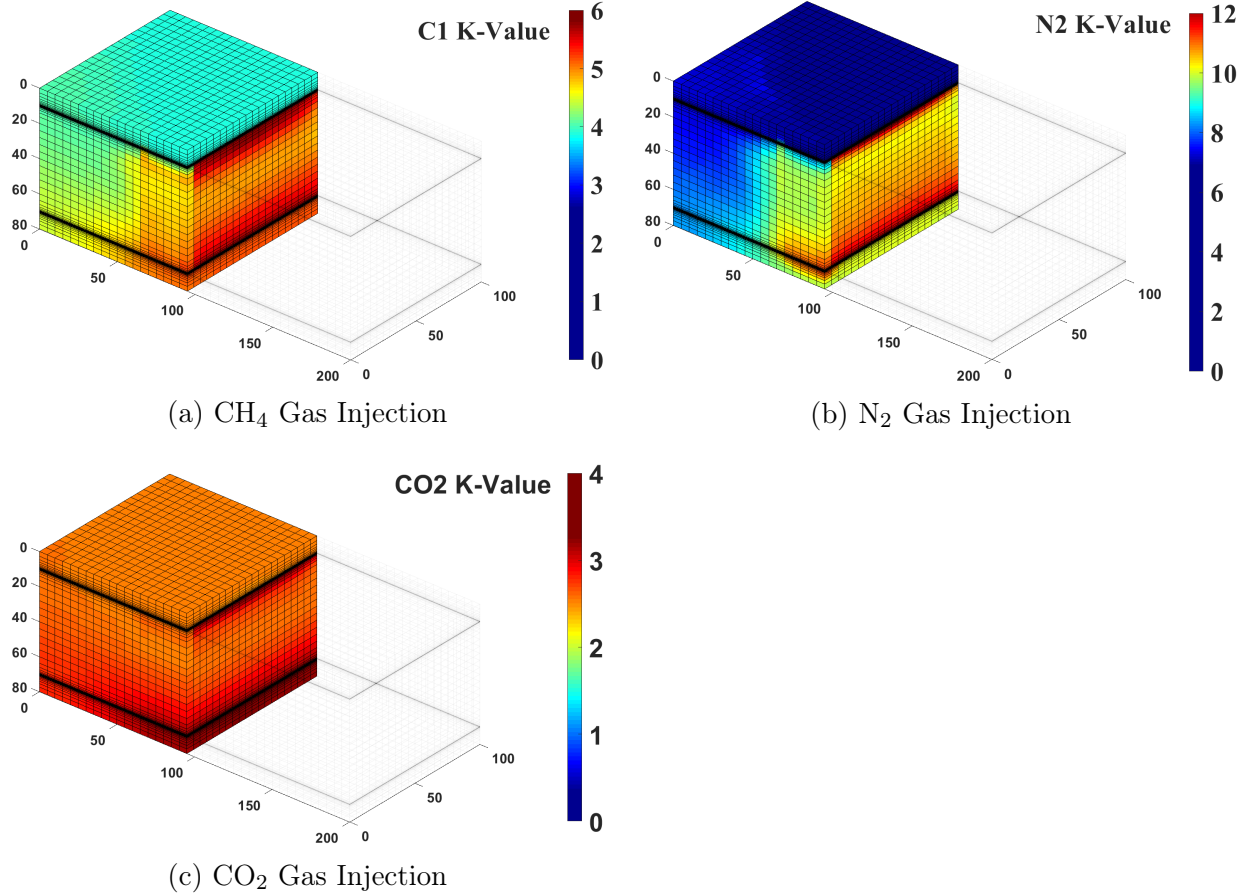


Figure 5.33. Images show solvent's K-value distribution in the grid blocks after simulating Bakken shale for 30 years: (5.33a) CH<sub>4</sub>, (5.33c) CO<sub>2</sub>, and (5.33b) N<sub>2</sub> gases. High K-values imply immiscible solvent flooding, such as N<sub>2</sub>. Regardless of the solvent miscibility/immiscibility with the reservoir fluid, applying our SDEOR technology for Bakken shale outperforms the CGEOR method and produces at least 3.43 more oil than primary recovery for the least efficient CO<sub>2</sub> case and up to 5.64 for the most efficient CH<sub>4</sub> case.

injection methods (miscible and immiscible flooding), and (3) has appreciable recovery from naturally fractured shale plays (existing at either a low or a high conductivity).

## Chapter 6. Conclusions and Recommendation for Future Work.

### 6.1. Summary and Conclusions

The numerical studies performed in this work indicate that our proposed SDEOR technology is robust and applicable in fractured unconventional reservoirs, regardless of the natural fracture intensity, orientation, and distribution. Furthermore, the simulation results obtained indicate that SDEOR outperforms currently used CG EOR methods and recovers at least three times more oil. This numerical study indicates that SDEOR technology could be a game-changer with regards to the development of unconventional reservoirs in the future. Some of the key features of SDEOR are as follows:

1. The Slot Drill (SD) completion technique is advantageous to the conventional hydraulic fracturing because it provides certainty in the location of the slot-drilled fracture, works regardless of rock brittleness, and is more amenable to accurate modeling, given the certainty in the fracture location.
2. Our simulation studies show promising results when this technology is applied to tight oil formations. After only eight years, SDEOR is capable of recovering 11% more oil than primary recovery. Higher oil RFs are also achievable under prolonged periods (30 and 60 years). SDEOR technology performance in fractured tight rocks is robust and slightly dependent on NF intensity, conductivity, and stochastic distribution.
3. Results from implementing molecular diffusion for primary recovery indicates that the resolution must be high enough to capture the diffusion effects; otherwise, the results from low-resolution models become erroneous due to numerical diffusion. At higher matrix permeability, the role of molecular diffusion diminishes as the flow becomes advection-dominated because of the high flow velocity.
4. Our simulation results show that the proposed technology outperforms the cyclic gas EOR (CGEOR) method by a factor of at least three. From our numerical studies of the physical mechanisms that control the proposed technology, we conclude that the drastic increase in recovery is because of the following:
  - (a) The continuous injection and production in the SDEOR technology curtails the effect of a significant reduction in relative oil permeability when the relative gas permeability increases during cyclic gas injection in CGEOR.

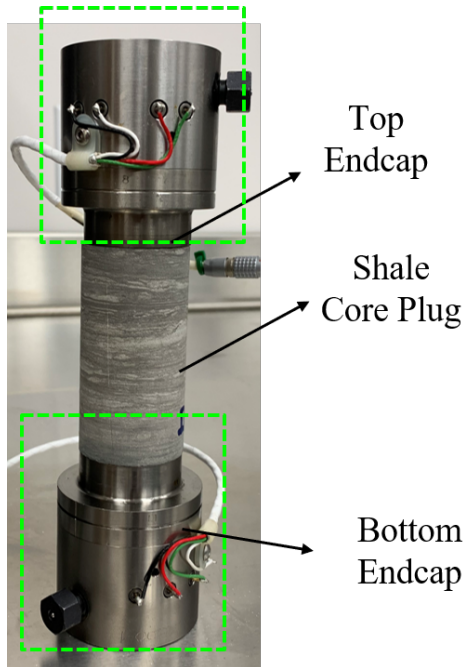
- (b) The SDEOR technology allows continuous production for 100% of the well life, whereas in CGEOR, production is halted during the injection and soaking periods.
- (c) The SDEOR technology is designed to take advantage of gravity in stabilizing the flow through the fracture network, unlike CGEOR, which involves a preferential flow through the poorly known fracture network.

## **6.2. Recommendations for Future Work**

### **6.2.1. Validating Numerical Simulation Results**

Results presented in this work show high recoveries from the SDEOR proposed technology. However, it is worth mentioning that the SD fracturing technology is yet to be tested in the field. So, experimental validation of the numerical results is crucial to confirm that high-recoveries are obtainable at the lab scale before deploying field pilots. Figure 6.1a shows a rock testing cell consisting of (1) a shale core plug, (2) a top endcap for gas injection, and (3) a bottom endcap for oil production. Figure 6.1b shows a closer image of an individual endcap consisting of (1) a groove to mimic flow inside the SD fracture and (2) electric wire connection. We shall run the SDEOR flow experiments using the NER AutoLab 1500 equipment (as shown in Figure 6.2), which can operate at reservoir pressures up to 20,000 psia and reservoir temperatures up to 120°C.





(a) SDEOR test cell



(b) Endcap with a flow groove

Figure 6.1. Left image shows an SDEOR test cell with a shale core plug placed between top and bottom endcaps. Right image shows an individual endcap with a groove to simulate flow inside the SD fracture.



Figure 6.2. An image of the NER AutoLab 1500 testing equipment.

### 6.2.2. Improving Molecular Diffusion Modeling

This work only considered multicomponent hydrocarbon diffusion between matrix and fracture cells in the domain (horizontal arrows in Figure 6.3). However, this diffusion implementation can be improved by considering the diffusion from the matrix into each natural fracture in the domain (as denoted by the matrix-fracture purple curved arrow in Figure 6.3).

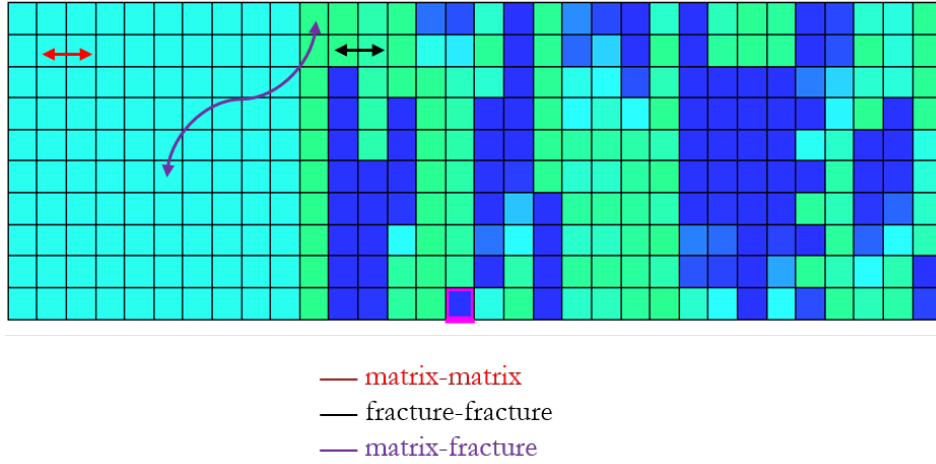


Figure 6.3. A 2D reservoir model after the 3D-pEDFM/EDFM processing. Horizontal arrows indicate standard connection between matrix-matrix and fracture-fracture cells, while the curved purple arrow indicates matrix-fracture non-neighbor connection.

So, we need to extend the 3D-pEDFM and EDFM algorithms by introducing a new diffusive matrix-fracture transfer function. We modify the  $q_i^{nnc}$  term in Equation (2.18) by adding the matrix-fracture diffusion transfer term, defined by the diffusion flux Equation in (2.37), as follows.

$$q_i^{nnc} = \sum_{m=1}^{N_{nnc}} A_m^{nnc} \sum_{\alpha=1}^{n_p} \frac{\rho_m^\alpha X_{i,m}^\alpha}{d_m^{nnc}} \left\{ \overbrace{\frac{k_m^{nnc} k_{r\alpha}}{\mu^\alpha} [(p^\alpha - \rho^\alpha gz) - (p^\alpha - \rho^\alpha gz)_m^{nnc}]}^{\text{advection transfer term}} - \overbrace{\frac{\phi_m S_m^\alpha}{\tau_m} D_{i,m}^a [\ln(f_i^\alpha) - \ln(f_i^\alpha)_m^{nnc}]}^{\text{diffusion transfer term}} \right\} \quad (6.1)$$

Equation (6.1) is dimensionally consistent as the diffusive flux has units of  $(\text{kg} \cdot \text{m}^{-2} \cdot \text{s}^{-1})$ , and it is multiplied by the  $(\sum_{m=1}^{N_{nnc}} A_m^{nnc})$  term with units of  $(\text{m}^2)$ . So, the new  $q_i^{nnc}$  term has the same units of mass rate  $(\text{kg} \cdot \text{s}^{-1})$ . The implementation of Equation (6.1) will be a subject of a future research study.

## Appendix A. Fluids Compositional Input Data

Tables A.1 and A.2 provide the corresponding data for a representative Barnett shale-gas reservoir. Tables A.3 and A.4 provide the compositional fluid data and binary interaction constants used in the simulations that involve a simple three-component hydrocarbon fluid. Tables A.7 and A.8 provide the corresponding data for a representative Bakken shale-oil reservoir, while Tables A.5 and A.6 provide compositional data inputs for a representative Eagle Ford shale-oil reservoir.

Table A.1. Compositional data for Barnett dry gas formation (Xiong et al., 2015).

Components	Mole Fraction	Critical Pressure (atm)	Critical Temperature (K)	Critical Volume (L/mol)	Molar Weight (g/gMol)	Acentric Factor
C <sub>1</sub>	0.991	190.56	190.6	0.099	16.04	0.0114
C <sub>2</sub>	0.0088	48.08	305.32	0.146	30.07	0.099
C <sub>3</sub>	0.0002	41.96	369.89	0.200	44.10	0.1521

Table A.2. Binary Interaction Coefficients for Barnett dry gas formation (Xiong et al., 2015).

Component	C <sub>1</sub>	C <sub>2</sub>	C <sub>3</sub>
C <sub>1</sub>	0	0.005	0.01
C <sub>2</sub>	0.005	0	0.005
C <sub>3</sub>	0.01	0.005	0

Table A.3. Compositional data for SDEOR synthetic oil fluid.

Components	Mole Fraction	Critical Pressure (atm)	Critical Temperature (K)	Critical Volume (L/mol)	Molar Weight (g/gMol)	Acentric Factor
C <sub>1</sub>	0.25	45.39	190.6	0.099	16.04	0.0114
CO <sub>2</sub>	0.25	72.80	304.12	0.094	44.01	0.2239
C <sub>10</sub>	0.50	20.75	617.70	0.601	142.28	0.4884

Table A.4. Binary Interaction Coefficients for SDEOR synthetic oil fluid.

Component	C <sub>1</sub>	CO <sub>2</sub>	C <sub>10</sub>
C <sub>1</sub>	0	0.045	0.1050
CO <sub>2</sub>	0.045	0	0.1150
C <sub>10</sub>	0.1050	0.1150	0

Table A.5. Compositional data for Eagle Ford shale formation, culled from (Yu et al., 2019).

Components	Mole Fraction	Critical Pressure (atm)	Critical Temperature (K)	Critical Volume (L/mol)	Molar Weight (g/gMol)	Acentric Factor	Parachor Coefficient
CO <sub>2</sub>	0.01183	72.80	304.20	0.0940	44.01	0.225	78.01
N <sub>2</sub>	0.00161	33.50	126.20	0.0895	28.01	0.040	41.0
C <sub>1</sub>	0.11541	45.40	190.6	0.0990	16.04	0.008	77.0
C <sub>2</sub> -C <sub>5</sub>	0.26438	36.5	274.74	0.2293	52.02	0.1723	171.07
C <sub>6</sub> -C <sub>10</sub>	0.38089	25.08	438.68	0.3943	103.01	0.2839	297.42
C <sub>11+</sub>	0.22588	17.55	740.29	0.8870	267.15	0.6716	661.45

Table A.6. Binary Interaction Coefficients for Eagle Ford shale formation, culled from (Yu et al., 2019).

Component	CO <sub>2</sub>	N <sub>2</sub>	C <sub>1</sub>	C <sub>2</sub> -C <sub>5</sub>	C <sub>6</sub> -C <sub>10</sub>	C <sub>11+</sub>
CO <sub>2</sub>	0	0.02	0.1030	0.1299	0.15	0.15
N <sub>2</sub>	0.02	0	0.031	0.082	0.12	0.12
C <sub>1</sub>	0.1030	0.031	0	0.0174	0.0462	0.111
C <sub>2</sub> -C <sub>5</sub>	0.1299	0.082	0.0174	0	0.0073	0.0444
C <sub>6</sub> -C <sub>10</sub>	0.15	0.12	0.0462	0.0073	0	0.0162
C <sub>11+</sub>	0.15	0.12	0.111	0.0444	0.0162	0

Table A.7. Compositional data for Bakken light oil shale formation, culled from (Yu et al., 2015).

Components	Mole Fraction	Critical Pressure (atm)	Critical Temperature (K)	Critical Volume (L/mol)	Molar Weight (g/gMol)	Acentric Factor	Parachor Coefficient
CO <sub>2</sub>	0.0002	72.80	304.20	0.0940	44.01	0.225	78.0
N <sub>2</sub>	0.0004	33.50	126.20	0.0895	28.01	0.040	41.0
C <sub>1</sub>	0.25	45.40	190.6	0.0990	16.04	0.008	77
C <sub>2</sub> -C <sub>4</sub>	0.22	42.54	363.30	0.1970	42.82	0.143	145.2
C <sub>5</sub> -C <sub>7</sub>	0.20	33.76	511.56	0.3338	83.74	0.247	250
C <sub>8</sub> -C <sub>9</sub>	0.13	30.91	579.34	0.4062	105.91	0.286	0.099
C <sub>10+</sub>	0.1994	21.58	788.74	0.9208	200.00	0.686	0.099

Table A.8. Binary Interaction Coefficients for Bakken light oil shale formation, culled from (Yu et al., 2015).

Component	CO <sub>2</sub>	N <sub>2</sub>	C <sub>1</sub>	C <sub>2</sub> -C <sub>4</sub>	C <sub>5</sub> -C <sub>7</sub>	C <sub>8</sub> -C <sub>9</sub>	C <sub>10+</sub>
CO <sub>2</sub>	0	-0.02	0.1030	0.1327	0.1413	0.15	0.15
N <sub>2</sub>	-0.02	0	0.013	0.0784	0.1113	0.12	0.12
C <sub>1</sub>	0.1030	0.013	0	0.0078	0.0242	0.0324	0.0779
C <sub>2</sub> -C <sub>4</sub>	0.1327	0.0784	0.0078	0	0.0046	0.0087	0.0384
C <sub>5</sub> -C <sub>7</sub>	0.1413	0.1113	0.0242	0.0046	0	0.0006	0.0169
C <sub>8</sub> -C <sub>9</sub>	0.15	0.12	0.0324	0.0087	0.0006	0	0.0111
C <sub>10+</sub>	0.15	0.12	0.0779	0.0384	0.0169	0.0111	0

## Appendix B. Permissions for Published Work

Figure B.1 is a permission evidence to use Figure 2.1 that compares different fracture modeling approaches.

6/23/2021

Mail - Hassan A Amer - Outlook

**RE: Permission to use an image from SimTech**

Jijun Miao <mj.miao@simtechnologyus.com>

Tue 6/22/2021 7:59 AM

**To:** Hassan A Amer <ahass16@lsu.edu>

Morning, Dear Hassan,

We are good and thank you!

No problem, it's published information and you are good to cite it with reference.

Let me know if we can help some and all the best with your thesis.

Stay safe!

Cheers,

Jijun Miao Ph. D

CEO, Founder of Sim Tech, LLC

Research Advisor in Geology, CPGE, UT Austin

+1 832 520 9138(Cell)

+1 281 245 0851(Office)

[Mj.miao@simtechnologyus.com](mailto:Mj.miao@simtechnologyus.com)

[www.simtechnologyus.com](http://www.simtechnologyus.com)

25807 Westheimer Pkwy, STE 324, Katy, Texas 77494

---

**From:** Hassan A Amer <ahass16@lsu.edu>

**Sent:** Tuesday, June 22, 2021 2:54 AM

**To:** Jijun Miao <mj.miao@simtechnologyus.com>

**Subject:** Permission to use an image from SimTech

Dear Dr. Miao,

I hope this email finds you and you are staying safe.

I am completing my MS thesis at Louisiana State University entitled: "Enhanced Oil Recovery in Tight Rocks Using the 'Slot-Drill' Completion"


I would like your permission to reprint the following material in my thesis, which is in preparation for my graduation in August 2021:

[Website Link: <http://www.simtechnologyus.com/edfm-concept.html>

Image: comparison of different fracture models]

Please contact me if you have any questions or need additional information.

Sincerely,

signature\_402157206

Hassan Amer

<https://outlook.office365.com/mail/inbox/id/AAQkAGE1OGQ2MzgXLWExOTMINGMzYS1INTkzLWM5MGQ5NDY3ZDQxMwAQAPT5WtIS2PRPpV1IGn...> 1/2

Figure B.1. A permission evidence from SimTech, LLC to use the image in Figure 2.1.

## References

- Alfarge, D., Wei, M., and Bai, B. (2017a). Factors affecting co<sub>2</sub>-eor in shale-oil reservoirs: numerical simulation study and pilot tests. *Energy & Fuels*, 31(8):8462–8480.
- Alfarge, D., Wei, M., Bai, B., et al. (2017b). Ior methods in unconventional reservoirs of north america: comprehensive review. In *SPE Western Regional Meeting*. Society of Petroleum Engineers.
- Alghalandis, Y. F. (2017). Adfne: open source software for discrete fracture network engineering, two and three dimensional applications. *Computers & Geosciences*, 102:1–11.
- Apiwathanasorn, S., Ehlig-Economides, C., et al. (2012). Evidence of reopened microfractures in production data analysis of hydraulically fractured shale gas wells. In *SPE Canadian unconventional resources conference*. Society of Petroleum Engineers.
- Carter Jr, E. E. (2011). Method and apparatus for increasing well productivity. US Patent App. 13/130,579.
- Chen, C., Balhoff, M. T., Mohanty, K. K., et al. (2014). Effect of reservoir heterogeneity on primary recovery and co<sub>2</sub> huff’n’puff recovery in shale-oil reservoirs. *SPE Reservoir Evaluation & Engineering*, 17(03):404–413.
- Coats, K. (1979). An equation of state compositional model spe8284. In *54th Annual Fall Technology Conference and Exhibition of the Society of Petroleum Engineers, Las Vegas, Nevada, US*.
- Coleman, I. J. K. and Hester, N. C. (2010). Drilling and opening reservoir using an oriented fissure to enhance hydrocarbon flow and method of making. US Patent 7,647,967.
- Cronin, M., Emami-Meybodi, H., Johns, R. T., et al. (2020). Multicomponent diffusion modeling of cyclic solvent injection in ultratight reservoirs. *SPE Journal*.
- Dahaghi, A. K. et al. (2010). Numerical simulation and modeling of enhanced gas recovery and co<sub>2</sub> sequestration in shale gas reservoirs: A feasibility study. In *SPE international conference on CO<sub>2</sub> capture, storage, and utilization*. Society of Petroleum Engineers.
- Du, F. and Nojabaei, B. (2019). A review of gas injection in shale reservoirs: enhanced oil/gas recovery approaches and greenhouse gas control. *Energies*, 12(12):2355.
- Eshkalak, M. O., Al-shalabi, E. W., Sanaei, A., Aybar, U., Sepehrnoori, K., et al. (2014). Enhanced gas recovery by co<sub>2</sub> sequestration versus re-fracturing treatment in unconventional shale gas reservoirs. In *Abu Dhabi International Petroleum Exhibition and Conference*. Society of Petroleum Engineers.
- Farrar, R. B., Mayercheck, W. D., and Bockosh, G. R. (1991). Method of mining a mineral deposit seam.
- Fick, A. (1855). Ueber diffusion. *Annalen der Physik*, 170(1):59–86.



- Firoozabadi, A. (2015). *Thermodynamics and applications of hydrocarbon energy production*. McGraw Hill Professional.
- Ganjdanesh, R., Yu, W., Fiallos Torres, M. X., Sepehrnoori, K., Kerr, E., Ambrose, R., et al. (2019). Huff-n-puff gas injection for enhanced condensate recovery in eagle ford. In *SPE Annual Technical Conference and Exhibition*. Society of Petroleum Engineers.
- Grinestaff, G., Barden, C., Miller, J., Franklin, W., Barden, C., Ding, E., et al. (2020). Evaluation of eagle ford cyclic gas injection eor: Field results and economics. In *SPE Improved Oil Recovery Conference*. Society of Petroleum Engineers.
- Hao, M., Liao, S., Yu, G., Lei, X., and Tang, Y. (2020). Performance optimization of co2 huff-n-puff for multifractured horizontal wells in tight oil reservoirs. *Geofluids*, 2020.
- Haridy, M. G., Sedighi, F., Ghahri, P., Ussenova, K., Zhiyenkulov, M., et al. (2019). Comprehensive study of the oda corrected permeability upscaling method. In *SPE/IATMI Asia Pacific Oil & Gas Conference and Exhibition*. Society of Petroleum Engineers.
- Hoffman, B. T. (2018). Huff-n-puff gas injection pilot projects in the eagle ford. In *SPE Canada Unconventional Resources Conference*. OnePetro.
- Hoffman, B. Todd, J. G. et al. (2016). Improved oil recovery ior pilot projects in the bakken formation. In *SPE low perm symposium*. Society of Petroleum Engineers.
- Hurd, R. L. (1980). Method and apparatus for deep mining using chain driven in fixed direction. US Patent 4,232,904.
- Jacobs, T. et al. (2019). Shale eor delivers, so why won't the sector go big? *Journal of Petroleum Technology*, 71(05):37–41.
- Karimi-Fard, M. and Firoozabadi, A. (2001). Numerical simulation of water injection in 2d fractured media using discrete-fracture model. In *SPE Annual Technical Conference and Exhibition*, New Orleans, Louisiana, USA. Society of Petroleum Engineers.
- Kim, J.-G. and Deo, M. D. (2000). Finite element, discrete-fracture model for multiphase flow in porous media. *AIChE J.*, 46(6):1120–1130.
- Kim, T., Park, S., Lee, K. S., et al. (2015). Modeling of co2 injection considering multi-component transport and geomechanical effect in shale gas reservoirs. In *SPE/IATMI Asia Pacific Oil & Gas Conference and Exhibition*. Society of Petroleum Engineers.
- Kowalski, B. (2010). *Quantitative mineralogic analysis of the middle Bakken member, Parshall Field, Mountrail County, North Dakota*. PhD thesis, Colorado School of Mines.
- Krogstad, S., Lie, K.-A., Møyner, O., Nilsen, H. M., Raynaud, X., Skaflestad, B., et al. (2015). Mrst-ad—an open-source framework for rapid prototyping and evaluation of reservoir simulation problems. In *SPE reservoir simulation symposium*. Society of Petroleum Engineers.

- Kuuskraa, V., Murray, B., and Petrusak, R. (2020). Increasing shale oil recovery and co2 storage with cyclic co2 enhanced oil recovery. <https://bit.ly/34I4fIu>. USEA/DOE-002415-20-01.
- Lake, L. W., Johns, R., Rossen, W. R., Pope, G. A., et al. (2014). Fundamentals of enhanced oil recovery.
- Li, L. and Lee, S. H. (2008). Efficient field-scale simulation of black oil in a naturally fractured reservoir through discrete fracture networks and homogenized media. *SPE Reserv. Evaluation Eng.*, 11(04):750–758.
- Lie, K.-A. (2019). *An introduction to reservoir simulation using MATLAB/GNU Octave: User guide for the MATLAB Reservoir Simulation Toolbox (MRST)*. Cambridge University Press.
- Lohrenz, J., Bray, B. G., Clark, C. R., et al. (1964). Calculating viscosities of reservoir fluids from their compositions. *Journal of Petroleum Technology*, 16(10):1–171.
- Moinfar, A., Varavei, A., Sepehrnoori, K., Johns, R. T., et al. (2012). Development of a novel and computationally-efficient discrete-fracture model to study ior processes in naturally fractured reservoirs. In *SPE improved oil recovery symposium*. Society of Petroleum Engineers.
- Moridis, G., Reagan, M., et al. (2020). Evaluation of the effectiveness of continuous gas displacement for eor in hydraulically fractured shale reservoirs. In *SPE Latin American and Caribbean Petroleum Engineering Conference*. Society of Petroleum Engineers.
- Møyner, O., Tchelepi, H., et al. (2017). A multiscale restriction-smoothed basis method for compositional models. In *SPE Reservoir Simulation Conference*. Society of Petroleum Engineers.
- Niven, E. B. and Deutsch, C. V. (2010). Relating different measures of fracture intensity. *CCG Annual Report-Paper 103, Centre for Computational Geostatistics*.
- Odunowo, T. O., Moridis, G. J., Blasingame, T. A., Olorode, O. M., Freeman, C. M., et al. (2014). Evaluation of well performance for the slot-drill completion in low-and ultralow-permeability oil and gas reservoirs. *SPE Journal*, 19(05):748–760.
- Olorode, O., Wang, B., Rashid, H. U., et al. (2020). Three-dimensional projection-based embedded discrete-fracture model for compositional simulation of fractured reservoirs. *SPE Journal*, 25:2143–2161.
- Peng, D.-Y. and Robinson, D. B. (1976). A new two-constant equation of state. *Industrial & Engineering Chemistry Fundamentals*, 15(1):59–64.
- Pospisil, G., Weddle, P., Strickland, S., McChesney, J., Tompkins, K., Neuroth, T., Pearson, C. M., Griffin, L., Kaier, T., Sorensen, J., et al. (2020). Report on the first rich gas eor cyclic multiwell huff n puff pilot in the bakken tight oil play. In *SPE Annual Technical Conference and Exhibition*. Society of Petroleum Engineers.

- Pruess, K. and Narasimhan, T. N. (1982). A practical method for modeling fluid and heat flow in fractured porous media. *SPE J.*, 25(01):14–26.
- Rassenfoss, S. et al. (2017). Shale eor works, but will it make a difference? *Journal of Petroleum Technology*, 69(10):34–40.
- Raterman, K. T., Farrell, H. E., Mora, O. S., Janssen, A. L., Gomez, G. A., Busetti, S., McEwen, J., Frieauf, K., Rutherford, J., Reid, R., et al. (2018). Sampling a stimulated rock volume: An eagle ford example. *SPE Reservoir Evaluation & Engineering*, 21(04):927–941.
- Schlumberger (2018). Eclipse technical description manual.
- Shafiei, A., Dusseault, M. B., Kosari, E., and Taleghani, M. N. (2018). Natural fractures characterization and in situ stresses inference in a carbonate reservoir—an integrated approach. *Energies*, 11(2):312.
- Sturm, S. D. and Gomez, E. (2009). Role of natural fracturing in production from the bakken formation, williston basin north dakota. In *AAPG Annual Convention and Exhibition*, volume 50199.
- Sun, J., Zou, A., Schechter, D., et al. (2016). Experimental and numerical studies of co 2 eor in unconventional liquid reservoirs with complex fracture networks. In *SPE Improved Oil Recovery Conference*. Society of Petroleum Engineers.
- Sun, R., Yu, W., Xu, F., Pu, H., and Miao, J. (2019). Compositional simulation of co2 huff-n-puff process in middle bakken tight oil reservoirs with hydraulic fractures. *Fuel*, 236:1446–1457.
- Taylor, R. and Krishna, R. (1993). *Multicomponent mass transfer*, volume 2. John Wiley & Sons.
- Tene, M. (2018). *Algebraic Multiscale Framework for Fractured Reservoir Simulation*. PhD thesis, Delft University of Technology.
- Tene, M., Bosma, S. B., Al Kobaisi, M. S., and Hajibeygi, H. (2017). Projection-based embedded discrete fracture model (pedfm). *Advances in Water Resources*, 105:205–216.
- Thakur, G. et al. (2019). Enhanced recovery technologies for unconventional oil reservoirs. *Journal of Petroleum Technology*, 71(09):66–69.
- Warren, J. E. and Root, P. J. (1963). The behavior of naturally fractured reservoirs. *SPE J.*, 3(03):245–255.
- Wattenbarger, R. A., El-Banbi, A. H., Villegas, M. E., and Maggard, J. B. (1998). Production analysis of linear flow into fractured tight gas wells. In *SPE rocky mountain regional/low-permeability reservoirs symposium*. OnePetro.

- Xiong, Y., Winterfeld, P., Wang, C., Huang, Z., Wu, Y.-S., et al. (2015). Effect of large capillary pressure on fluid flow and transport in stress-sensitive tight oil reservoirs. In *SPE Annual Technical Conference and Exhibition*. Society of Petroleum Engineers.
- Yew, C. H. and Weng, X. (2014). *Mechanics of hydraulic fracturing*. Gulf Professional Publishing.
- Yu, W., Al-Shalabi, E. W., Sepehrnoori, K., et al. (2014a). A sensitivity study of potential co2 injection for enhanced gas recovery in barnett shale reservoirs. In *SPE unconventional resources conference*. Society of Petroleum Engineers.
- Yu, W., Lashgari, H., Sepehrnoori, K., et al. (2014b). Simulation study of co2 huff-n-puff process in bakken tight oil reservoirs. In *SPE Western North American and Rocky Mountain Joint Meeting*. Society of Petroleum Engineers.
- Yu, W., Lashgari, H. R., Wu, K., and Sepehrnoori, K. (2015). Co2 injection for enhanced oil recovery in bakken tight oil reservoirs. *Fuel*, 159:354–363.
- Yu, W., Zhang, Y., Varavei, A., Sepehrnoori, K., Zhang, T., Wu, K., Miao, J., et al. (2019). Compositional simulation of co 2 huff’n’puff in eagle ford tight oil reservoirs with co 2 molecular diffusion, nanopore confinement, and complex natural fractures. *SPE Reservoir Evaluation & Engineering*, 22(02):492–508.
- Zhang, Y., Yu, W., Li, Z., and Sepehrnoori, K. (2018). Simulation study of factors affecting co2 huff-n-puff process in tight oil reservoirs. *Journal of Petroleum Science and Engineering*, 163:264–269.
- Zhu, P., Balhoff, M. T., and Mohanty, K. K. (2017). Compositional modeling of fracture-to-fracture miscible gas injection in an oil-rich shale. *Journal of Petroleum Science and Engineering*, 152:628–638.
- Zoback, M. D. (2010). *Reservoir geomechanics*. Cambridge University Press.
- Zou, A., Schechter, D., et al. (2017). Investigation of the oil recovery mechanism during laboratory co 2 eor experiments with unconventional shale cores through compositional simulation. In *Carbon Management Technology Conference*. Carbon Management Technology Conference.
- Zuloaga, P., Yu, W., Miao, J., and Sepehrnoori, K. (2017). Performance evaluation of co2 huff-n-puff and continuous co2 injection in tight oil reservoirs. *Energy*, 134:181–192.
- Zuloaga-Molero, P., Yu, W., Xu, Y., Sepehrnoori, K., and Li, B. (2016). Simulation study of co2-eor in tight oil reservoirs with complex fracture geometries. *sci. rep.* 6: 33445.

## Vita

Hassan Amer received his bachelor's degree in Petroleum Engineering from The American University in Cairo (AUC) in June 2019 with a 4.0 GPA. In August 2019, Hassan joined Louisiana State University (LSU), where he anticipates graduating with his Master of Science degree in Petroleum Engineering and a graduate minor in computer science both in August 2021. He holds the Engineer-In-Training (EIT) certification from Texas Board of Professional Engineers. To date, he accumulated two years of oil & gas industry experience working as a Reservoir Simulation Engineer for SimTech, LLC, a Junior Engineer for Apache Egypt Companies, and interning for different Egyptian National Oil Companies (e.g., Khalda Petroleum Company, Qarun Petroleum Company, and Petrobel). Upon graduation, he will be joining the University of Texas at Austin's Petroleum Engineering Department as a Ph.D. student.